UNIVERSIDADE FEDERAL DO RIO GRANDE DO SUL
PROGRAMA DE PÓS-GRADUAÇÃO EM FÍSICA

Exploring the Properties of Pure and Mo-Doped Ta_3N_5: A Theoretical and Experimental Investigation

By

Hameed Ullah

Institute of Physics

Thesis submitted to the Universidade Federal do Rio Grande do Sul (UFRGS), Porto Alegre, Brazil, as a partial requirement to obtain the degree of Doctor in Science, under the supervision of Prof. Dr. Sherdil Khan (Institute of Physics, UFRGS) and Prof. Dr. Marcos Jose Leite Santos (Institute of Chemistry, UFRGS).

Porto Alegre

October 2023

UNIVERSIDADE FEDERAL DO RIO GRANDE DO SUL
PROGRAMA DE PÓS-GRADUAÇÃO EM FÍSICA

Investigação das Propriedades do Ta_3N_5 Puro e Dopado com Mo: Um Estudo Teórico e Experimental

Por

Hameed Ullah

Instituto de Física

Tese submetido Universidade Federal do Rio Grande do Sul (UFRGS), Porto Alegre, Brasil, como requisito parcial para a obtenção do titulo de Doutor em Ciências Exatas, sob a orientação do Prof. Dr. Sherdil Khan (Instituto de Física, UFRGS) e Prof. Dr. Marcos José Leite Santos (Instituto de Química, UFRGS).

Porto Alegre

Outubro de 2023

Acknowledgment

I would like to express my sincere gratitude to the Almighty Allah, the creator of the Universe, for granting me the opportunity to pursue a PhD in Physics

First and foremost, my heartfelt thanks go to my supervisor, Prof. Dr. Sherdil Khan. His invaluable guidance, unwavering support, and consistent encouragement have been instrumental in shaping the direction of my research and elevating the quality of this thesis. I am truly fortunate to have had the privilege of working under his mentorship.

I also extend my gratitude to my co-supervisor, Prof. Dr. Marcos Leite, for his valuable support and insights during my PhD study and research.

I am profoundly grateful to Prof. Dr. Altaf Ur Rahman for his unwavering support and guidance throughout my PhD journey. His constant encouragement and motivation have been instrumental in inspiring me to work diligently and strive for excellence.

Last but certainly not least, I would like to extend my heartfelt gratitude to my wife, PhD scholar Sadaf Aqil, whose unwavering support and understanding have been the cornerstone of my academic journey. Her sacrifices, patience, and enduring belief in me have been my constant source of strength. She has stood by my side through the late nights, countless revisions, and the highs and lows of this challenging endeavor. Without her love and encouragement, completing this PhD would have been an even more daunting task. Her presence has made every achievement sweeter and every hurdle easier to overcome. I dedicate this thesis to her, with all my love and appreciationI would like to express my heartfelt appreciation to my entire family for their unwavering love, support, and encouragement throughout my academic journey

I owe a debt of gratitude to my colleagues and fellow researchers at the Nanomaterials for Renewable Energy and Artificial Photosynthesis (NanoREAP) laboratory. Their collaboration, stimulating discussions, and willingness to share knowledge have enriched my research journey and made it both productive and enjoyable.

Additionally, I would like to acknowledge the generous financial support provided by the National Council for Scientific and Technological Development (CNPq). Their funding has played a vital role in facilitating my experiments and providing access to research materials, without which this thesis would not have come to fruition.

Table of Contents

List of Figures

List of Tables

List of Abbreviation

QE Quantum Espresso

PS Pseudo Potential

HH Half-Heusler

E_x Exchange Energy

KS Kohn-Sham

DFT Density Functional Theory

HFT Hartree-Fock Theory

HKT Hohenberg-Kohn Theorem

LMTO Linear Muffin Tin Orbitals

LDA Local Density Approximation

GGA Generalized Gradient Approximation

PAW Projected Augmented Wave

TDOS Total Density of States

PDOS Partial Density of States

LAPW Linearized Augmented Plane Wave

NTs Nanotubes

PEC Photoelectrochemical

RHE Reversible Hydrogen Electrode

SEM Scanning Electron Microscope

TEM Transmission electron microscope

MTN Molybdenum Tantalum Nanotubes

CB Conduction Band

VB Valance Band

E_f	Fermi Energy
m_e	Electron Mass
m_h	hole mass
XPS	X-rays Photoelectron Spectroscopy

Abstract

Addressing global warming necessitates collective actions such as adopting more sustainable lifestyles, transition to renewable energy and support international climate policies. In the field of renewable energy, utilizing semiconductor-liquid interfaces to produce green energy through artificial photosynthesis holds promising potential. Ta_3N_5 (E_g~2.1eV) is one of the excellent candidates for photochemical water splitting. However, to date, it suffers from fast e^-/h^+ recombination, hole trapping, and high temperature nitridation based defects generation. Doping Ta_3N_5 and loading suitable co-catalysts are the key strategies towards improving its electronic and optical properties for enhanced photochemical performance. Aiming to address these issues, here we studied structural, electronic and optical properties of pure and Mo doped Ta_3N_5 utilizing density functional theory (DFT) and experimental approaches. DFT calculations were based on generalized gradient approximation (GGA) and to obtain more realistic results GGA+U was also utilized. GGA+U calculated electronic bandgap energy was red-shifted from 1.98 to 1.16 eV for Mo-doped Ta_3N_5. The nature of the bandgap was changed from the indirect to direct bandgap semiconductor which might help to increase the light absorption coefficient and improve the charge carrier's mobility. The valence band (VB) of pure and Mo doped Ta_3N_5 was mainly composed of N2p orbitals while the conduction band (CB) was composed of Ta4d and Mo3d orbitals for Mo doped Ta_3N_5 as compared to Ta4d of pure one. Due to the smaller electronegativity difference between Mo (2.16) and N (3.04) as compared to Ta (1.5) and N (3.04), the bond length decreased from 1.97 Å to 1.86 Å for Mo doped Ta_3N_5 and the density of states was increased in the CB. Mo doped Ta_3N_5 maintained n-type conductivity of Ta_3N_5. Utilizing norm-conserving pseudopotential (Fritz Haber Institute), the optical properties were studied. The optical bandgap was also red-shifted from 1.96 to 1.20 eV for Mo-doped Ta_3N_5 which is consistent with the electronic bandgap energy calculation. In line with the red-shift in the bandgap energy, the dielectric constant was also increased from 6 to 8.31 by Mo doping. Reflective index was increased from 2.51 to 2.89 and reflectivity was decreased from 35% to 29% which suggests a decrease in the electron energy loss and improvement in the light-matter interaction for Mo doped Ta_3N_5. This might also be attributed to changing the nature of the bandgap from indirect to direct. To experimentally dope Ta_3N_5, firstly in this work Ta_2O_5 nanotubes (NTs) have been synthesized by anodization technique. After

anodization, the amorphous Ta_2O_5 NTs were transformed to Ta_3N_5 by nitridation at 900°C for 3h. For Mo doping, prior to the nitridation, different amount of Mo (Mo/Ta (mol/mol) 0.1, 0.3 and 0.5) were added in Ta_2O_5 by hydrothermal process. The crystal structure was studied by X-ray diffraction and Raman Spectroscopy. The crystallite size was increased from 12.5 to ~15 nm by Mo doping. In Raman Spectroscopy, the full width half maximum of the A_g mode located at 271cm^{-1} was decreased and the peak position showed a distinct red-shift, indicative of successful Mo doping in Ta_3N_5. The Scanning Electron Microscopy (SEM) technique showed that after nitridation the length of the NTs decreased from 2.1 µm to 1.5 µm attributed to the density difference between Ta_2O_5 and Ta_3N_5. The measured outer diameter of anodized Ta_2O_5 from TEM image was 116 ± 5 nm while that of Ta_3N_5 was 65 nm ± 5 nm. Energy-Dispersive X-ray Spectroscopy (EDX) results confirmed the existence of Mo in all doped samples which was also complemented by X-ray photoelectron spectroscopy (XPS). The photoelectrochemical water oxidation test demonstrated that Mo doping significantly enhances the water oxidation performance of Ta_3N_5. Initially, the calculated current density for Ta_3N_5 stood at 0.78 mA/cm² at 1.23 V_{RHE}, but with the introduction of Mo doping and without co-catalyst modification, this value surged to 2 mA/cm². MTN-0.1, among the various Mo-doped samples, displayed the highest current density, peaking at 3 mA/cm² at 1.54 V_{RHE}. This study underscores that Mo doping not only boosts the water oxidation performance of Ta_3N_5 but also induces a cathodic shift in the onset potential toward lower values. Furthermore, when the surface was enhanced with Co(OH)x as a co-catalyst, the most effective photoanode achieved remarkable results. It yielded a peak current density of 6.1 mA/cm² at 1.54 V_{RHE} while maintaining the lowest onset potential at a mere 0.57 V_{RHE}.

Keywords: Ta_3N_5, Ta_2O_5, Photoelectrochemical, artificial photosynthesis, Anodization

Resumo

Abordar o aquecimento global requer ações coletivas, como a adoção de estilos de vida mais sustentáveis, transição para energia renovável e apoio a políticas climáticas internacionais. No campo da energia renovável, a utilização de interfaces semicondutores-líquidos para produzir energia verde por meio da fotossíntese artificial tem um potencial promissor. Ta_3N_5 (Eg~2.1eV) é um dos excelentes candidatos para a separação fotoquímica da água. No entanto, até o momento, ele sofre de rápida recombinação e-/h+, aprisionamento de lacunas e geração de defeitos baseados em nitretação de alta temperatura. A dopagem de Ta_3N_5 e o carregamento de cocatalisadores adequados são as principais estratégias para melhorar suas propriedades eletrônicas e ópticas para melhorar o desempenho fotoquímico. Com o objetivo de abordar essas questões, aqui estudamos as propriedades estruturais, eletrônicas e ópticas do Ta_3N_5 puro e dopado com Mo, utilizando a teoria do funcional da densidade (DFT) e abordagens experimentais. Os cálculos DFT foram baseados na aproximação de gradiente generalizado (GGA) e para obter resultados mais realistas GGA+U também foi utilizado. A energia de banda proibida eletrônica calculada por GGA+U foi desviada para o vermelho de 1,98 para 1,16 eV para Ta_3N_5 dopado com Mo. A natureza do bandgap foi alterada do semicondutor bandgap indireto para direto, o que pode ajudar a aumentar o coeficiente de absorção de luz e melhorar a mobilidade dos portadores de carga. A banda de valência (VB) do Ta_3N_5 puro e dopado com Mo era composta principalmente por orbitais N2p, enquanto a banda de condução (CB) era composta pelos orbitais Ta4d e Mo3d para o Ta_3N_5 dopado com Mo em comparação com o Ta4d do puro. Devido à menor diferença de eletronegatividade entre Mo (2,16) e N (3,04) em comparação com Ta (1,5) e N (3,04), o comprimento da ligação diminuiu de 1,97 Å para 1,86 Å para Ta_3N_5 dopado com Mo e a densidade de estados foi aumentada no CB. Ta_3N_5 dopado com Mo manteve a condutividade do tipo n de Ta_3N_5. Utilizando pseudopotencial de conservação de norma (Fritz Haber Institute), as propriedades ópticas foram estudadas. O bandgap óptico também foi deslocado para o vermelho de 1,96 para 1,20 eV para Ta_3N_5 dopado com Mo, o que é consistente com o cálculo eletrônico de energia do bandgap. De acordo com o desvio para o vermelho na energia do bandgap, a constante dielétrica também foi aumentada de 6 para 8,31 por dopagem com Mo. O índice de reflexão aumentou de 2,51 para 2,89 e a refletividade diminuiu de 35% para 29%, o que sugere uma diminuição na perda de energia de

elétrons e melhora na interação luz-matéria para Ta_3N_5 dopado com Mo. Isso também pode ser atribuído à mudança da natureza do bandgap de indireto para direto. Para dopar experimentalmente o Ta_3N_5, primeiramente neste trabalho foram sintetizados nanotubos (NTs) de Ta_2O_5 por técnica de anodização. Após a anodização, os NTs Ta_2O_5 amorfos foram transformados em Ta_3N_5 por nitretação a 900°C por 3h. Para a dopagem de Mo, antes da nitretação, diferentes quantidades de Mo (Mo/Ta (mol/mol) 0,1, 0,3 e 0,5) foram adicionadas em Ta_2O_5 por processo hidrotérmico. A estrutura cristalina foi estudada por difração de raios X e espectroscopia Raman. O tamanho do cristalito foi aumentado de 12,5 para ~15 nm por dopagem com Mo. Na Espectroscopia Raman, o meio máximo da largura total do modo Ag localizado em 271 cm^{-1} foi diminuído e a posição do pico mostrou um desvio para o vermelho distinto, indicativo de doping de Mo bem-sucedido em Ta_3N_5. A técnica de Microscopia Eletrônica de Varredura (MEV) mostrou que após a nitretação o comprimento dos NTs diminuiu de 2,1 µm para 1,5 µm atribuído à diferença de densidade entre Ta_2O_5 e Ta_3N_5. O diâmetro externo medido do Ta_2O_5 anodizado da imagem TEM foi de 116 ± 5 nm, enquanto o do Ta_3N_5 foi de 65 nm ± 5 nm. Os resultados da Espectroscopia de Raios X por Dispersão de Energia (EDX) confirmaram a existência de Mo em todas as amostras dopadas, o que também foi complementado pela espectroscopia de fotoelétrons de raios X (XPS). O teste fotoeletroquímico de oxidação da água demonstrou que a dopagem com Mo aumenta significativamente o desempenho de oxidação da água do Ta_3N_5. Inicialmente, a densidade de corrente calculada para Ta_3N_5 era de 0,78 mA/cm² a 1,23 V_{RHE}, mas com a introdução da dopagem com Mo e sem modificação do cocatalisador, esse valor subiu para 2 mA/cm². MTN-0.1, entre as várias amostras dopadas com Mo, apresentou a maior densidade de corrente, atingindo um máximo de 3 mA/cm² a 1,54 V_{RHE}. Este estudo ressalta que a dopagem com Mo não apenas aumenta o desempenho de oxidação da água do Ta_3N_5, mas também induz uma mudança catódica no potencial de início para valores mais baixos. Além disso, quando a superfície foi melhorada com Co(OH)x como co-catalisador, o fotoanodo mais eficaz alcançou resultados notáveis. Ele produziu uma densidade de corrente de pico de 6,1 mA/cm² a 1,54 V_{RHE}, mantendo o potencial de início mais baixo em apenas 0,57 V_{RHE}.

Palavras-chave: Ta_3N_5, Ta_2O_5, Fotoeletroquímico, fotossíntese artificial, Anodização

Overview

Since the industrial revolution, there has been a significant increase in both the global temperature and the concentration of greenhouse gases in the Earth's atmosphere [1]. Furthermore, in light of the Paris agreement's goal to limit global warming, countries require an accelerated transformation of their industry, transportation, and energy sectors towards renewable sources [2]. As the world population and industrialization continue to rapidly rise, the demand for energy is increasing every day. All the carbon-based fossil fuels currently employed as global energy sources have finite lifespans [3]. The most pressing challenge facing today's scientific community is the transition from a carbon-based economy to a carbon-free one [4]. Hydrogen emerges as a promising candidate for utilization as a sustainable energy source. It is also called a clean fuel and an ideal energy carrier. The gravimetric energy density of hydrogen is 3 times higher than all other known hydrocarbons-based fuel [5]. Furthermore, hydrogen is considered as the most abundant element on earth [6]. To split water by using semiconductor and solar energy is one of the attractive fields of research after the Fujishima and Honda discovery in 1972 [7]. The solar energy striking the earth surface consists of 10% ultra violet (UV), 40% visible and 50% infrared (IR). In 2015, the U.S. Department of Energy revealed a remarkable fact: the energy received from the sun on Earth's surface in just one hour amounted to 4.3×10^{20} J, nearly equivalent to the total energy consumption of our modern civilization over the course of one year, which was 4.1×10^{20} J. These statistics strongly indicate that by harvesting sun energy we may solve the energy crises. There are different mechanisms used to produce hydrogen from water by using solar radiation. These methods are photoelectrochemical (PEC) water splitting, photocatalytic water splitting, thermochemical conversion, photobiological methods, molecular artificial photosynthesis, and plasma chemical conversion [7]. In photoelectrochemical (PEC) water splitting, a suitable semiconducting material is used to split water into hydrogen and oxygen. This method has several advantages. One of the main advantages of PEC is that oxygen and hydrogen are produced at different electrodes and thus are easily separable. This process can be carried out at room temperature.

Among the nitride semiconductors, Ta_3N_5 has emerged as one of the promising candidates for overall water splitting as a photocatalyst or photoanode due to its suitable bandgap and bands position. Ta_3N_5 has an experimental bandgap of 2.1 eV while a

theoretical bandgap of 2 eV [8]. Although the theoretical solar to hydrogen (STH) energy conversion efficiency of Ta_3N_5 is 15.9%, intensive efforts have been made to improve the STH efficiency of Ta_3N_5 and despite these efforts the highest efficiency achieved so far is 2.72%, which is still very low as compared to the theoretical value [9]. Additionally, to improve the photocatalytic performance of Ta_3N_5 several nano-morphologies like Nanorods (NRs) [10], Nanoparticles, Nanotubes (NTs) [11] have been developed and studied. It has been observed that among the aforementioned Nano-morphologies, the 1D nanotubes (NTs) of Ta_3N_5 exhibit excellent charge transport properties along with a substantial active surface area, rendering them highly suitable candidates for photoelectrochemical (PEC) applications. The 1D Ta_3N_5 NTs was first prepared by Feng et al in 2010 by nitridation of amorphous Ta_2O_5 NTs [11]. In this work our goal is to engineer the electronic and optical properties of Ta_3N_5 and use it in PEC water splitting.

During my Ph.D., my research extended beyond the exploration of Ta_3N_5 to encompass various projects involving the prediction and investigation of both 2D and 3D materials. Noteworthy among these materials are CrSSe, TiO_2/V_2O_5, $BiVO_4$, CaO, MnO_2, C_3N_4, CuO, WO_3, and CdS. Notably, we introduced CrSSe as a 2D material for the first time, employing Density Functional Theory (DFT) for its prediction. Concurrently, we conducted comprehensive studies on the distinctive properties of the remaining materials.

Our findings and contributions to the field have been disseminated through publications in well-established journals. The author has published research on the homogeneous V incorporation in TiO_2 and the novel 2D material CrSSe, serving as the first author for both. Consequently, a brief overview of these two materials is provided below. For further details and a comprehensive overview of the published work related to these materials, please refer to the appendix of the thesis.

Because of interesting and environmental friendly properties like non-toxic, cheap, corrosion resistive, TiO_2 have attracted a lot of scientific attention [12]. There are different pathways by which TiO_2 can be prepared like hydro/solvothermal method, sol gel method, template-assisted method, and electrochemical means, etc. [13]. The electrochemical anodization technique is considered as one of the most promising methods to produce TiO_2 nanotubes applied in PEC. This method was pioneeringly introduced in 1999, enabling the synthesis of 1D nanostructures and self-organized TiO_2 nanotubes (NTs through a straightforward anodization process applied to a

titanium sheet [12], [14]. As compared to the other morphologies of TiO_2, better charge transportation makes TiO_2 nanotubes as an interesting candidate for PEC devices. The bottleneck to apply TiO_2 as a photocatalyst lies in its bandgap energy as it only absorbs light in UV-region. Doping and heterostructure formation are promising routes to improve its light absorption. In this work, we prepared TiO_2 nanotubes along with the uniform V incorporation by single step anodization. Herein, we studied V doping in TiO_2 NTs or V_2O_5/TiO_2 NTs heterostructure formation via single step anodization. Furthermore, the experimental results were strengthened by doing the DFT calculation for V_2O_5/TiO_2. I invite the reader to explore the entirety of this work through the provided reference [15].

After the discovery of graphene in 2004, a lot of attention has been attracted by 2D materials because of their unique electronic, optical, magnetic, transport and photocatalytic properties [16]. Because of their remarkable properties, they have the potential to substitute noble metals (Pt, IrOx and RuO_x), they are extensively studied for PEC applications [17]. Because of their surface funcationization [16-17], large active surface area [18], and an excellent stackability for heterostructure formation [19] , the 2D materials are considered as promising candidates in energy storage, harvesting, and conversion. Recently, different 2D transition metal dichalcogenides like MoS_2 [20] , $PtSe_2$ [21], WS_2 [22], NbS_2 [23] WSSe [24] were developed and applied in the context of solar water splitting. There is ample room for the exploration of new 2D materials and their potential applications in renewable energy devices. In this work, new 2D material CrSSe was predicted by DFT calculations. On the bases of theoretical results, it was concluded that this material holds a strong potential for applications in the renewable energy. This research was published in the Journal of Crystal Growth & Design, with comprehensive details provided in the accompanying reference [25].

This thesis is divided into four comprehensive chapters.

In Chapter 1, we delve into the fundamental characteristics of Ta_3N_5 and its myriad of applications. We provide an introduction to semiconductors, exploring their various types, and offer a concise explanation of the semiconductor-electrolyte interface. Moreover, we investigate how the Ta_3N_5 system can contribute to present and future advancements in photoelectrochemical (PEC) water splitting.

Chapter 2 is dedicated to the intricate details of experimental procedures, equipment descriptions, and the fundamental underpinnings of Density Functional Theory (DFT) using the Quantum Espresso code.

In Chapter 3, we embark on a comprehensive study of both theoretical and experimental aspects, focusing on bandgap engineering, optical properties and PEC application of both pure and Mo doped Ta_3N_5.

In Chapter 4, we outlined the overarching conclusions of the thesis, shedding light on key insights. Additionally, this chapter delves into prospects for future work specifically focused on Ta_3N_5.

List of Publications from Current Project

- ✓ **H. Ullah**, A.U. Rahman, E.L. Aragão, F.F. Barbosa, K.G. Pergher,R. Giulian, H.C. Júnior, R.L. Sommer, S. Khan. Homogeneous V incorporation via single-step anodization: structural doping or heterostructure formation?. Applied Surface Science. **2021** Aug 1;556:149694.

- ✓ **H. Ullah,** I. Shehzadi, A.U. Rahman, M.W. Iqbal, S. Khan. Room Temperature Ferromagnetism in Hydrogenated Janus CrSSe Monolayer Using Quantum Monte Carlo Simulation. Crystal Growth & Design. **2022**.

Chapter 1 Semiconductor and their Potential Application for Photoelectrochemical Water Splitting

1.1 Introduction

The global population is rising day by day. According to a recent report by the United Nations in 2020, Earth's population exceeded 7 billion, with projections indicating that this number will grow to 9 billion by the year 2050 [25]. To provide huge amount of energy to our modern society with the steady growth in energy consumption is one of the big problems of the world, especially in the developing countries. As per the United States Energy Information Agency, the total global power consumption, catering to a population of over 7 billion people, currently stands at 15 terawatts (TW) and is projected to reach 30 TW by the year 2050 [26]. Most part of the energy used today comes from fossil fuels. In a short run we will be unable to keep up with this increasing demand because it depends on the available reserves [27]. The available reserves like coal, oil and gas on our planet are going to decrease very sharply. The International Energy Agency noted that oil production reached its peak in 2006 [25]. Since 2001, the prices of all types of fossil fuels have been on the rise and are not expected to return to the lower levels seen before 2001 [26].

One of the more serious concerns associated with the use of fossil fuels is its effect on our environment. When these fossil fuels like coal, oil and natural gas burn in the presence of oxygen greenhouse gases are produced. Among these greenhouse gases carbon dioxide (CO_2) has high impact on global warming [28]. The current industry energy matrix mostly relies on the fossil fuels. Thus, after the industrial revolution the CO_2 level in our environment was sharply risen from 294 to 394 part per million (ppm) and rising by 2ppm/year [29]. If the CO_2 level in our environment goes above 450 ppm, it will carry a high risk and rising the temperature of our environment by more than 2 ^oC. This high increase in temperature will affect our ecosystem and human society. Therefore, if we limit the increase to less than 2 ^oC than there is a greater chance for our society to adapt with this increase. It is one of the big problems for nowadays scientific society to reduce the CO_2 emission [30].

To reduce the CO_2 emission, exploring new sources of energy are highly demanding. These should be abundant, cheap, and large scale sustainable. Different

forms of sustainable energy sources are wind, hydroelectric, biomass, nuclear and solar. Among the various sources of energy mentioned above, solar energy stands out as having the potential to meet the entire energy demand of our modern society [31]. The amount of energy from sun striking the earth surface in one hour is more than that of the energy used by earth in one year [26]. The solar spectrum on the surface of earth is about 50% infrared (IR), 40% visible (V) and 10% ultraviolet (UV). The energy from sun is one of the good choices to fill the energy demand of our planet.

The above consideration shows that the route of solar energy conversion to hydrogen cannot be ignored. As we know, water is one of the abundant and most convenient resources of hydrogen. The energy used by the world in one year can be obtained from 3.5×10^{13} L of water in the form of hydrogen. This amount of water is roughly equal to the 0.01% of annual rain fall or 0.000002% of the water in World Ocean [27]. The hydrogen used by nowadays industry is generated by the steam methane reforming (SMR) method, which generates 5kg of CO_2 /kg of H_2. The annual discharge of CO_2 to the atmosphere is 240 mega ton in SMR method. The significant emission of CO_2 into the environment renders the SMR method as unsuitable for hydrogen production [7].

To sustain life on our planet smoothly and regularly we need to look for green energy sources, like to produce hydrogen from water. There are different mechanisms used to produce hydrogen from water by using solar radiation. These methods are photoelectrochemical (PEC) and photocatalytic water splitting, thermochemical conversion, photobiological methods, molecular artificial photosynthesis, and plasma chemical conversion [27]. One of the main advantages of PEC is that oxygen and hydrogen are produced at different electrodes. This process can be carried out at room temperature. The simple PEC cell is consisting of semiconductor working electrode and metal counter electrode [28]. A suitable wavelength excites the electron from the valance band (VB) to the conduction band (CB) of the semiconducting photoelectrode [29]. In the case of n-type semiconductor the photogenerated electrons go to the back of the semiconductor from where it is transferred to the counter electrode by external wire. These photogenerated electrons reduce water at counter electrode to produce hydrogen. The hole moves toward the semiconductor electrolyte interface to perform water oxidation reaction. There are different types of semiconductors that have been studied to split water. The benchmark to classify the photocatalytic devices is solar to hydrogen efficiency (STH) and for industrial applications, it should be over 10%. To

achieve STH, the most fundamental requirement for a semiconductor photoelectrode or photocatalyst is to absorb wide spectrum of the sun light and convert it into electron-hole pairs to split water into its constituent. For PEC water splitting, by using sunlight the semiconductor needs to fulfil some criterion. (i) The semiconductor ought to exhibit absorption within the visible region (ii) charge separation should be efficient (iii) it should present active surface area (iv) exhibit long term stability (v) and the valance band (VB) and conduction band of the semiconductor should straddle the water redox potentials [27]. Several oxides, nitride and 2D materials have been applied for solar water splitting, however, research is going on around the world to find out the best candidate that can fulfill all above mentioned requirements for overall water splitting.

1.2 Semiconductors and their properties

In solid state physics textbooks, a semiconductor is usually defined as a material having electrical resistivity that lies in between 10^{-2} to 10^{9} Ωcm^{-1} at room temperature. It can also be defined on the base of its bandgap energy, i.e., a material whose bandgap energy lies between zero to 4 eV (**Figure 1.1**) [30].

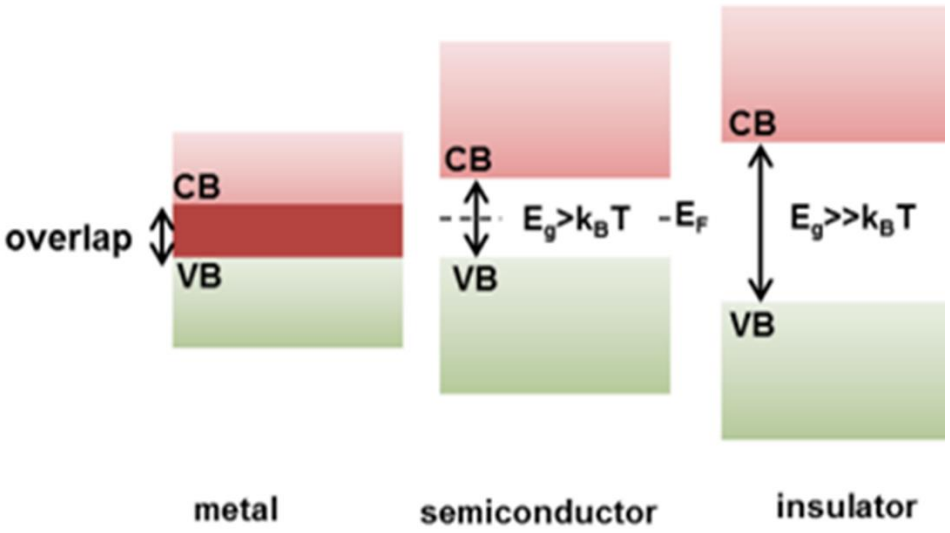

Figure 1-1 Energy diagram of metal, semiconductor and insulator. The CB, VB and EF represent the conduction band, valance band and fermi energy level, respectively [31].

The energy band diagram of semiconductor can be drawn if we plot the momentum k as a function of energies. This energy band diagram has filled and unfilled energy bands. The highest occupied molecular orbital (HOMO) is normally fully filled or partially filled with electrons in the semiconductors called the valance band of a

semiconductor. While the lowest unoccupied molecular orbital (LUMO) is called the conduction band. The bandgap of a semiconductor can be defined as the difference between the valance band and conduction band energies. The important property of a semiconductor can be extracted from the bandgap diagram of a semiconductor. The relative position of the valance band maximum (VBM) and conduction band minimum (CBM) with respect to the wave vector k has an important impact on the electronic properties of the semiconductor. If the VBM and CBM lie at same momentum k then the semiconductor is said to be direct bandgap semiconductor otherwise it is named as the indirect bandgap semiconductor. The highest occupied energy state of a system at absolute zero temperature is called the Fermi energy level. It is known that at absolute zero temperature the valance band of semiconductors is fully filled with electrons while the conduction band is empty. The probability of electron to jump from valance band to conduction band above absolute zero temperature is not likely to be zero. It means that the electron has a certain probability to occupy the excited state at room temperature. And this probability increases with increasing the temperature of the semiconductor [32]. The Fermi-Dirac distribution function can be used to spin half particles like electrons to find out how the electrons are distributed over the energy levels. According to the Fermi-Dirac distribution function, the probability of electron in a certain energy level with energy 'E' at some known temperature 'T' is given by the following equation

$$f(E) = \frac{1}{e^{\left(\frac{E-E_F}{K_B T}\right)}+1} \tag{1.1}$$

The above **Equation 1.1** is called Fermi-Dirac distribution function. Where E is the energy of certain energy level, E_F is the fermi energy, K_B is the Boltzmann constant and T is the certain known temperature. If the energy of an electron in an energy level is equal to the Fermi energy then the fermi-Dirac distribution function gives the probability equal to half. This result is consistent with the definition of fermi energy level. The density of states i.e., number of states per unit volume varies with varying the energy value. Consider that dE is the energy interval where we are interested to find the density of states for conduction band and valance band. The required density of states is given below [32].

$$g_c(E) = \frac{m_e^* \sqrt{2m_e^*(E-E_C)}}{\pi^2 \hbar^3} \tag{1.2}$$

$$g_V(E) = \frac{m_h^* \sqrt{2m_h^*(E_V - E)}}{\pi^2 \hbar^3} \quad (1.3)$$

In above **Equations 1.2 and 1.3** m_h^* and m_e^* are the effective mass of hole and electron, respectively. The constant $\hbar = \frac{h}{2\pi}$, E_C and E_V are the enrgy of the conduction band minimum (CBM) and valance band maximum (VBM) respectively. Similerly the hole density in valance band and the electron density in conduction band can be calculated by the following equations,

$$n_h = \int_{E_{Bottom}}^{E_V} g_v(E)\big(1 - f(E)\big)dE \quad (1.4)$$

$$n_e = \int_{E_C}^{E_{Top}} g_C(E) f(E) dE \quad (1.5)$$

In above **Equation 1.4**, E_{Bottom} is the energy of the bottom of valance band. In **Equation 1.5**, E_{Top} is the energy of the conduction band top and E_C representig the conduction band minimum energy respectively. For a semiconductor, the room temperature thermal excitation is not enough to excite the maximum number of electrons. It needs some external source to excite the electrons such as sunlight [33]. The populations of thermally excited charge carrier at room temperature is very low in most of the semiconductor as compared to the metals. This low populations of charge carriers leads to very low conductivity in pure semiconductor. At room temperature, the density of thermally excited electrons in metals is approximately 1×10^{28} electrons, whereas in pure semiconductors, the density is significantly lower, around 1.5×10^{13} electrons. This substantial difference in electron density imposes limitations on the practical applications of pure semiconductors [34]. To improve the conductivity of semiconductor, the impurity are introduced by doping. The doping process improves the conductivity of the semiconductor even if we keep the doping level of impurity very low, as 0.0001%.

1.2.1 p-type and n-type Semiconductor

In an intrinsic semiconductor, the number of holes in the valence band and the number of free electrons in the conduction band are equal. At above absolute zero temperature in an intrinsic semiconductor like silicon, there will be some electrons that are excited from valence band to conduction band that leads to charge flowing [35]. The doped semiconductor can be given the name extrinsic semiconductor. In an

extrinsic semiconductor, the introduction of foreign atoms through doping serves to enhance its conductivity across the entire crystal lattice. There are two types of external doping used in intrinsic semiconductors and as a result, we get two types of extrinsic semiconductors. One is an electron donor (n-type) and the other one is an electron acceptor (p-type). The electron donor dopant has a higher valency than the host atom, whereas the electron acceptor has a lower valency compared to the host atom. In n-type semiconductors the electrons are the majority charge carrier and holes are the minority. Due to the large number of free electrons in conduction band, the Fermi energy level in n-type semiconductor is shifted closer to the conduction band. The p-type semiconductor has holes as the majority charge carrier while electrons are minority charge carriers. In contrast to the n-type, the p-type has a lot of holes in the valance band, therefore, the Fermi energy level lies near to the valance band [32],[30].

1.3 Semiconductor electrolyte interface

When semiconductor is brought in contact with another semiconductor or metal, if both have different Fermi energy levels, then after the contact there is a charge transfer between them until the equilibrium is established. After the equilibrium, there is no charge transfer. The semiconductor has one of the main features that is the presence of space charge or built of electric field within the semiconductor when it is brought in contact with another semiconductor, metal, or electrolyte [32]. When n-type semiconductor is immersed in an electrolyte the band bending across the semiconductor electrolyte interface is caused by this electric field which plays an important role in effective charge separation (**Figure. 1.2**). For an ideal n-type semiconductor which is in contact with electrolyte, the electrons are transferred from semiconductor to the electrolyte. This phenomenon of charge transfer continues until equilibrium is reached. After the equilibrium is achieved the fermi level of semiconductor and redox level of electrolyte lie at the same position. As a result, we get the bands bending in an upward direction. Near to the semiconductor surface, there is a region where the electrons concentration is depleted. This region is given the name space charge region or depletion region.

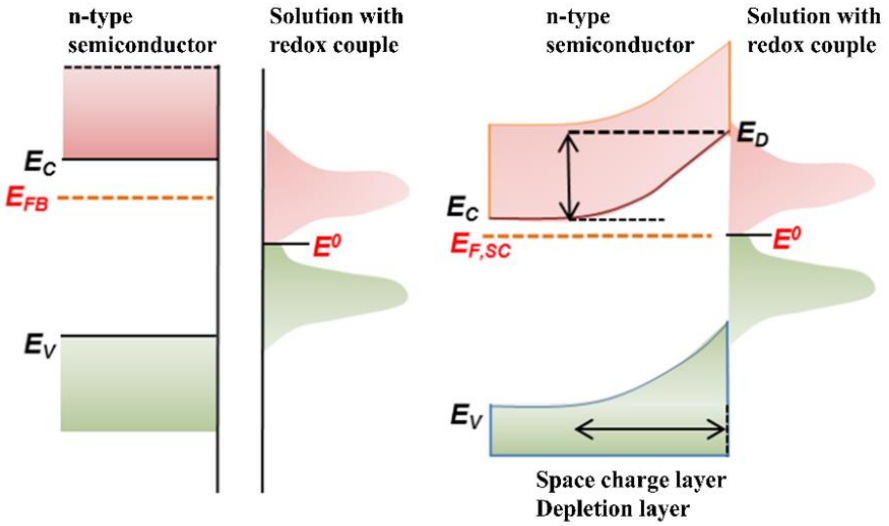

Figure 1-2 Semiconductor electrolyte interface for n-type semiconductor [31] .

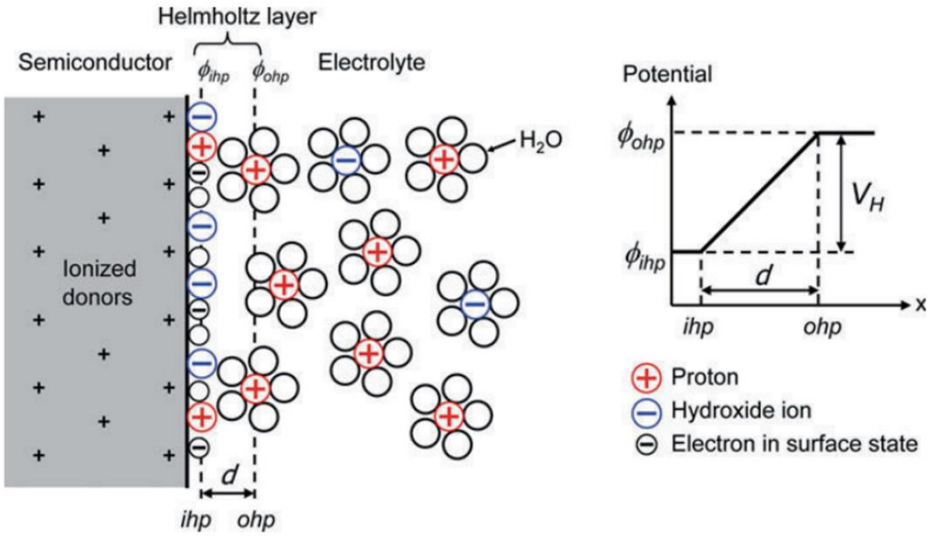

Figure 1-3 Schematic diagram of the semiconductor/electrolyte interface and the Helmholtz layer. The outer Helmholtz plane (ohp) marks the distance of closest approach for ions still in the solution. The inner Helmholtz plane (ihp) consists of H^+ and OH^- ions that are specifically adsorbed at the semiconductor surface [27] .

The Helmholtz layer has a thickness of ~2-5 Å. There is some potential drop across the Helmholtz layer and this drop is in the order of ~ 0.1→0.5V. The Helmholtz capacitance is about 10─20 μFcm^{-2} [36]. Furthermore, the width of band bending can be calculated by using the Poisson equation,

$$\frac{d^2\varphi(x)}{dx^2} = \frac{-eN_D}{\varepsilon_0\varepsilon_r} \quad (0 \le x \le w) \tag{1.6}$$

Where w, is the width of depletion region is, ε_0 is the permittivity in vacuum, ε_r is the relative permittivity and N_D is the donor atom density. The solution of the above equation is given below,

$$\varphi(\mathrm{x}) = \frac{\mathrm{eN_D}}{\varepsilon_0 \varepsilon_\mathrm{r}}\left(\mathrm{wx} - \frac{1}{2}\mathrm{x}^2\right) - (\mathrm{V_D} - \mathrm{V_{FB}}) \tag{1.7}$$

When $x = w$

$$\mathrm{w} = \left(\frac{2\varepsilon_0 \varepsilon_\mathrm{r}}{\mathrm{eN_D}}(\mathrm{V_D} - \mathrm{V_{FB}})\right)^{\frac{1}{2}} \tag{1.8}$$

In above equation e is the elementary charge on electron, V_D potential drop in the depletion region. V_{FB} is the flat band potential when there is no band bending i.e., band becomes flat. The flat band potential is generally used to find the position of the conduction band and valance band in semiconductor. It can be measured experimentally by applying the Mott-Schottky equation, which is given below,

$$\frac{1}{c^2} = \frac{2}{A^2 e \varepsilon_0 \varepsilon_r N_D}\left(V_{app} - V_{FB} - \frac{kT}{e}\right) \tag{1.9}$$

Where, V_{app} is the applied potential, A is the surface area. The flatband potential can be found out if the $\frac{1}{c^2}$ is ploted against the applied voltage. The intercept on the potential axis gives the flatban potentail value [37]. All the above formulas are valid only for an ideal semiconductors.

1.4 Photoelectrochemical cell

The photoelectrochemical (PEC) cell consists of three electrode systems. These electrodes are working electrode, reference electrode and counter electrode. The working electrode is made of semiconducting material. The main component of PEC cell is the working electrode. When the light of suitable wavelength falls on the working electrode, the electron hole pairs are generated. These electron hole pairs are separated from each other due to the electric field present inside the semiconductor. If the working electrode is made from n-type semiconductor, then the photogenerated electron moves toward the conducting back of working electrode from where it is transported to the counter electrode by external wire. At the surface of counter electrode, it reduces the water to produce hydrogen. The photo-generated holes are swiped toward the surface of the working electrode to oxidize water to produce the oxygen.

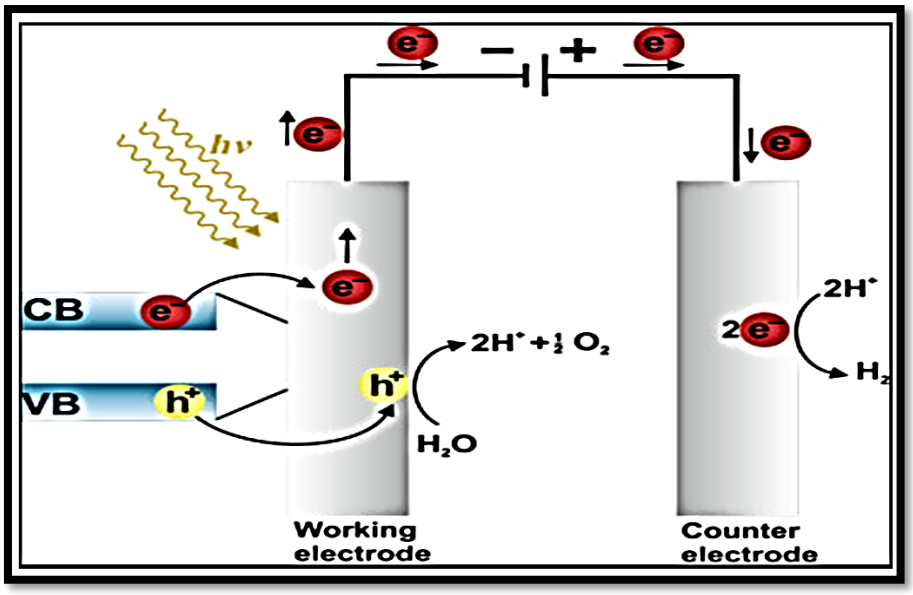

Figure 1-4 Schematic diagram of PEC water splitting [38].

Overall water splitting process is given below,

$$4\mathrm{H_2O} + 4\mathrm{e^-} \rightleftarrows 2\mathrm{H_2} + 4\mathrm{OH^-} \tag{1.9}$$

$$4\mathrm{OH^-} + 4h^+ \leftrightarrows 2\mathrm{H_2O} + O_2 \tag{1.10}$$

The whole setup is shown in the above **Figure. 1.4**.

The Gibbs free energy for overall water splitting can be found out by the following expression.

$$\Delta G = -nF\Delta E \tag{1.11}$$

In above expression ΔG is Gibbs free energy, F is the Faraday constant, ΔE is the cell potential which is ($\Delta E = E^{o}_{\text{cathode}} - E^{o}_{\text{anode}}$). At standard temperature 298 K, pressure 1bar and $\Delta E = -1.229$, the change in the Gibbs free energy is 237 kJ/mol for H_2. The positive change in Gibbs free energy shows that the water splitting process is thermodynamically endothermic process like uphill.

1.5 Photoelectrochemical water splitting

Approximately 71% of Earth's surface is covered by water, making it a valid assertion that water is indeed life's essential component for all living organisms on our planet.

*"Conserve water **even if you were on the banks of a flowing river."***

(Prophet Muhammad PBUH)

Photoelectrochemical (PEC) water splitting was first reported by K. Honda and A. Fujishima by using TiO_2 photoanode in 1970s. After A. Fujishima and K. Honda a large attention has been attracted to split water by using semiconductor photoanode and sunlight. In PEC water splitting, the sunlight is used to split the water into hydrogen and oxygen. This method is environmentally friendly because it does not produce carbon dioxide [42]. The bandgap of the semiconductor is very important to drive efficient water splitting. The water splitting reaction is given below.

$$H_2O + 2h\nu \rightarrow \frac{1}{2}O_2 + H_2 \qquad (1.12)$$

The change in Gibbs free energy to convert one molecule of water into O_2 and H_2 at standard temperature and pressure is 237 kJ/mol. Hence, the change in free energy is positive as we discussed earlier, the water splitting process is uphill. In simple words we can say that we need an external source to drive the process. In electrolysis, the minimum potential needed to be applied between the two electrodes to drive the water splitting process should be 1.23V. This reaction can be driven by using semiconductors and sunlight. Therefore, the semiconductor absorbs the photon with energy greater than 1.23 eV (wavelength equal to 1008 nm).

The conventional PEC cell is composed of three electrodes (**Figure. 1.5**). These electrodes are reference, working, and counter electrode. In all our experiments we will use the Ag/AgCl electrode as a reference electrode. There are three different scales used for water oxidation and reduction. That is Reversible Hydrogen Electrode scale (RHE) Normal Hydrogen Electrode (NHE) scale and standard hydrogen electrode scale (SHE). According to the RHE scale, the water oxidation and reduction occur at 1.23 V and 0 V vs RHE, respectively, which is independent of the pH of the water based electrolyte. To convert the potential of Ag/AgCl electrode to RHE, we used the Nernst equation, which is given below.

$$E_{RHE} = E^0_{Ag/AgCl} + E_{Ag/AgCl} + 0.059 \times pH \qquad (1.13)$$

Where $E^0_{Ag/AgCl}$ corresponding to standard reference potential of Ag/AgCl electrode at 25℃ and its value equal to 0.197 V, $E_{Ag/AgCl}$ refers to the applied bias potential and pH correspond to the potential hydrogen of the electrolyte. The PEC water splitting has an advantage over the pure electrolysis because the PEC use the sunlight as compared

to electrolysis for water splitting, while in electrolysis the electricity come from another source to split water which, may or may not be the green energy.

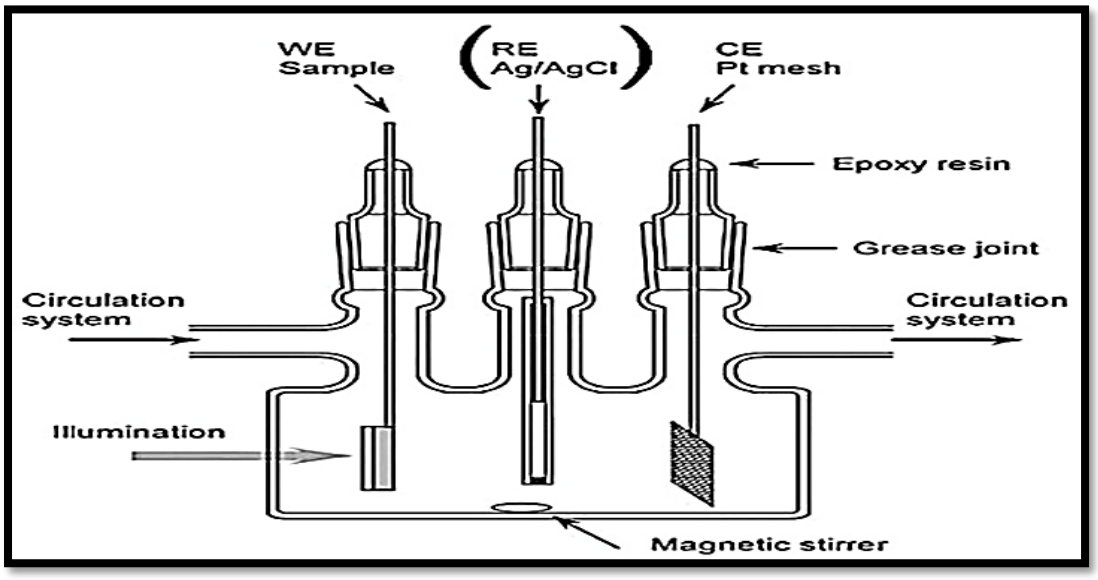

Figure 1-5 Three electrodes PEC Cell configuration [39].

1.6 Photocatalysts for water splitting

Several metal nitrides and oxynitrides (e.g., Ta_3N_5, TaON, $LaTaON_2$, $LaTiO_2N$, etc.) and oxides (TiO_2, WO_3, $SrTiO_3$, Fe_2O_3, and Cu_2O) [8] attracted a lot of attention because of their suitable bandgaps and band edge positions to split water [43]. In addition, 2D materials like CdS, WSSe, g-C_3N_4, MoSSe, PtSSe and CrSSe also presented a great promise for water splitting [8], [44]. However, there is a lot of room available to discover more materials with potential energy applications. Research is going on to discover the material of the future that can be utilized for overall water splitting.

1.6.1 Ta_3N_5 as photocatalyst

Oxides semiconductor photocatalyst such as, TiO_2, Fe_2O_3, WO_3, $NaTaO_3$, $SrTiO_3$ and $BiVO_4$ [40] have been applied in PEC devices to split water. All these metal oxides are stable in water, and typically earth plentiful compounds. Unfortunately, due to wide bandgap the metals oxide such as TiO_2 ($E_{g\sim}$3.1 eV), and Ta_2O_5 ($E_{g\sim}$3.9 eV) etc. harvest only a small portion of solar spectrum [41]. The valance band of transition metal oxides mainly consists of O 2p orbitals. By nitridation process, the phase change occurs from oxide to nitride by changing the VB from O2p to N2p orbitals, thereby, decreasing

the bandgap energy. Therefore, opening up the possibility to engineer the oxide bandgap to utilize most part of the solar energy [41].

In nitride semiconductors, Ta_3N_5 has been emerged as one of the promising candidates for overall water splitting as a photocatalyst or photoanode due to its suitable bandgap and band position. To synthesize Ta_3N_5, the oxygen in Ta_2O_5 is replaced by nitrogen as [42], [31].

$$\frac{3}{2}Ta_2O_5 + 5NH_3 \rightarrow Ta_3N_5 + \frac{15}{2}H_2O \qquad (1.14)$$

Ta_3N_5 has an experimental bandgap of 2.1 eV while a theoretical band gap of 2 eV [21]. To improve the photocatalytic performance of Ta_3N_5 there are several nano-morphology like Nanorods (NRs) [22], Nanoparticles, Nanotubes (NTs) [23], have been developed and studied. Among all these previously stated nano-morphologies, the 1D NTs of Ta_3N_5 have a good charge transport property as well as a large surface area, which makes it suitable candidate for PEC applications. The 1D Ta_3N_5 NTs was first prepared by Feng et al in 2010 by nitridation of amorphous Ta_2O_5 NTs [23]. A short comparison of the previous literature on Ta_3N_5 as a photoanode (**Table 1.1)** and suspended particles (**Table 1.2**) system is presented in the tables below.

Table 1-1 Tantalum nitride photocatalysts for solar water splitting in the PEC system.

Photoelectrode	Preparation	Doping	Catalyst	Electrolyte	IPCE	Photocurrent ($mAcm^{-2}$)	Ref
Ta_3N_5	Oxidation and Nitridation	NA	NA	KOH (1M)	4.8%	0.5 at 1.5V RHE	[11]
Ta_3N_5	Oxidation and Nitridation	NA	$Co(OH)_x$	NaOH (1M)	50%	5.5 at 1.23V RHE	[11]
Ta_3N_5	Oxidation and Nitridation	NA	NA	KOH (1M)	5.3%	NA	[43]
Ta_3N_5	Oxidation	NA	Co_3O_4	Na_2SO_4 (PH=11)	9%	1.3 at 0.7 V Ag/AgCl	[44]

	and Nitridation						
Ta_3N_5	Oxidation and Nitridation	Zr	$Co(OH)_x$	KOH (1M)	NA	7.2 at 1.23 V RHE	[45]
Ta_3N_5	Oxidation and Nitridation	W	$Co(OH)_x$	KOH (1M)	NA	4 at 0.5V Ag/AgCl	[46]
Ta_3N_5	Mask anodization	Ba	CoPi	K_2HPO_3	55%	6.7 at 1.23V RHE	[47]

Table 1-2 Tantalum nitride photocatalysts for solar water splitting.

Photocatalyst	Synthesis	Catalyst	Light Source	Solution	H_2 ($\mu mol\ h^{-1}\ g^{-1}$)	O_2	Ref
Ta_3N_5	Nitridation	None	300 W	$AgNO_3$	NA	2100	[48]
Ta_3N_5	Templating and nitridation	Pt(0.5Wt %)	450 W	Methanol	156	NA	[49]
Ta_3N_5	Nitridation	Pt(3 Wt %)	300 W	Methanol	9	NA	[49]
Ta_3N_5	Templating and nitridation	Pt(3 Wt %)	300 W	Methanol	175	NA	[50]
Ta_3N_5	CVD and nitridation	Pt(3 Wt %)	300 W	Methanol	17	NA	[51]
Ta_3N_5	Homogeneously chemical reduction	None	300 W	$AgNO_3$	2050	NA	[52]

Though the theoretical solar to hydrogen (STH) energy conversion efficiency of Ta_3N_5 is 15.9%, and theoretical photocurrent density is 12.9 $mAcm^{-2}$ yet they were not achieved experimentally (**Table 1 & 2**) [53]. Intensive efforts have been made to improve the STH efficiency of Ta_3N_5 and despite these efforts the highest efficiency achieved so far is 2.72%, which is still very low as compared to the theoretical value[11] . From the bandgap diagram (**Figure. 1.6**) of Ta_3N_5 it's clear that the conduction band

is more negative with respect to the water reduction potential while the valance band is more positive as compared to the water oxidation potential.

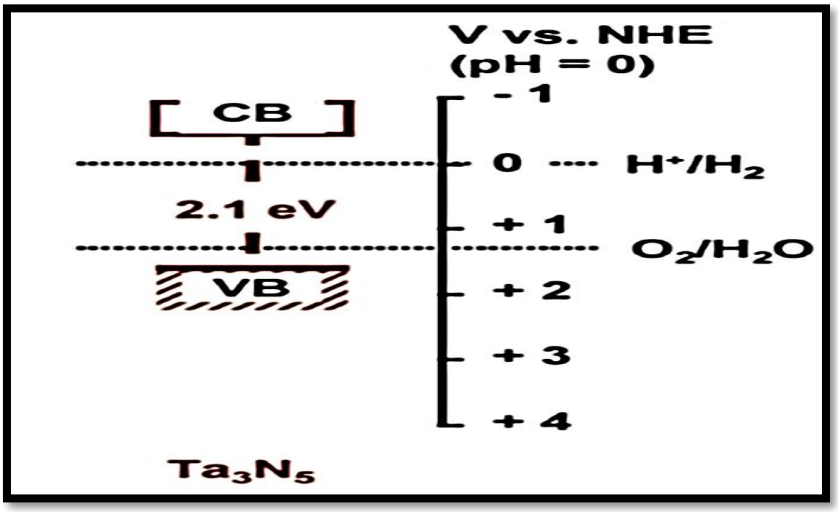

Figure 1-6 Bandgap position of Ta_3N_5 measured at pH=0 [31].

The main obstacle in using Ta_3N_5 for overall water splitting is the apparent imbalance in the water reduction and oxidation capacities [47]. Upon comparison we can realize that the photocatalytic reduction activity of Ta_3N_5 is much poorer or in some cases even undetectable as compared to water oxidation [54] due to the defects induced by the nitridation process which act as electron traps [55], [56]. The main challenges related to Ta_3N_5, which limit its photocatalytic activity are its poor stability in electrolyte, low photo voltage, mismatch between hole diffusion length and light absorption depth and self-oxidation [9]. To improve the electronic and optical properties of Ta_3N_5, a variety of modification were suggested including, particles size reduction, doping of foreign element, heterojunction formation and surface modification [57]. These previous studies showed that the doping of foreign element and co-catalyst loading are one of the valuable techniques to improve the PEC properties of Ta_3N_5.

1.6.1.1 Crystal and electronic structure of Ta_3N_5

Ta_3N_5 was firstly synthesized in 1964, by H. Funk and H. Bohland by heating the Ta_2O_5 powder in ammonia rich atmosphere [58]. Ta_3N_5 contains different crystal structures reported in the literature [59]. The conventional unit cell of Ta_3N_5 is

composed of 32 atoms. The experimentally measured lattice constant is $a = 3.89$ Å, $b = 10.22$ Å and $c = 10.27$ Å [31]. The space group of Ta_3N_5 is cmcm. The density of Ta_3N_5 is about 9.75 gcm^{-3} with constituent oxidation states are N^{3-} and Ta^{5+}. The crystal structure is shown in the **Figure. 1.7.** Each Ta atom is connected with six N atoms while each N atom has 3 or 4 nearest Ta atoms. Furthermore, the theoretical bond length between Ta and N is 2.10Å and similarly the bond length between Ta and Ta is 3Å.

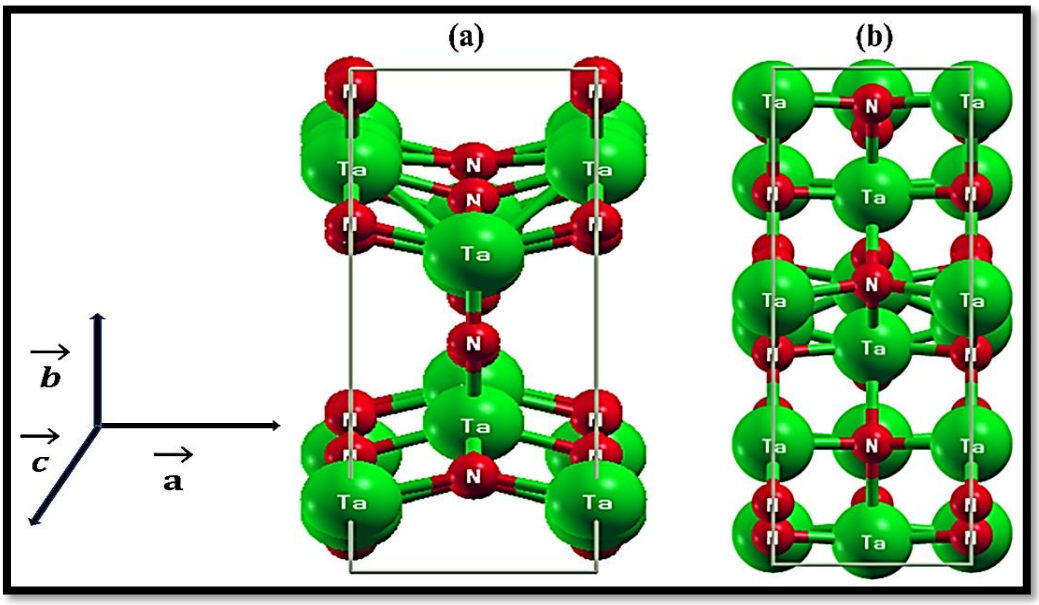

Figure 1-7 (a) Crystal structure of Ta_3N_5 unit cell, (b) represent the top view of Ta_3N_5 unit cell. The crystal structures presented above were generated by using crystalline and molecular structure visualization program *(*XCrySDen*)*

The electronic bandgap structure of Ta_3N_5 was calculated by C. Fang et al, in 2001 by using the density functional theory. The electronic band gap calculations in literature show that the valance band is composed of N 2p orbitals while the conduction band is mainly due to the Ta 5d orbitals [29]. The Ta 5d orbitals have non vanishing density of states in the valence band which shows us that the interaction between N and Ta is covalent. The theoretical calculated indirect and direct band gap are 1.1 eV and 1.4 eV, respectively. The experimental band gap of Ta_3N_5 is 2.1 eV [60]. Generally, this under estimation in the theoretical bandgap is attributed to the GGA calculation.

1.6.1.2 Factors that limit Ta_3N_5 photocatalytic performance

Ta_3N_5 is a promising candidate for PEC water splitting, however, with above all these properties, it faces the following two critical issues (i) low photovoltage and (ii) poor stability in aqueous electrolyte. The low photovoltage i.e., V_{low}, is the lowest potential at which nonzero photocurrent is measured also known is onset potential, generally > 0.6V [61], [62]. To address this issue, significant efforts have been made. Recently, tremendous improvement was achieved by Seo et al, by improving this value to 0.55V via doping and surface modification technique [62]. The fact behind the poor performance of Ta_3N_5, in terms of photovoltage, still poorly understood. The photocurrent [62] of Ta_3N_5 abruptly decreases more than 50% within the first few minutes of water splitting reaction [57]. Wang et al revealed that the issue of low photovoltage and poor stability are caused by growth of a thin oxide layer on the surface of Ta_3N_5. This oxide layer pins the fermi energy level and leads to the complete suppression of the photocatalytic activity. Thus, further study is needed to clearly investigate it. Similarly, the degradation of Ta_3N_5 in electrolyte is also unclear [51]. To improve the stability, protective layers such as NiFeOOH, $Co(OH)_x$ and CoFeOOH were utilize [63]. The conduction band of Ta_3N_5 is mainly composed of Ta 5d states and it is known that high temperature nitridation induces electron traps near the conduction band due to reduced Ta species [55] . Adding a dopant with unoccupied d states may decrease the formation of electron traps. Mo is a transition metal with unoccupied 4d states and recently used to improve the electronic structure of other semiconductors such as $BiVO_4$ [64], [48]. Due to Mo doping, localized states closed to the CB of $BiVO_4$ were identified thus an extension to the CB was achieved which improved electronic and optical properties of the material. This also opens up the possibility to decrease the electron traps in Ta_3N_5. However, for efficient doping and charge compensation, the oxidation state of the dopant should also be considered [48]. The ionic radii of Mo^{4+} (65 Å) is comparable to Ta^{5+} (64 Å). Hence, we anticipate that Mo^{4+} could serve as a promising candidate for enhancing the electronic structure and optical properties of Ta_3N_5. In this study, we performed DFT calculations and successfully synthesized Mo-doped Ta_3N_5 using experimental techniques.

1.7 Novelty and objective of our work

This work focuses on the experimental and theoretical investigation of semiconducting material Ta_3N_5. Ta_3N_5 emerged as a promising photocatalyst due to its capacity to absorb a broad spectrum of visible light and its band positions that straddle the redox potential of water. However, the high-temperature nitridation process to synthesize Ta_3N_5 results the formation of reduced species ($Ta^{4+/3+}$) which act as a shallow donor states and nitrogen vacancies that act as electron-hole (e^-/h^+) recombination centers. The presence of reduced species and nitrogen vacancies significantly impacts the photoelectrochemical (PEC) performance of Ta_3N_5. Adding metal dopants with unoccupied d states in Ta_3N_5 possess strong potential to extend the conduction band that may suppress the shallow donor states, thereby decreasing the e-/h+ recombination centers and enhancing the PEC activity of Ta_3N_5. Herein, we followed a theoretical and an experimental technique of foreign metals element Mo doping in Ta_3N_5 to enhance its opto-electronic properties for PEC water splitting. The electronic and optical properties of pure and Mo doped Ta_3N_5 were calculated by using Density Functional Theory calculations within the generalized gradient approximation (GGA-PBE) implemented in Quantum Espresso package. The GGA approximation was refined using the GGA+U functional. Subsequently, the material was synthesized through experimental means, characterized, and subsequently applied in photoelectrochemical (PEC) applications. To the best of our knowledge, Mo doping in Ta_3N_5 nanotubes has not been reported in the previous literature indicating toward novelty of this work.

Chapter 2 Theoretical and experimental background

Density functional theory (DFT) has been the predominant approach to quantum mechanical simulation of periodic systems for the last forty years [26, 27]. Quantum chemists have also embraced it in recent years, and it is currently extensively utilized for the simulation of energy surfaces in molecules. First-principles methods combined with the advancement of computer power over the past decades have provided fast and reliable results for a wide range of problems in the materials science, such as microelectronics, energy storage or the prediction of new functional materials. First principle methods are adopted to solve Schrödinger's equation, which governs the behavior of electrons in a system. Density functional theory (DFT) offers an effective solution to these issues by providing an approximate description of a system's ground state. The computational cost of DFT is very low compared to other techniques like quantum Monto Carlo, therefore DFT is one of the useful techniques in recent days to solve a lot of problems in material science.

This chapter is composed of two parts. (i) Theoretical background related to DFT (ii) The experimental procedures used in this project.

2.1 Theoretical procedures

2.1.1 Density functional theory

Density functional theory (DFT) is one of the successful theories to predict the electronic structure of atoms, molecules, and solids. DFT is not only useful in condensed matter physics but also in chemistry and biochemistry. It’s called density functional because the function density itself is a function of position. DFT uses the electron density to predict the ground state energy of the system instead of the electron wave function. The use of the electron density reduces the multidimensional many electrons system into three-dimension system; that makes the system easy to be solved. So, the DFT is one of the easiest way to approximately solve the many bodies Schrödinger wave equation. DFT is computationally feasible even for large systems [65] . The DFT was established on Hohenberg–Kohn and Kohn–Sham theorems. These theorems will be reviewed in this section.

2.1.2 Schrodinger wave equation

The Schrodinger wave equation is linear second order partial differential equation. It describes the wave function of an electron. This equation is one of the key results in the field of quantum mechanics. However, it was first derived by Erwin Schrodinger in 1925 and published in 1926. Based on his work, he was awarded with the Nobel Prize in Physics in 1933. The time independent Schrodinger wave equation for a single nonrelativistic particle in three dimensions is.

$$\left[\frac{-\hbar^2}{2m}\nabla^2 + V(r)\right]\psi(r) = E\psi(r) \qquad (2.1)$$

Here, $\hbar = \frac{h}{2\pi}$, is the reduced Plank's constant, m is the mass of electron,

∇^2 is Laplacian,

V(r) is the potential energy of an electron,

$\psi(r)$ is the electron wave function and E is the energy Eigen value of Hamiltonian operator.

For a system like hydrogen atom or single ionized helium atom it is easy to solve the Schrödinger equation and find out the ground state energy for the system. But in the case of many bodies system, where we have more than one electron it is very hard to solve the Schrödinger wave equation. The time independent Schrodinger wave equation for many bodies system is given below,

$$\left[-\sum_I^N \frac{\hbar^2}{2M_I}\nabla^2_{\vec{R}_I} - \sum_i^N \frac{\hbar^2}{2m_i}\nabla^2_{\vec{r}_i} + V(r,R)\right]\psi(r,R;t) =$$

$$\iota\hbar\frac{\partial}{\partial t}\psi(r,R;t) \qquad (2.2)$$

In above **Equation (2.2)** $V(r,R)$ represent the coulombic interactions between nucleus-nucleus, electron-electron and nucleus-electron. The mathematical form of this interaction is given below,

$$V(r,R) = \sum_{I\neq J}^N \frac{e^2}{2}\frac{Z_I Z_J}{|\vec{R}_I - \vec{R}_J|} - \sum_{i,J}^N e^2\frac{Z_J}{|\vec{r}_i - \vec{R}_J|} + \sum_{i\neq j}^N \frac{e^2}{2}\frac{Z_I Z_J}{|\vec{r}_I - \vec{r}_j|} \qquad (2.3)$$

In above **Equation (2.3)** 'r' represents the positions of electron while the 'R' represents the position of nuclei.

Put the above **Equation (2.3)** in **Equation (2.2)** we get,

$$\left[-\sum_I^N \frac{\hbar^2}{2M_I}\nabla^2_{\vec{R}_I} - \sum_i^N \frac{\hbar^2}{2m_i}\nabla^2_{\vec{r}_i}\right]\psi(r,R;t) + \left[\sum_{I\neq J}^N \frac{e^2}{2}\frac{Z_I Z_J}{|\vec{R}_I-\vec{R}_J|} - \sum_{i,J}^N e^2\frac{Z_J}{|\vec{r}_i-\vec{R}_J|} + \sum_{i\neq j}^N \frac{e^2}{2}\frac{Z_I Z_J}{|\vec{r}_I-\vec{r}_j|}\right]\psi(r,R;t) = \iota\hbar\frac{\partial}{\partial t}\psi(r,R;t) \quad (2.4)$$

Obtaining the exact solution to the aforementioned equation is exceptionally challenging. To solve Equation (2.4) for a system involving multiple bodies, the application of certain approximations becomes necessary. The Born-Oppenheimer approximation is one of the basic approximations in condensed matter physics. This approximation is based upon the fact that the electron is lighter as compared to the nucleus. Similarly, the proton is 2000 times heavier than electron. Because of this fact Max Born and Robert Oppenheimer considered the nucleus to be at rest. So, this approximation allowed us to separate the nuclei motion from the motion of electron. After the Born-Oppenheimer approximation the kinetic energy of nucleus vanishes and the columbic interaction term between nuclei contribute a constant to the ground state energy of the system.

The time independent Schrödinger wave equation for many electrons system interacting with different nuclei is given by;

$$\left[-\sum_i^N \frac{\hbar^2}{2m_i}\nabla^2_{\vec{r}_i} - \sum_{i,J}^N e^2\frac{Z_J}{|\vec{r}_i-\vec{R}_J|} + \sum_{i\neq j}^N \frac{e^2}{2}\frac{1}{|\vec{r}_i-\vec{r}_j|}\right]\psi(r,R;t) = E\,\psi(r,R;t) \quad (2.5)$$

Here, the first term is the kinetic energy of an electron,

While the second term represent the columbic interaction between electron at position $\vec{r}_i$ and nucleus at position $\vec{R}_J$.

The third term is the caulomic interaction between two electrons that are located at position $\vec{r}_i$ and $\vec{r}_j$. The factor $\frac{1}{2}$ in last term comes to avoid the double counting of Coulomb interaction.

2.2 The Hohenberg-Kohn theorems

As discussed above, the DFT is developed on the basis of two mathematical theorems. These theorems are published by Hohenberg–Kohn and Kohn–Sham in 1964 and known as Hohenberg-Kohn theorems [66] .

Theorem I: According to the first theorem there is one-to-one correspondence between the ground state electron density $n_0(r)$ and external potential $V_{ext}(r)$, or in simple words different ground state electron density must correspond to different external potentials.

Theorem II: For a given external potential $V_{ext}(r)$, we can define an energy functional $E[n]$ such that,

$$E[n] = \int dr[n[r]V_{ext}(r)] + G[n] \quad (2.6)$$

In above **Equation (2.6)** the energy functional will take its minimum value at the ground state electron density $n_0(r)$ and the value of the functional at that density is minimum i.e., ground state energy E_0. For any trial density of electron $n(r)$, the variational principle says that,

$$E_0 = E[n_0(r)] = <\psi_0[n_0(r)]|H|\psi_0[n_0(r)]> \leq <\psi_0[n(r)]|H|\psi_0[n(r)]> \quad (2.7)$$

It will be equal if, $n_0(r) = n(r)$

It means that we can get the ground state energy without the explicit knowledge of the many electrons ground state wave function. The exact ground state density of many electrons system gives the lowest energy.

2.3 Kohn-Sham equation

The Hohenberg-Sham theorem shows that the ground state density can be used to predict the properties of solid system. But these theorems do not say anything about how to find the ground sate density. After Hohenberg-Sham theorem's it was an open question. In 1965 Kohn-Sham provide a way to find out the ground state density. According to Kohn-Sham the ground state density as a functional of charge density and is given by [66].

$$E[\rho(r)] = T[\rho(r)] + \int \rho(r)V(r)dr + E_{ee} \quad (2.8)$$

The first term in the above equation represents kinetic energy, the second term represent the electron nuclei interaction, while the third term represent the electron-electron interaction. The third term can be written in new form as;

$$E_{ee}[\rho(r)] = \frac{1}{2}\int \frac{\rho(r)\rho(r')}{|r-r'|} dr dr' + E_{xc}[\rho(r)] \quad (2.9)$$

Here, the first term on right hand side gives the coulomb interaction between two electrons located at position $r\ and\ r'$. The second term is the exchange correlation energy.

Adding **Equation (2.9)** in **Equation. (2.8)**, we get,

$$E[\rho(r)] = T[\rho(r)] + \int \rho(r)V(r)dr + \frac{1}{2}\int \frac{\rho(r)\rho(r')}{|r-r'|} drdr' + E_{xc}[\rho(r)] \quad (2.10)$$

The charge density $\rho(r)$ can be defined as,

$$\rho(r) = \sum_{i=1}^{n} \psi_i^*(r)\psi_i(r) \quad (2.11)$$

Here 'n' represents the number of electrons.

Taking functional derivative $\frac{\delta E[\rho(r)]}{\delta \psi_i^*(r)}$ with the constraint that each $\psi_i(r)$ is normalized to unit leads to:

$$\left(\frac{-\hbar^2\nabla^2}{2m} + V_{KS}\right)\psi_i(r) = \epsilon_i\psi_i(r) \quad (2.12)$$

Here,

$$V_{KS} = \int \frac{\rho(r')}{|r-r'|} dr' + V(r) + V_{xc}(r) \quad (2.13)$$

The first term in the above **Equation. (2.13)** is Hartree potential. The second term corresponds to the local ionic potential. The third term referred to the exchange correlation potential. The exchange correlation potential can be defined as

$$V_{xc}(r) = \frac{\delta E_{xc}[\rho(r)]}{\delta \rho(r)} \quad (2.14)$$

The above equation **Equations. (2.11-2.14)** can be solved self consistently. The procedure for self-consistent field method is follows.

1. The initial trial electron density $\rho(r)$ should be defined.
2. To find out the Kohn-Sham orbitals $\psi_i(r)$ we should use the initial trial density to solve the Kohn-Sham equation.
3. The Kohn-Sham electron density should be calculated from step II.

$$\rho_{KS}(r) = \sum_i \psi_i^*(r)\,\psi_i(r) \quad (2.15)$$

4. The process can be repeated until the convergences are achieved. $|\rho_{KS}(r) - \rho(r)| < CC$, here CC is the convergence criterion. After the convergence is reached, we can calculate the final total energy of the system.

2.4 Exchange-correlation functional

The exact form of the exchange correlation functional is still unknown. Different approximation has been made to find out the exchange correlation functional. Among these different approximations the most widely used in DFT calculation are Local Density Approximation (LDA) [66] and Generalized Gradient Approximation (GGA) [65]. In the case of LDA, the solid system is taken as uniform electron gas, where the density is uniform everywhere in space. The exchange-correlation functional in case of LDA is given by,

$$E_{xc}[\rho] \cong E_{xc}^{LDA} = \int dr\ \rho(r)\epsilon_{xc}\rho(r) \tag{2.16}$$

As we discussed above, in LDA the density is the same at every place. Due to this approximation the exchange energy is underestimated while the correlation energy is overestimated. To overcome on these deficiencies another approximation is used known is GGA [67], [65]. In GGA the density is not uniform everywhere in space and the electron density is expanded in term of density gradient. The exchange-correlation functional in case of GGA [68] is given by,

$$E_{xc}[\rho] \cong E_{xc}^{GGA} = \int dr\ \rho(r)\epsilon_{xc}(\rho(r), \nabla\rho(r)) \tag{2.17}$$

Here, $\nabla\rho(r)$ is the density gradient.

2.5 Bloch theorem and K-space

It is known that atoms are arranged in crystals in a periodic manner. The infinite repetition of a unit cell in three dimensions makes a crystal. The entire crystal can be studied by studying the unit cell because crystal is the periodic repetition of unit cell. The position vector of atom in Cartesian coordinate system is given by the following equation.

$$\vec{r} = n_1\overrightarrow{a_1} + n_2\overrightarrow{a_2} + n_3\overrightarrow{a_3} \tag{2.18}$$

Where $\overrightarrow{a_1}$, $\overrightarrow{a_2}$ and $\overrightarrow{a_3}$ are lattice vector along X, Y and Z direction respectively and n_1, n_2 and n_3 are integers.

The Block theorem can be defined as 'For periodic potential the solution of the Schrodinger wave equation will be the sum of the following terms.

$$\psi_k(r) = u_k(r)e^{\iota\vec{k}.\vec{r}} \tag{2.19}$$

$u_k(r)$ is the periodic potential and can be written as,

$$u_k(r) = u_k(r + n_1\overrightarrow{a_1} + n_2\overrightarrow{a_2} + n_3\overrightarrow{a_3}) \tag{2.20}$$

Here, $u_k(r)$ is periodic. From this we can see that using Bloch theorem; we can solve Schrödinger equation for each $\vec{k}$ vectors independently. The space occupied by $\vec{k}$ wave vectors is known as k space. It is also known as reciprocal space.

2.6 Pseudopotentials

We know that the material bonding properties depend upon the valence electrons not on the core electrons. To solve the Schrodinger wave equation by using the columbic potential from core electrons makes the equation very complicated to solve. To overcome this difficulty an approximation has been made. According to this approximation, the core electrons are treated as an immobile entity stuck to the nucleus. This approximation is given the name as frozen core approximation. Even with this approximation where we remove the core electrons from computation, the numerical calculations that have the contributions of wave function of valance electrons could still be very intensive. The reason behind that is this to be orthogonal to core electrons, the wave function of valance electrons must have nodes in the core region, which leads to the fast oscillations of the wave function in the core region [66]. The core electrons have fast oscillation in the core region and therefore requires many planes wave basis for representation the core electrons orbitals. This requirement is one of the main obstacles in realistic calculations. To overcome this difficulty, it is important to note that the most bonding in solid takes place in the interstitial region as compared to the core region. If we can construct an artificial potential which represents the wave function of the valence electrons in the interstitial region but replace the oscillating part of the wave function by smooth one. We can expect after the construction of this artificial potential, the chemical properties of solids can be described very well. This artificial potential is given the name as pseudopotentials [69]. It has been found that by adoption of the pseudopotential in the realistic solid calculation not only reduced the computational cost but also will describes the chemical behavior of solids. Different

algorithms have been used to design the pseudopotentials for different solid systems, which can be found in the literature [70], [71]. Once the pseudopotential is obtained for any solid system to implement it in Kohn-Sham equation is straightforward. The local ionic potential $V(r)$ in **Equation. (2.13)** is replaced by pseudopotential $V_{ps}(r)$ all other parameters in the equation will be the same.

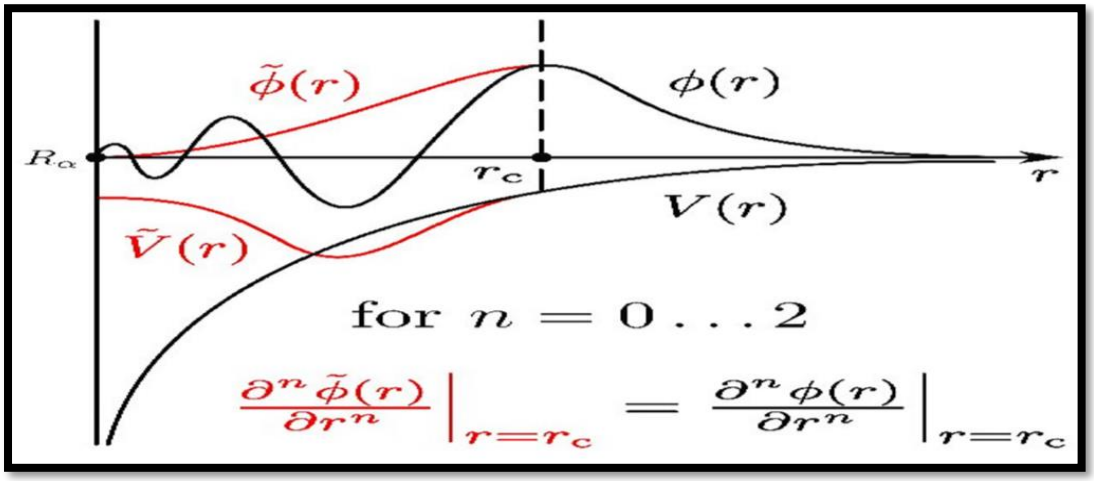

Figure 2-1 comparison between coulomb potential wave function and pseudopotential, inside and outside the core region of an atom. The black line representing the real (also called coulomb potential of all electrons) and the red is for pseudo (valance electron) wave function.

Figure. 2.1 shows comparison between ψ_{pseudo} verses real wave function ψ and pseudo potential V_{pseudo} verses real potential V. The all-electronic wave function and the pseudo wave function match above a certain radii cut-off. Core electrons stay in the core region because they are tightly bound to the nuclei with low Eigen-energies and forming a closed shell. In condensed matter systems core electrons are usually inert and almost irrelevant in determining physical and chemical properties of materials. In contrast, loosely bound valence electrons participate in chemical bonding with other atoms and determine the main characteristic of materials. So, the pseudopotential enables us to achieve fast convergence of our DFT calculations with much lower computational cost.

2.6.1 Norm-conserving pseudopotential

One important class of pseudopotentials is known as norm-conserving pseudopotentials. In 1979, Hamann et al. showed that the pseudo wave function and all

electrons wave function outside the core radius r_c are equal but inside of the core radius r_c it is also a condition that the norm of the pseudo-wave functions and the original wave functions should be equal. Norm conservation means that the charge contained within the chosen radius

r_c is the same for the pseudo wave function and the all-electron wave functions. There are many types of norm-conserving pseudopotentials from different authors such as Hamann Schlüter and Chiang [72], Troullier and Martins [73], Kerker , Vanderbilt [72] and Goedecker-Teter-Hutter [74].

2.6.2 Ultrasoft pseudopotential

The ultrasoft pseudopotential was first introduced by D. Vanderbilt in 1990. The main aim of the ultrasoft pseudopotential is to do the calculations with the reduced possible cutoff energy E_f for the plane-wave basis set. The much softer pseudopotential can be generated by using the relaxation of Norm-Conserving constraint, which is the basic concept of ultrasoft pseudopotential. Because of its better transferability property, the ultrasoft pseudopotential can be used to get the good accuracy. The transferability of pseudopotential means how it works well in different systems. The ultrasoft pseudopotential can work very well not only for a system for which it's designed but for other systems also. It means that this type of pseudopotential shows good transferability behavior as compared to the Norm-Conservative pseudopotential [69]. The example of ultrasoft pseudopotential we used in our theoretical calculations is PBE type pseudopotential [65]. The pseudopotential generated within the Perdew-Burke-Ernzerhof (PBE) framework for density functional theory (DFT) calculations refers to the PBE pseudopotential. To reduce the computational cost and complexity of the calculations, the pseudopotentials are used in DFT. These pseudopotentials are used to replace the core electrons of atoms in a system with an effective potential.

2.7 Computation codes

In this section the details of the computational code that has been used in theoretical work is described.

2.7.1 Quantum ESPRESSO code

Generally, density functional theory calculations are done by using software package Quantum ESPRESSO which stands for OpEn-Source Package for Research in

Electronic Structure, Simulation, and Optimization. It is freely available to researchers worldwide under the terms of the GNU General Public License. The package includes automated calculations and functions such as atomic relaxation and self-consistent calculations (pw.x), post-processing (pp.x), atomic projection (projwfc.x), phonon calculation (ph.x) and Wannier generation (wannier90.x).

Quantum ESPRESSO is an initiative of the DEMOCRITOS National Simulation Centre (Trieste) and SISSA (Trieste), in collaboration with CINECA National Supercomputing centre in Bologna, Massachusetts Institute of Technology, University Pierre et Marie Curie, Princeton University, and Oxford University, Ecole Polytechnique Fdrale de Lausanne. Courses on modern electronic-structure theory with hands-on tutorials on the Quantum ESPRESSO codes are offered on a regular basis in developed as well as in developing countries, in collaboration with the Abdu's Salam International Centre for Theoretical Physics in Trieste.

2.8 Computational study of Ta_3N_5

Computational studies of Ta_3N_5 was done by using the Quantum ESPRESSO code. In this work various aspects of Ta_3N_5 have been studied. The DFT calculations were performed with the plane wave basis pseudopotential method implemented in Quantum Espresso code. The exchange and correlation energy and potential were calculated with GGA and GGA+U [75], [76]. First, we take the orthorhombic unit cell of Ta_3N_5 with space group CmCm. The orthorhombic unit cell of Ta_3N_5 is composed of 32 atoms. In unit cell, the numbers of tantalum atoms are 12 while the nitrogen atoms are 20. The crystal structure optimization has been done by means of DFT by using Quantum Espresso code. The PBE type pseudopotential, which is ultrasoft pseudopotential was used in the crystal structure and in all other types of calculations. Their Brillouin zones were sampled with 10×10×6 Monkhorst–Pack k-point grids. We did the relaxation calculations for the unit cell to fully optimize the cell parameters and ionic coordinates. The residual force criterion applied in this calculation is below 0.001 eV/Å, ensuring a high degree of precision and accuracy. The convergence criterion for Self-Consistent Field (SCF) calculation is $10^{-6}\ eV$. The k-space band structure and electron density of states calculation were performed by DFT and DFT+U by using the Quantum Espresso package. The valence electrons atomic configuration which are used in the calculations are $5d^3 6s^2$ for Ta atom while $2s^2 2p^3$ for N atom respectively. The formation energy (E_f) is defined as,

$$E_f = E_{tot[Ta_{3N_5}-X]} - E_{tot[Ta_{3N_5}]} + \mu_{host} - \mu_x \qquad (2.21)$$

Where, $E_{tot[Ta_{3N_5}-X]}$ is the total energy of defective system including the dopant x. $E_{tot[Ta_{3N_5}]}$ is the total energy of pure Ta_3N_5. The μ_{host} is the chemical potential of the substituted atom while μ_x is the chemical potential of the dopant atom. The more negative the formation energy means much favorable be the doping site. The PBE GGA functional underestimate the band gap energy, to avoid this the PBE functional is corrected by Hubbard parameters (PBE+U) [76] The norm-conserving pseudopotential developed by Fritz Haber Institute (FHI), was used for the optical properties' calculations. The number of valance electrons used in the pseudo-atomic calculations by FHI was 5 for Ta: $[Xe]4f^{14}5d^36s^2$, 5 for N: $[He]2s^22p^3$, and 4 for Mo: $[Kr]4d^55s^1$. The charge density and wave-function cutoff used in the calculations are selected to be 280 Ry and 70 Ry, respectively to lower the computational cost and improve the accuracy. Furthermore, the value for energy convergence was $10^{-6}\ Ry$ and for the force convergence the value was set to $10^{-3}\ \frac{Ry}{\text{Å}}$ [77].

2.9 Experimental procedures

All the experimental procedures are included in this part.

2.9.1 Chemical reagents

The Ta sheet for anodization was purchased from PRO-ANALISE QUIMICA E DIAGNOSTICA LTD, (having purity 99.5%) with dimension $20\ cm \times 20\ cm \times 0.025\ cm$. The sheet was cut into small pieces. The chemicals used for the cleaning of these samples are acetone, methanol, isopropanol and deionized (DI) water. The chemicals used to prepare the electrolyte solution for anodization are HF (38-42%), H_2SO_4 (95-98%) and DI water. These chemicals were purchased from the Modern Chemical Industry and Trade LTD. For Photoelectrochemical (PEC) measurement, KOH (98%) was purchased from Sigma Aldrich. All these chemicals were used as received, without further purification.

2.9.2 Ta sheet anodization

Initially, sheets of tantalum (Ta) were precision-cut into discs measuring 1 cm × 1 cm × 0.025 cm in dimensions. Ta discs were made flat by rubber hammer and were polished to mirror like finishing with different grids of sandpapers; 400, 600, 1200 and 2000

successively. The flat Ta discs were soaked in HF (40%) for 1 min and rinsed with DI water. Ta discs were cleaned in acetone, methanol, isopropanol and DI water successively by sonication for 30 min each. When the ultra-sonication was finished the Ta discs were dried by nitrogen flow. The electrolyte used for anodization was composed of H_2SO_4 + 1 Vol% HF + 4 Vol% H_2O [78]. The anodization was carried out in two cell configuration system. This cell was composed of two Teflon reactors. The anodization was carried out at constant temperature of $10\ °C$ which was kept constant by the water circulating system around it using Thermo Neslab-RTE7 circulating system. However, constant voltage of 50V for 20 min at $10\ °C$ temperature was used to carry out the anodization. The working electrode which consisted of Ta sheet was used as an anode while the polished Cu disc was used as a cathode. Meanwhile, the distance between two electrodes i.e., cathode and anode were kept 1 cm. The electrodes were connected to the DC power supply. During anodization, the current vs voltage curve was monitored by Dalton Vidor software. When the anodization time was finished, the sample was removed from the Teflon reactor and washed several times with DI water to remove the extra residual acid from the sample. The whole setup of anodization which consisted of ultrasound, Teflon cup, Teflon reactors, power supply and digital software are shown in the **Figure. 2.2.**

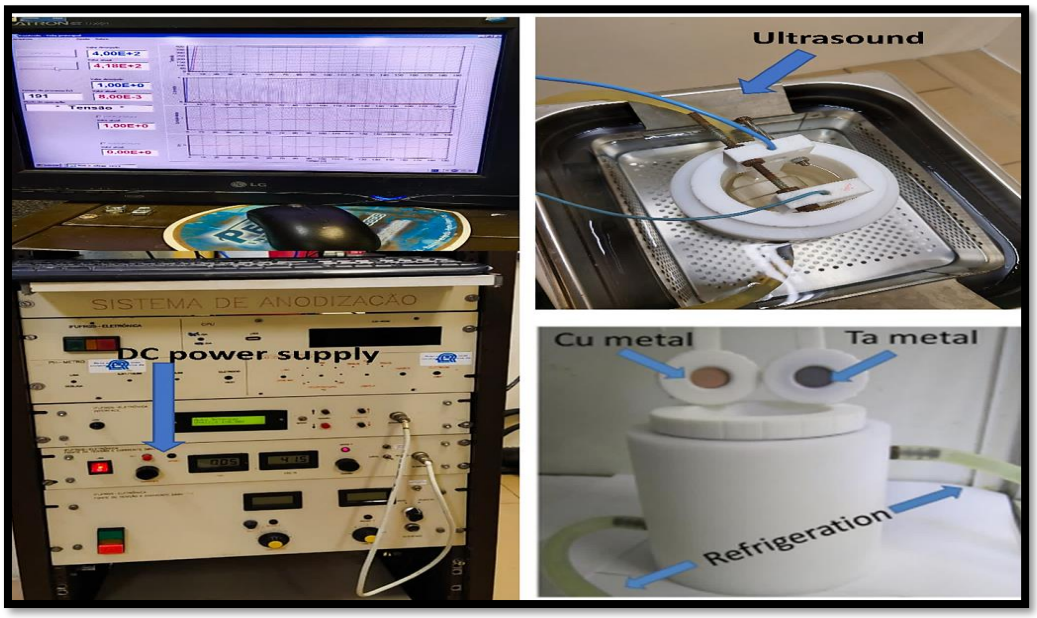

Figure 2-2 Anodization system used for the anodization of Ta sheet.

2.9.3 Doping of foreign metal element in Ta_2O_5

Prior to nitridation we doped foreign metal element Mo in Ta_2O_5 by hydrothermal method. We prepared three different molar solutions of Mo like 0.1M Mo, 0.3M Mo and 0.5M Mo. We put the molar solution in 25mL autoclave reactor in which the anodized Ta discs were suspended. 75% of the total volume of the reactor was occupied by the solution. Furthermore, reactor was sealed and put in the oven for 12 h at $180\ °C$. After 12 h the system was cooled to the room temperature. To dry the samples, they were put in oven again at $80\ °C$ for 6h.

2.9.4 Nitridation of Ta_2O_5

The nitridation process was carried out in a home-made quartz tube furnace. The clean and dried samples were put on aluminum boat and then it was put at the middle of quartz tube furnace. For nitridation we used the argon and ammonia gas mixture. The mixture of gas was composed of 95 Vol% of argon and 5 Vol% of ammonia. Nitridation was carried out at temperature of $900\ °C$ for 3h. For all samples the ramping rate of the furnace in heating and in cooling was $10\ °C\ min^{-1}$ under ammonia flow. The flux of the gas inside the tube was adjusted to $100\ mL\ min^{-1}$ by gass flow meter and this flux was kept constant during the whole period of the experiment. Mixture of gas was allowed to enter the tube on one side and after passing through the tube it was bubbled into the aqueous HCl solution to neutralize the gas. After neutralization, the gas was exhausted to the environment. The samples were cooled to room temperature in the presence of ammonia. After nitridation the samples were rinsed with DI water a few times and dried in an open atmosphere. The nitridation setup we used in our experiments is shown below.

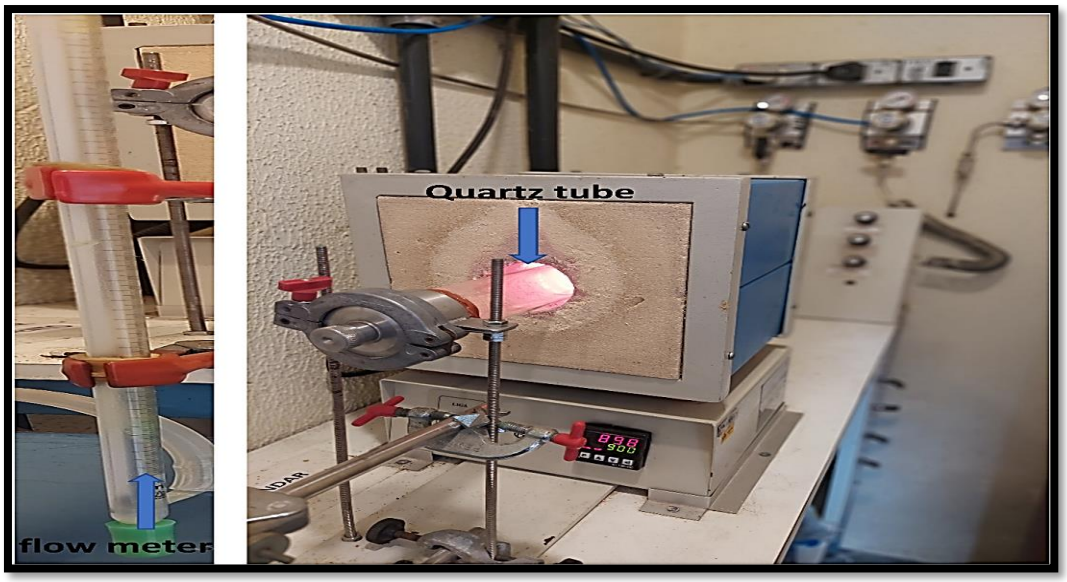

Figure 2-3 Home-made nitridation setup consist of horizontal quartz tube furnace and glas flow meter.

2.9.5 Co-catalyst modification

The surface of bare and doped Ta_3N_5 was modified by co-catalyst. We used the Co $(OH)_x$ as an oxygen evolution co-catalyst to promote the hole transfer. The co-catalyst solution contained 0.1M Co $(NO_3)_2$ and 0.1M NaOH and it was stirred for 1h to get homogeneous solution. The doped and bare Ta_3N_5 was immersed in the solution for 1h and then washed with DI water and dried in air before PEC test. The sample with co-catalyst modification was given the name as Ta_3N_5-Co while with Mo doped Ta_3N_5 samples with the co-catalyst modification were named as MTN-x-Co (x = 0.1,0.3 and 0.5).

2.9.6 Photoelectrochemical measurement of doped Ta_3N_5

We prepared different metals doped Ta_3N_5 on Ta substrate. These samples were named MTN-0.1-Co, MTN-0.3-Co, MTN-0.5-Co and bare Ta_3N_5. The bare sample was prepared in the same way except for soaking it in the molar solution of sodium molybdate dihydrate. The back of these electrodes was polished with sandpaper to make it conductive and cleaned with DI water. After drying, the silver wires were connected with the back of the electrodes by silver colloidal solution. The exposed conductive part of the electrodes was sealed by adhesive epoxy. The PEC performances of bare and doped Ta_3N_5 were measured in three electrodes configuration cell. Ta_3N_5 was used as a working electrode, Ag/AgCl as reference electrode and Pt wire is a counter electrode.

1 mol L^{-1} KOH ($pH = 13.6$) solution was used as a testing electrolyte. The potential of the working electrode was controlled by Gamry Interface 1000 potentiostat. 300 W Xenon lamp was used as a light source. The intensity of light was calibrated to 1 Sun i.e., 100 $mWcm^{-2}$ by using AM 1.5 filter. The calibration of light intensity was done by silicon photodiode with a known responsivity. The measured potential versus Ag/AgCl reference electrode was converted to the reversible hydrogen electrode (RHE) by the following equation.

$$V_{RHE} = V^{0}_{Ag/AgCl} + V_{Ag/AgCl} + 0.0592 \times pH \qquad (2.22)$$

Where $V^{0}_{Ag/AgCl}$ correspond to the standard reference potential of Ag/AgCl electrode at $25\ °C$. $V_{Ag/AgCl}$ is the applied biasing potential in PEC cell applied through potentiostat and pH is the potential of hydrogen of the electrolyte. The linear sweep voltammetry (LSV) curves were obtained at applied biasing voltages of -0.9 to 0.6 with a scan rate of 10 mV/s. The voltage range was found from the above **Equation. (2.22)**.

2.10 Characterization techniques

2.10.1 X-ray diffraction spectroscopy (XRD)

The grazing angle XRD characterizations were performed to investigate the crystal structure of all synthesized samples. The XRD diffractograms were obtained by using the Bruker D8 Advance X-rays diffractometer with Cu K_α radiation ($\lambda = 1.54$Å) at 40 kV and 40 mA. In grazing angle XRD analysis, the grazing angle was 0.3°, at a 2θ range 10° to 70°, with 0.02°, degree step size and measuring time per step was 3 second. The XRD pattern of all samples were obtained by grazing incidence method. The XRD data of all samples were analyzed by using the Origin software.

2.10.2 UV-visible spectroscopy

To determine the bandgap of all samples UV-Vis spectroscopy was performed by using the CARY 5000 spectrophotometer at Centro de Espectroscopia Óptica de Materiais (CEOMat) . We got the reflectance spectra of all samples by diffuse reflectance spectroscopy and the reflectance was converted to Kubelka-Munk function by the following formula,

$$Kubelka - Munk = \frac{K}{S} = \frac{(1-R_\infty)^2}{2R_\infty} \qquad (2.23)$$

Where K and S are the absorption and scattering coefficients respectively while $R_\infty = \frac{R_{sample}}{R_{standard}}$ is the reflectance of infinitely tick sample. The **Equation 2.23** provides the correct definition of the Kubelka-Munk function (F(R) = K/S) [98].

2.10.3 Scanning electron microscopy

To reveal the morphology and surface structure of Ta_2O_5, Ta_3N_5, and Mo-doped Ta_3N_5 nanotubes, scanning electron microscopy (SEM) was conducted using the Zeiss EVO 50 scanning electron microscope, operating at 10 kV. The SEM measurements took place at the Center for Microscopy and Microanalysis (CMM) at UFRGS. Prior to SEM analysis, the samples underwent ultrasonic cleaning using solvents such as isopropanol, methanol, and acetone, followed by drying. Side view images were obtained by scratching the samples. The lengths and widths of Ta_2O_5, Ta_3N_5 and Mo doped Ta_3N_5 nanotubes were estimated using ImageJ software.

2.10.4 Raman spectroscopy

The vibrational and rotational modes of materials are studied by using the Raman spectroscopy analysis. The excitation source used by the Raman spectroscopy is mostly laser light. The choice of the wavelength of laser light mostly depends on the properties of the materials. The wavelengths of laser light that are commonly used are 532 nm, 785 nm and 1064 nm. To achieve the good signal to noise ratio, the laser power should be optimized. The Raman scatter light has useful information about the chemical structure of the sample. In Raman spectroscopy, along y-axis is the intensity of Raman scattering while along x-axis is the frequency. To investigate the chemical fingerprint of our samples the Raman spectroscopy was performed by using HORIBA Confocal Raman Microscope at Centro de Espectroscopia Óptica de Materiais (CEOMat) Institute of Physics UFRGS. The measured data for all samples were analyzed using Origin software.

2.10.5 X-rays photoelectron spectroscopy (XPS)

To investigate the surface compositions and chemical environment of Ta_3N_5 and Mo-doped Ta_3N_5 nanotubes, X-ray photoelectron spectroscopy (XPS) measurements were conducted at Laboratório Multiusuário de Análise de Superfície (LAMAS-UFRGS) using an Al Kα X-ray source (hv = 1486.6 eV, 225W, 15keV, 15mA). Data collection

employed the Omicron SPHERE analyzer, with a pass energy of 50 eV for long scans and a step size of 1 eV for an acquisition time of 0.2s. High-resolution spectra of Ta 4f, Mo 3d, O 1s, and C 1s were obtained using a step size of 0.2 eV and a time per step set to 0.2s. Analysis of the XPS spectra for all samples was performed using CasaXPS software, with correction for charging effects accomplished by referencing to the adventitious carbon component (284.5 eV) in the C 1s region. The Relative Sensitivity Factor (RSF) method was applied to calculate the surface compositions and N/Ta ratios for all samples, as described below

$$\frac{N}{Ta} = \frac{Area\ of\ N\ 1s}{RSF} \div \frac{Area\ of\ ta\ 4f}{RSF}$$

The O/Ta and Mo/Ta ratios were determined using a comparable procedure.

Chapter 3 Enhancement of electronic, optical, and Photocatalytic activity of Mo doped Ta_3N_5 photoanode

Overview

In nitride semiconductors, Ta_3N_5 has emerged as one of the promising photocatalyst for overall water splitting due to its suitable bandgap (experimental value of 2.1 eV and theoretical of 2.0 eV) and band positions [8]. To improve the photocatalytic performance, several morphologies like Nanorods (NRs) [10], Nanoparticles (NPs), and Nanotubes (NTs) [11], [47] have been applied. Among them, Ta_3N_5 NTs having a 1D nature with good charge transport property as well as an active surface area are suitable for PEC applications [11]. The NTs are generally prepared by anodization process and Ta_3N_5 can be prepared by nitridation of Ta_2O_5 NTs. Allam et al. for the first time reported the Ta_2O_5 NTs by using one step anodization in electrolyte containing HF and H_2SO_4 [79]. The anodization of Ta sheet can be carried out Galvano statically or potentiostatically [42].

To control the structural defects generated by the nitridation process and improve the charge transportation, herein the combined theoretical and experimental studies of Pure and Mo doped Ta_3N_5 were performed. The theoretical calculations were performed by using the Quantum Espresso package. In the first step the crystal structure was relaxed to find out the equilibrium lattice constant for pure and Mo doped Ta_3N_5 system. The bandgap energy for pure and Mo doped Ta_3N_5 were calculated and compared with the experiments. Furthermore, the electronic and optical properties of pure and Mo doped Ta_3N_5 were studied by using Density function theory (DFT). In experimental work, a constant voltage anodization was carried out in the electrolyte containing H_2SO_4 + 1 vol% HF and 4 vol% H_2O [80]. Different molar solutions of sodium molybdate as a source of Mo for doping in Ta_2O_5 were prepared. For doping, the hydrothermal method was followed. Afterwards the thermal nitridation of doped Ta_2O_5 was carried out to obtain the Mo doped Ta_3N_5 NTs. For bare Ta_3N_5 NTs, the nitridation condition was the same. The samples were characterized comprehensively.

3.1 DFT study of pristine and Mo-doped Ta_3N_5

3.1.1 DFT-GGA calculations

The conventional unit cell of Ta_3N_5 has an orthorhombic crystal structure, with 32 atoms per unit cell (**Figure 3.1**). The number of Ta atoms per unit cell is 12 while N is 20 and the unit cell is characterized by lattice parameters a, b/a ratio, c/a ratio and mutual angles α, β, and γ. In the crystal structure of Ta_3N_5, each Ta atom is coordinated with five N atoms while each N atom has three or four Ta nearest neighbors. The Ta─N bond length along x, y and z directions are 2.95 Å, 1.97 Å and 2.04 Å, respectively. The Ta─Ta bond length is 2.95 Å. All these bond lengths are calculated after relaxing the crystal structure. The Mo is doped at Ta site where the x-coordinate was maximum (**Figure 3.2**). The choice of this site corresponds to more negative formation energy that results in the highest stability. Compared to pure Ta_3N_5, the Ta (Mo) ─N bond length along x, y and z directions decreased to 2.03 Å, 1.86 Å and 2.01 Å, respectively and Ta (Mo) ─Ta bond length slightly increased to 2.97 Å. These changes are attributed to the electronegativity difference between Ta (1.5) and Mo (2.16). After doping, the crystal structure was relaxed, and the lattice constants are compared in **Figure 3.2 (a)** and **Figure 3.2 (b)** showing that the very small change in the lattice constants was observed after Mo doping (**Table 3.1**). All of the theoretically calculated lattice parameters show good agreement with previous literature (**Table 3.1**).

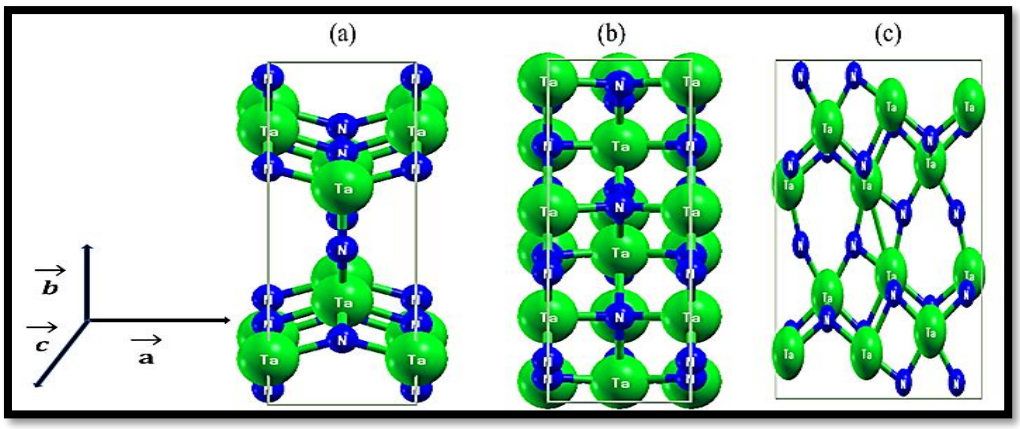

Figure 3-1 Crystal structure of pristine Ta_3N_5. (a) Top view of unit cell (b) side view and (c) bottom view.

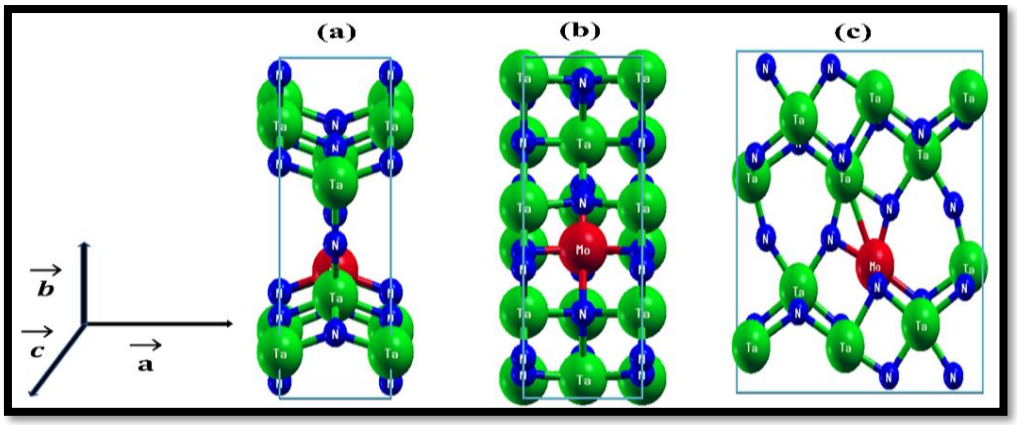

Figure 3-2 Theoretical model of Mo- doped Ta_3N_5. (a) Top view of Mo doped Ta_3N_5 unit cell (b) side view and (c) bottom view.

Due to the lower U value and the approximate similarity in ionic radii of Ta (64 Å) and Mo (65 Å), a small change in the lattice constant is observed [24], as depicted in **Figure 3.3 (A), 3.3 (B)** and **Table 3.1**.

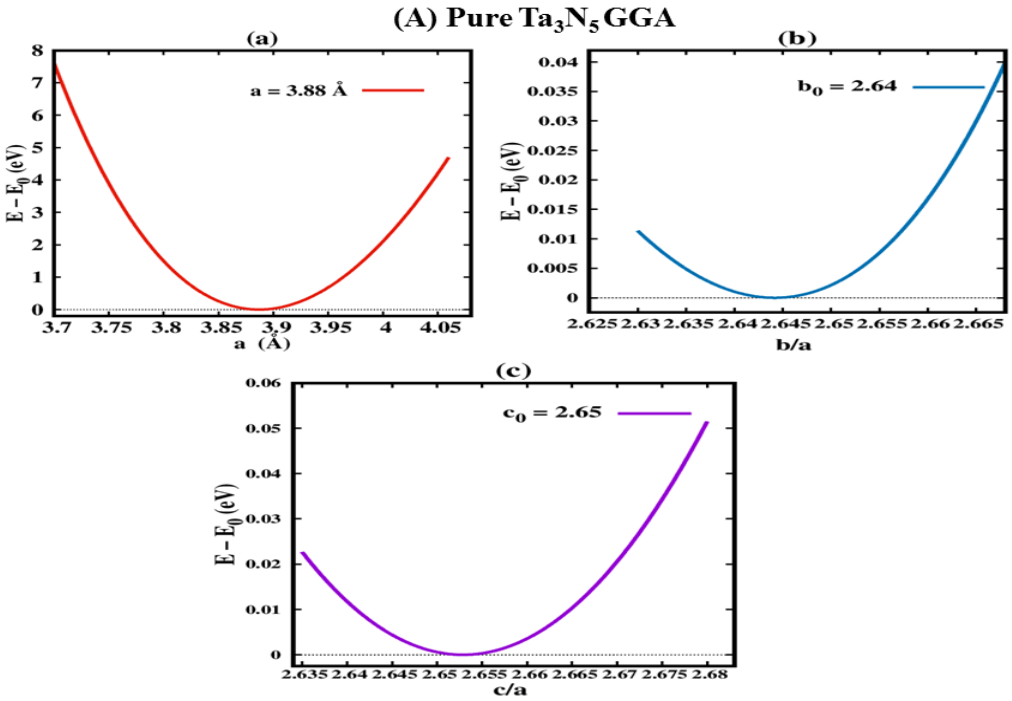

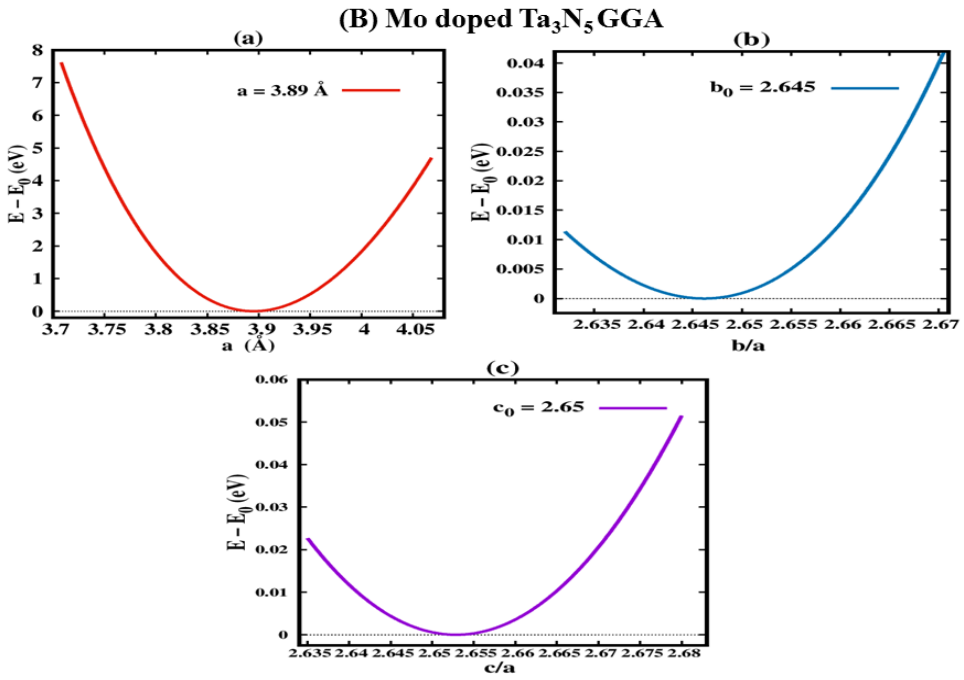

Figure 3-3 (A) (a) Theoretical lattice constant a (b) b/a ratio and (c) represent the c/a ratio of pure Ta_3N_5 unit cell. (B) (a) Lattice constant a, (b) b/a ratio and (c) C/a ratio of Mo doped Ta_3N_5.

Table 3-1 Lattice parameters of pure and Mo doped Ta_3N_5 calculated with GGA and GGA+U methods.

Lattice parameters	This work Pure Ta_3N_5		This work (Mo doped Ta_3N_5)		Previous work (Pure Ta_3N_5)	Ref
	GGA	GGA+U	GGA	GGA+U		
a (Å)	3.88	3.88	3.89	3.89	3.89	[81]
b (Å)	10.26	10.27	10.27	10.28	10.26	[82]
c (Å)	10.30	10.31	10.31	10.31	10.31	[83],[77]
α (°)	90.0	90.0	90.0	90.0	90.0	[84]
β (°)	90.0	90.0	90.0	90.0	90.0	[41]
γ (°)	90.0	90.0	90.0	90.0	90.0	[41],[77]

The first principle calculated band gap energy of pristine and Mo-doped Ta_3N_5 are shown in **Figure. 3.4** and **Figure 3.5**, respectively based on GGA calculation. The calculated bandgap energy for pristine Ta_3N_5 is 1.39 eV.

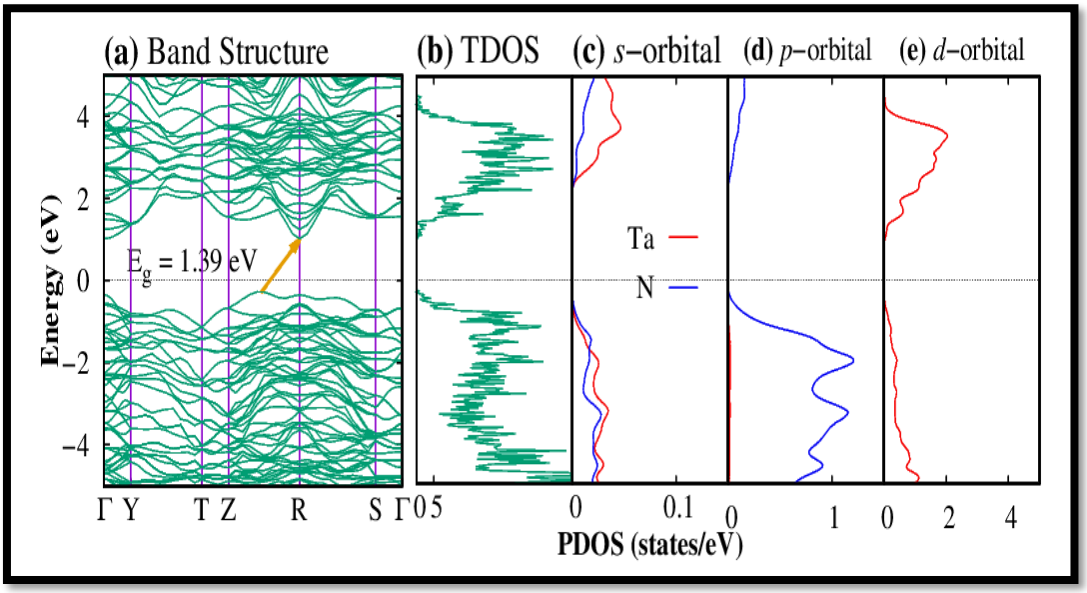

Figure 3-4 Band structure, TDOS and PDOS of pure Ta_3N_5 calculated with GGA approximation.

From the band structure diagram, it can be inferred that pure Ta_3N_5 exhibits indirect bandgap because the top of the VB or valance band maximum (VBM) and conduction band minimum (CBM) lies at the different k-point of the Brillouin zone (BZ) [41]. However, it is published in the previous literature that Ta_3N_5 is an indirect band semiconductor with bandgap energy of 2.1, while in some cases it is direct bandgap semiconductor [55]. The inconsistency between these results is related to GGA which always underestimates the bandgap energy. Based on total density of states (TDOS) and partial density of states (PDOS) (**Figure 3.4**), the VB of pure Ta_3N_5 is mostly composed of N 2p orbitals, while the CB is mainly composed of Ta 5d orbitals. However, the Ta 5d states have some non-vanishing values in VB of Ta_3N_5 which indicates the bond between Ta and N atoms is strongly covalent. We calculated the formation energy for the doped system, and it was -9.10 eV/unit cell. This formation energy shows Mo-doped Ta_3N_5 is thermodynamically stable.

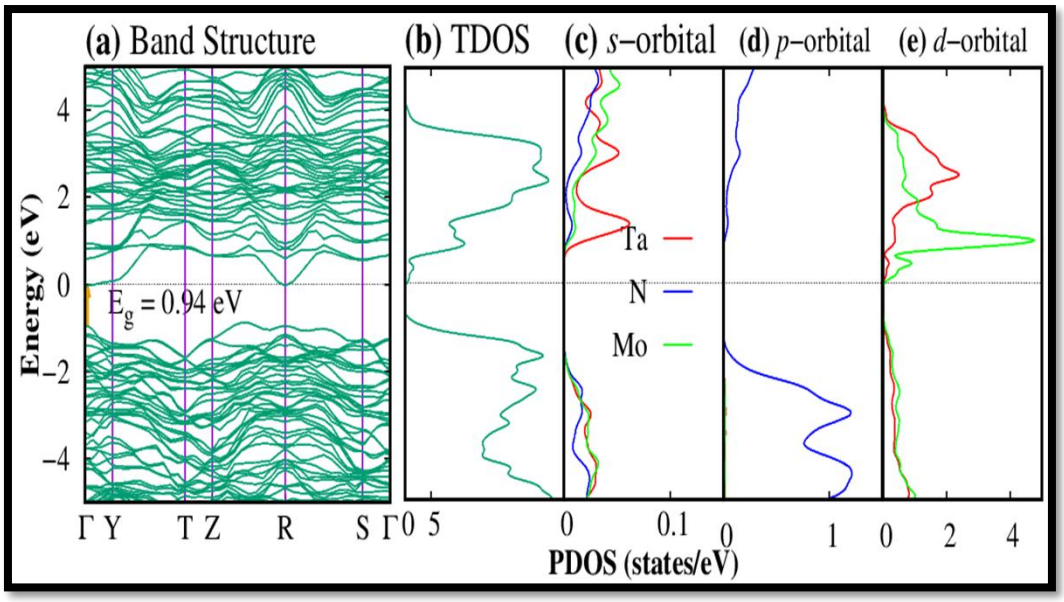

Figure 3-5 Band structure, TDOS and PDOS of Mo-doped Ta_3N_5, calculated with GGA approximation.

After thermodynamic stability, we performed the electronic bandgap calculations for Mo doped Ta_3N_5 (**Figure. 3.5**). Mo-doped Ta_3N_5 has a direct bandgap of 0.94 eV calculated with GGA. The VB of Mo-doped Ta_3N_5 is mainly composed of N 2p orbitals hybridized with the Mo 4d and Ta 5d orbitals. The N 2p orbitals are more dominant throughout the VB. The CB is mainly composed of Ta 5d and Mo 4d orbitals. Because of the dominant contribution of Mo 4d states in the CB and also non-vanishing values of Mo in all PDOS in the VB (**Figure 3.5**), the bandgap is decreased in case of Mo doping. Similar bandgap engineering was achieved in previous literature by doping V atom in Ta_3N_5 [96]. The bandgap value obtained by H. Jouypazadeh et al by doping V atom in Ta_3N_5 was 1.06 eV. In addition to decrease in the bandgap energy Mo doping in Ta_3N_5 shows a formation of an additional density of states in the CB as indicated by the PDOS (**Figure. 3.5**) that improves its n-type conductivity; indicating a great promise to use Mo-doped Ta_3N_5 in solar energy harvesting.

Above results show a mismatch between theoretical and experimental values of the bandgap energy caused by GGA approximation. The underestimation is due to the strong hybridization between d and p-states electrons. Thus, a strong p-d coupling changes the bandgap to a smaller value as compared to the experimental results. Different bandgap values were calculated in the literature by using different computational codes based on DFT as shown in the **Table. 3.3** Which indicates a

diversity in the values of the bandgap energy calculated by GGA. Therefore, concerted efforts must be made to effectively address and overcome these inconsistencies

Table 3-2 The calculated band gap energy of pristine and Mo-doped Ta_3N_5.

Sample	Computer code	Method	Band gap (eV)	Ref
Ta_3N_5	Quantum Espresso (QE)	GGA-PBE	1.39	Present work
Ta_3N_5	WIEN2K	GGA-PBE	1.1	[29]
Ta_3N_5	VASP	GGA-PBE	1.2	[29]
Ta_3N_5	VASP	GGA-PBE	1.4	[29]
Ta_3N_5	Experiment	UV-vis spectroscopy	2.1	[84]
Mo- Ta_3N_5	QE	GGA-PBE	0.96	Present work
V- Ta_3N_5 (sheet)	QE	GGA-PBE	1.06	[77]

3.1.2 Determination of Hubbard parameters U

In the literature, to overcome the shortcoming of GGA, different methods are available such as PBEO, HSE and GGA+U to simulate the bandgap of the semiconductors close to their experimental value. Using the hybrid functional like PBEO or HSE for band structure calculations is time consuming and it also overestimates the bandgap energies [85]. Compared to these functional, GGA+U has proven to be a highly effective method [86]. In GGA+U method, a one site coulomb energy is added to the chosen orbitals. Due to the addition of this columbic energy, the upshift in CB is observed while the energies of the occupied orbitals i.e., VB remain the same as compared to GGA. Because of the upshift of the CB band, the bandgap increases [87]. The main significance of adding the one site coulomb interaction to the selected orbitals is to correctly describe the electronic structures of pure and Mo doped Ta_3N_5. The addition of a precise U value to the DFT calculations provides a better understanding of the system and the obtained results that match well with the experimental results [83]. To overcome these difficulties, the GGA method was corrected with the Hubbard coulomb interaction parameters [85]. The Hubbard parameter U can be defined as

$$U = uU_{ion} \quad (3.1)$$

Where, u is constant (0 < u < 1) whose values are estimated by comparing the calculated bandgap value with the experimental bandgap value for a given system [96],[105]. The U_{ion} values for Ta^{5+}, N^{3-} and Mo^{4+} are given in **Table. 3.3.**

Table 3-3 The calculated values for $Ta^{5+,}$ N^{3-} and $M^{4+.}$

Ion	U_{ion}	Ref
Ta^{5+}	14.05	[83]
N^{3-}	9.33	[83]
M^{4+}	6.45	[88]

The choice of U value is critical to calculate the exact geometry and band structures as compared to experimental values. Some previous work also shows that high U values exaggerates the band gap energy as compared to experimental values. For this reason, we keep the U value very low in our calculation [112]. We calculated the band gap energy and lattice parameter for two different values of U. The U value for all three elements Ta, N and Mo are given in the **Table. 3. 4**.

Table 3-4 Hubbard parameter values for Ta, N and Mo that are used in our DFT calculations.

u	$U (eV) = uU_{ion}$		
	Ta	N	Mo
0.1	1.41	0.93	0.65
0.2	2.82	1.86	1.29

The band structure, TDOS and PDOS of pure Ta_3N_5 calculated from GGA+U is shown in **Figure. 3.6** and **Figure. 3.7**. The bandgap energy calculated with GGA+U approximation (with u = 0.1 and 0.2) showing that pure Ta_3N_5 is an indirect bandgap semiconductor as the CBM and VBM are located at R and Γ point of the Brillouin zone. This result matches well with the experimental results where pure Ta_3N_5 is an indirect bandgap semiconductor [53]. The increase in the bandgap energy value as compared to GGA is due to the change in potential profile of the unit cell caused by the U. The calculated indirect bandgap energies with GGA+U were 1.87 eV (u =0.1) and 1.98 eV

(u =0.2). In line with GGA, the VB of pure Ta_3N_5 is mostly composed of N 2p orbitals while the CB is dominated by Ta 5d orbitals. The increase in the bandgap energy with increasing u agrees with the previously reported work, where H. Julazadeh et al observed a similar trend [77] related to the Coulomb interaction which is kept among the localized orbitals' electrons (d and f states). In the bandgap, these localized orbitals are close to the fermi energy and the higher U value pushes away these states from the fermi energy [95].

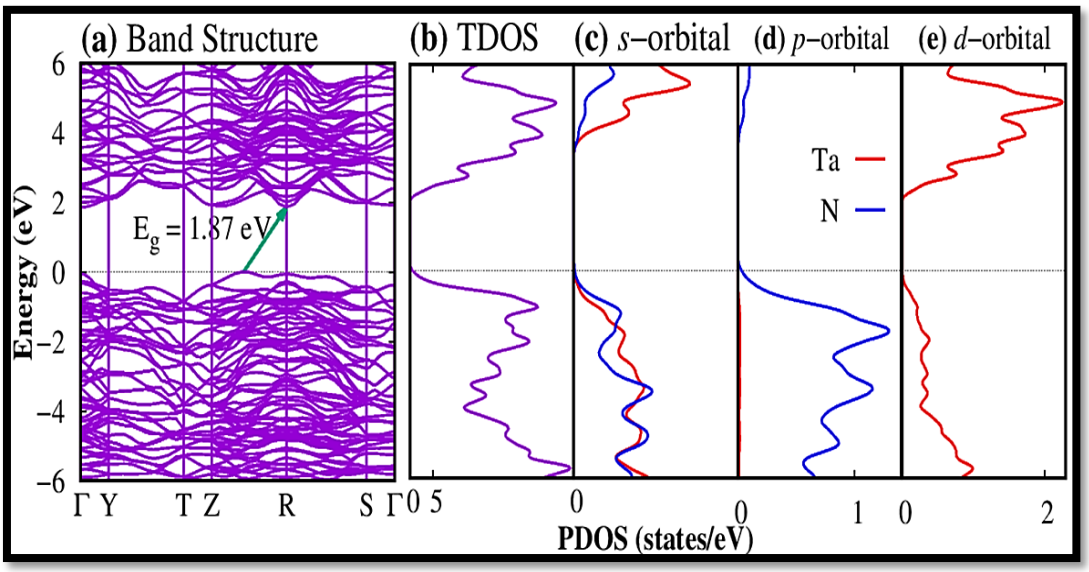

Figure 3-6 Band structure, TDOS and PDOS bare Ta_3N_5, calculated with GGA+U approximation (u = 0.1).

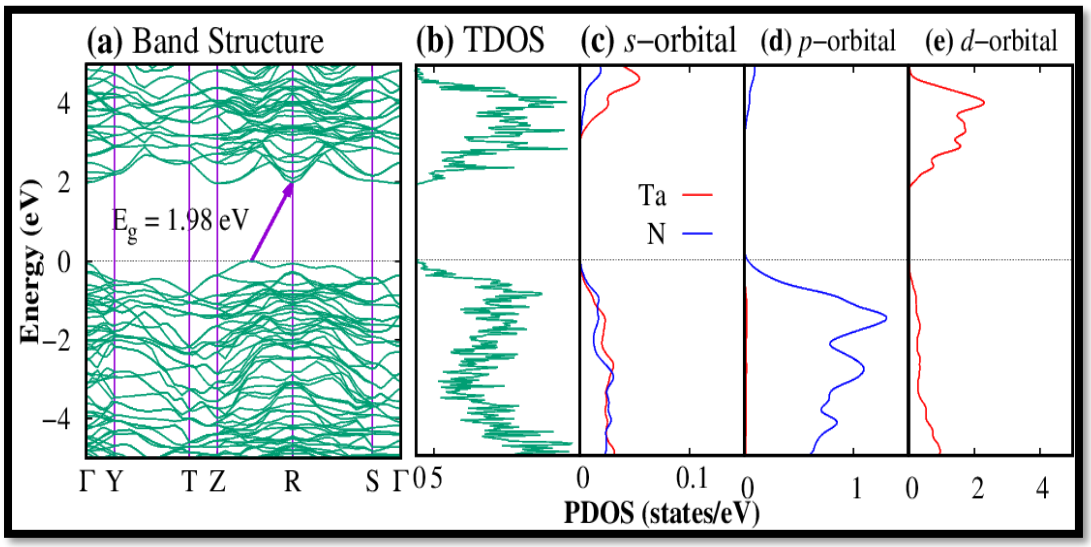

Figure 3-7 Band structure, TDOS and PDOS bare Ta_3N_5, calculated with GGA+U approximation (u = 0.2)

Figure 3.8 and **3.9** show the band structure, TDOS and PDOS of Mo doped Ta_3N_5 calculated with GGA+U approximations for u = 0.1 and 0.2. The formation energy Mo doped Ta_3N_5 increased as compared to pure Ta_3N_5 (**Table 3.5)** indicating that the replacement of Ta atom with Mo atom decreases the stability of Ta_3N_5. As compared to pure Ta_3N_5, the bandgap energy of Mo doped Ta_3N_5 decreased to 1.06 eV (u = 0.1) and 1.16 eV (u = 0.2).

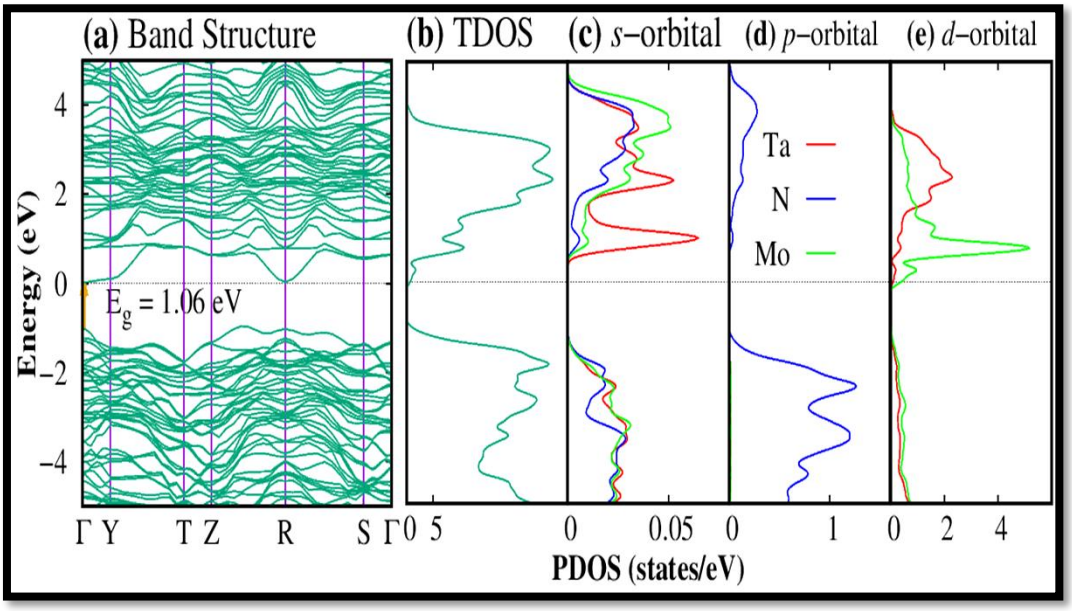

Figure 3-8.Band structure, TDOS and PDOS of Mo-doped Ta_3N_5, calculated with GGA+U approximation (u = 0.1).

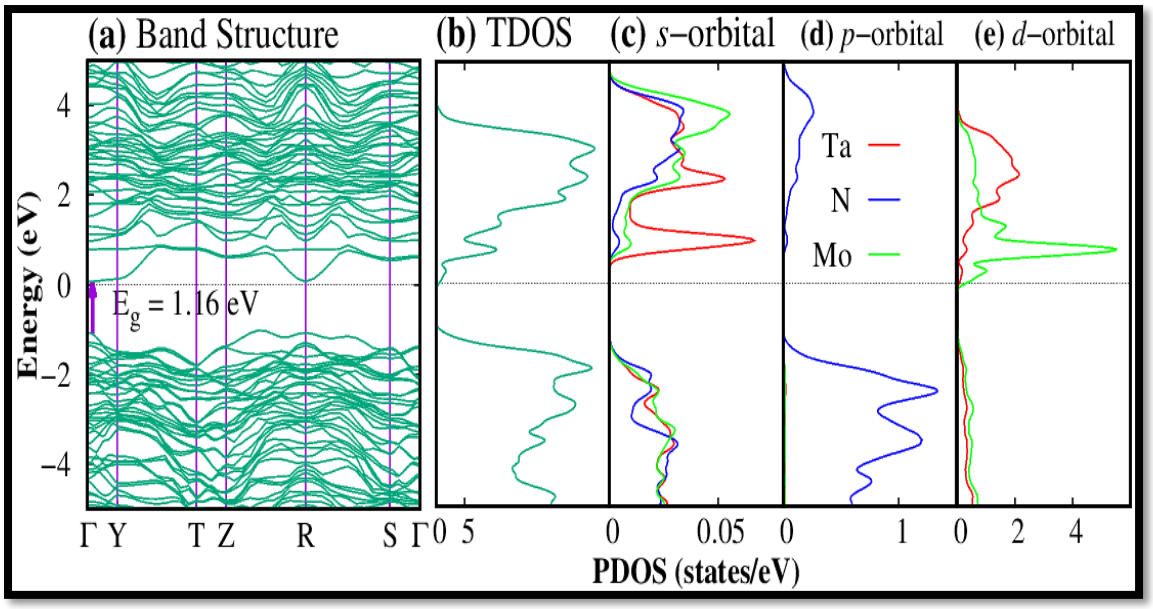

Figure 3-9 Band structure, TDOS and PDOS of Mo-doped Ta_3N_5, calculated with GGA+U approximation (u = 0.2).

This significant change in the bandgap energy of Mo doped Ta_3N_5 can be attributed to the presence of unoccupied 4d orbital of Mo. This unoccupied 4d orbital of Mo creates some extra states due to which the conduction band is shifted down as shown in **Figure 3.8** and **3.9**. Similar to pure Ta_3N_5, the VB of Mo doped Ta_3N_5 is mostly composed of N 2p orbitals while the CB is dominated by Ta 5d and Mo 4d orbitals. Interestingly, the nature of the bandgap calculated with GGA+U changes from indirect bandgap to direct bandgap semiconductor with Mo doping i.e., VBM and CBM lay at the same symmetry point Γ of the BZ. Thus, in addition to decreasing the bandgap energy, the nature of the bandgap can also be changed from indirect to direct by doping Mo in Ta_3N_5. [89]. The main drawback of the indirect bandgap semiconductor is its low efficiency in light absorption and emission as compared to the direct bandgap semiconductor. It is because the electronic transition for indirect bandgap semiconductors requires three simultaneous interactions that involve a photon, an electron and a phonon. Due to multiple particles interaction in the process, the electronic transition from VB to CB occurs at lower rate, thus absorption length decreases. In contrast, for direct bandgap semiconductors, there is no involvement of phonon due to which the light absorption and the electron excitation from VB to CB band is much higher. Direct bandgap semiconductors can be utilized in light emitting diodes, solar cells, photodetectors and

PEC water splitting [90]. Moreover, VB of Ta_3N_5 remained unchanged as it is mainly composed of N 2*p* orbitals with negligible contribution of the *p* orbitals of Mo and Ta, while the unoccupied 4d orbitals of Mo play a significant role in contributing to the CB of Mo-doped Ta_3N_5. The CB of Mo doped system is dominated by the unoccupied Mo 4d and Ta 5d orbitals. PDOS plots also show that the intensity of Mo 4d orbitals is very high in the CB as compared to the Ta 5d orbitals that pulls the CB toward VB and hence a decrease of bandgap is observed.

Table 3-5 The calculated bandgap and lattice constants of pure and Mo-doped Ta_3N_5 calculated with GGA+U.

u	Lattice constant (a, b, c)Å	Sample	Band gap	E_{form} (eV/Unit cell)
0.1	3.88, 10.27, 10.31	Ta_3N_5	1.87	-9.90
0.1	3.89, 10.28, 10.31	Mo- Ta_3N_5	1.06	-8.96
0.2	3.88, 10.27, 10.31	Ta_3N_5	1.98	-9.30
0.2	3.89, 10.28, 1.31	Mo- Ta_3N_5	1.16	-8.86

3.2 Optical Properties

The interaction between electromagnetic radiation and materials gives rise to a range of observable phenomena, owing to the intriguing interplay light matter interaction [91] . To gain a comprehensive understanding of the optical properties of a material, the dielectric constant stands out as a pivotal parameter. It plays an important role in many processes, especially in the case of light matter interaction i.e., the material response to electromagnetic radiation. The dielectric constant ε(ω) can be divided into its real and imaginary parts by the following relation [92],

$$`\varepsilon(\omega) = \varepsilon_1(\omega) + \iota\varepsilon_2(\omega) \quad (3.2)$$

In the above **Equation 3.2**, $\varepsilon_1(\omega)$ and $\varepsilon_2(\omega)$ represent the real and imaginary part of dielectric constant. The imaginary part of the dielectric constant gives the information about the total energy absorbed by the material. Random phase approximation can be used to calculate the $\varepsilon_2(\omega)$;

$$\varepsilon_2(\omega) = \frac{4\pi e^2}{m^2\omega^2}\sum_{i,j}\int\langle i|M|j\rangle^2 f_i\,(1-f_i)\times\delta(E_{j.k}-E_{i.k}-\omega)d^3k \quad (3.3)$$

Where i and j represent the initial and final states, M is the dipole matrix element while E_i and f_i represent the energy level of electron and Fermi-Dirac distribution function of the (i^{th}) state. The real part of the dielectric function can be calculated from the imaginary part of dielectric function by using the Kramers-Kronig relation [93], [94] such as;

$$\varepsilon_1(\omega) = 1 + \frac{2}{\pi}\,C\int_0^{\infty}\frac{(\omega'\varepsilon_2(\omega')}{(\omega'^2-\omega^2)}d\omega' \quad (3.4)$$

In **Equation 3.4** 'C' represents the Cauchy principal value. The imaginary and real part of dielectric function can be used to calculate the other optical properties of material. The refractive index which is the linear combination of refractive index (real part) and extinction coefficient [95] (imaginary part) as given below.

$$\bar{n}(\omega) = n(\omega) + \iota K(\omega) \quad (3.5)$$

The refractive index n(ω) [96] and extinction k(ω) are represented as follows,

$$n(\omega) = \frac{1}{\sqrt{2}}\left[\sqrt{\varepsilon_1^2(\omega)+\varepsilon_2^2(\omega)} + \varepsilon_1(\omega)\right]^{\frac{1}{2}} \quad (3.6)$$

And

$$k(\omega) = \frac{1}{\sqrt{2}}\left[\sqrt{\varepsilon_1^2(\omega)+\varepsilon_2^2(\omega)} - \varepsilon_1(\omega)\right]^{\frac{1}{2}} \quad (3.7)$$

Similarly, the reflectivity which is represented by R (ω) [97] are given in term of extinction coefficient and refractive index as shown below,

$$R(\omega) = \frac{(1-n)^2+k^2}{(1+n)^2+k^2} \quad (3.8)$$

Furthermore, the electron energy loss (EEL), L (ω) [96] is represented by the following relation,

$$L(\omega) = \frac{\varepsilon_2(\omega)}{\varepsilon_1^2(\omega)+\varepsilon_2^2(\omega)} \quad (3.9)$$

The imaginary part of dielectric function can be split into three tensor components $e^{xx}(\omega)$, $e^{yy}(\omega)$ and $e^{zz}(\omega)$. The average of all these three tensor components was taken

in calculating the optical properties. All the optical properties are calculated by using the GGA and GGA+U approximation (u = 0.2). The choice of u value is based on the maximum bandgap that we obtained for both pristine and Mo doped Ta_3N_5 (**Table 3.5**).

The GGA and GGA+U calculated imaginary part of pristine and Mo doped Ta_3N_5 as a function of energy of photon are shown in **Figures 3.10 (a)** and **(b)**. The information about the absorption behavior of a material and its optical bandgap can be extracted from the imaginary part of dielectric function ($\varepsilon_2(\omega)$) [98]. The imaginary part of the dielectric function $\varepsilon_2(\omega)$ increases suddenly after approaching the value of the bandgap followed by a maximum value with increasing photon energy (**Figure 3.10a and 3.10b**). Both GGA and GGA+U calculations yielded an optical bandgap that matches the electronic bandgap (**Table 3.5**). By GGA, the maximum of $\varepsilon_2(\omega)$ was located at ~2.0 eV and ~1 eV for pure and Mo doped Ta_3N_5, respectively. On the other hand, after U correction, these transitions were observed at 1.47 eV and 2.50 eV, respectively. These excitations are related to the electronic transitions from N 2p states to Ta 5d states (pure) and Ta5d + Mo4d (doped). Our results align with the findings of A. H. Reshak et al, who similarly observed a maximum in the imaginary part of the dielectric functions at approximately 2.9 eV and 2.6 eV. Similarly, the imaginary part of dielectric function calculated through GGA+U functional of pristine and Mo doped Ta_3N_5 as a function of energy of photon as shown in **Figure. 3.10 (b)**. The threshold energies of pure and Mo doped Ta_3N_5 are compared with the electronic bandgap value **(see Table 3.5)**. After comparison, it is concluded that the electronic and optical bands gap of pure and doped samples matched very well. The maximum of imaginary part of dielectric function peak lies at 2.50 eV for pure Ta_3N_5 as shown by red dotted line while for Mo doped Ta_3N_5 is at 1.47 eV as shown by blue dotted line in **Figure 3.10 (b)**. This is a clear indication that the absorption is shifted toward lower energy in case of Mo doped Ta_3N_5, and hence the absorption of photon is enhanced with Mo doping. These results matched with the previous reported work by A. H. Reshak et al and [99] whose observed the maximum of imaginary part of dielectric function at around 2.9 eV and 2.6 eV respectively. The observed two cleared absorption peaks below 3 eV, is shown in **Figures. 3.10 (a)** and **Figure. 3.10 (b).** In addition to these peaks, the appearance of the other peaks at higher photon energy shows that Ta_3N_5 is optically anisotropic [53].

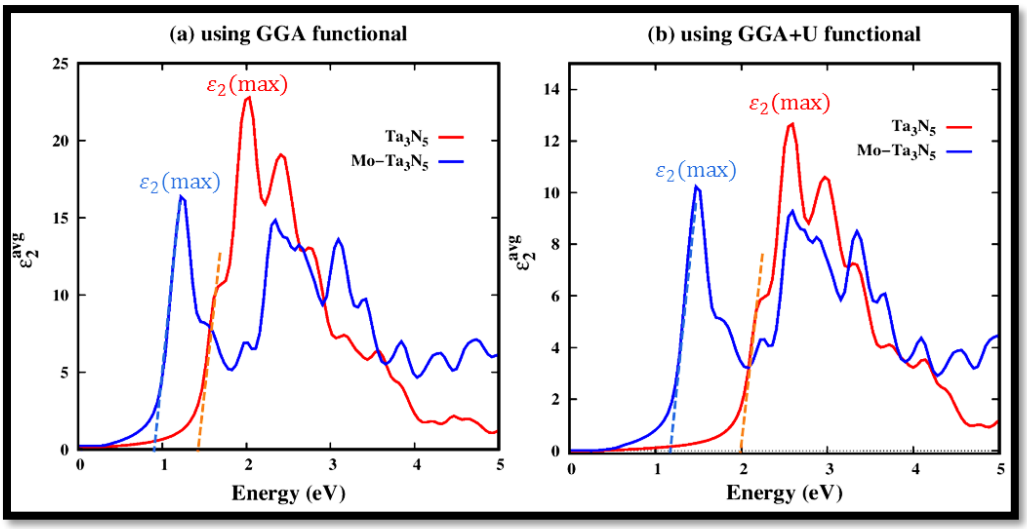

Figure 3-10 The GGA and GGA+U calculated optical spectra of pristine and Mo doped Ta_3N_5 (a) the imaginary part of dielectric function using GGA approximation and (b) imaginary part of dielectric function using GGA+U functional (u = 0.2). The dotted lines represents the optical bandgap.

Figure 3.11 shows the GGA and GGA+U calculated absorption spectra of pure and Mo doped Ta_3N_5. The optical bandgaps are listed in **Table. 3.6**.

Table 3-6 Optical bandgap of pure and Mo doped Ta3N5 calculated from absorption spectra.

Simple	Optical bandgap with GGA	Optical bandgap with GGA+U	$\varepsilon_1^{Average}(0)$ With GGA	$\varepsilon_1^{Average}(0)$ With GGA+U
Ta_3N_5	1.40 eV	2 eV	8.9	6
Mo- Ta_3N_5	0.98 eV	1.20 eV	11.58	8.31

The decrease in the optical bandgap of Mo doped Ta_3N_5 is related to the presence of unoccupied 4d orbital of Mo, as shown in all-band structure diagrams (**Figures 3.8, 3.9**). The absorption spectrum increases up to 30% at low energy range with Mo doping which is slightly higher than pure Ta_3N_5 that is consistent with the spectra of the imaginary part of dielectric function (**Figure 3.10**). For the electronic band structure calculations, the GGA+U functional resulted in more accurate results as compared to

GGA (**Figure 3.7** and **Figure 3.4**). The optical properties obtained by GGA+U functional exhibited a similar trend.

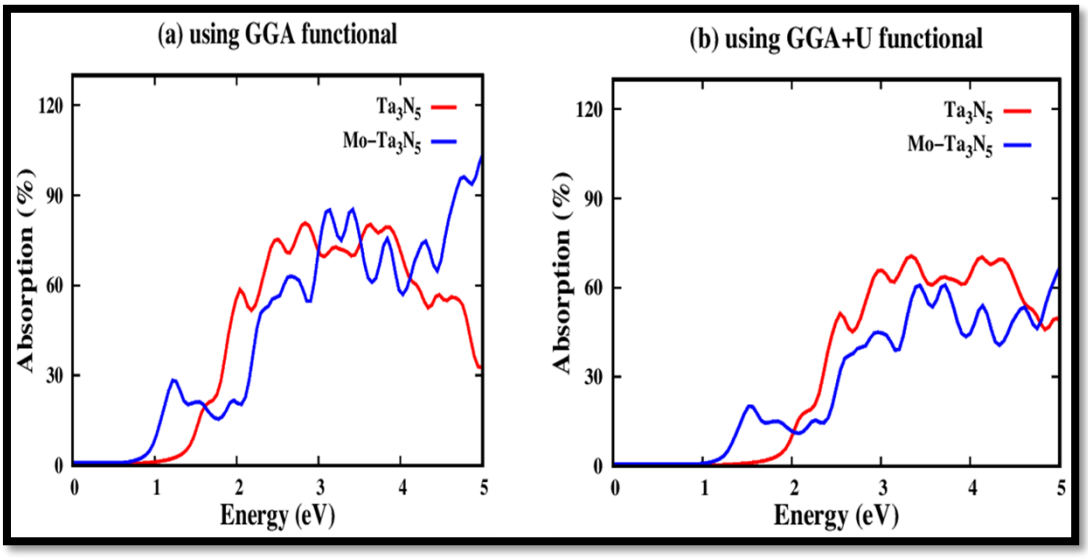

Figure 3-11 The GGA and GGA+U calculated absorption spectra of pristine and Mo doped Ta_3N_5 (a) the absorption spectra by using GGA approximation and (b) absorption spectra using GGA+U (u = 0.2).

Figure 3.12 (a) and **(b)** compare the real part of dielectric function of pure and Mo doped Ta_3N_5 versus the energy of photon calculated through GGA and GGA+U functional. The real part of dielectric function provides information about how much the material is polarized with the applied electromagnetic radiation. By using the real part, we can calculate the static dielectric constant which corresponds to zero frequency ($\omega \rightarrow 0$). The values of static dielectric constant are listed in **Table 3.6**. These values show that smaller dielectric constants yield a larger energy gap [41]. This statement could be explained with the help of Penn model [100], [101]. The Penn model is given below.

$$\varepsilon(0) = 1 + \left(\frac{\hbar\omega_p}{E_g}\right)^2 \qquad (3.10)$$

Where, E_g is the average energy gap.

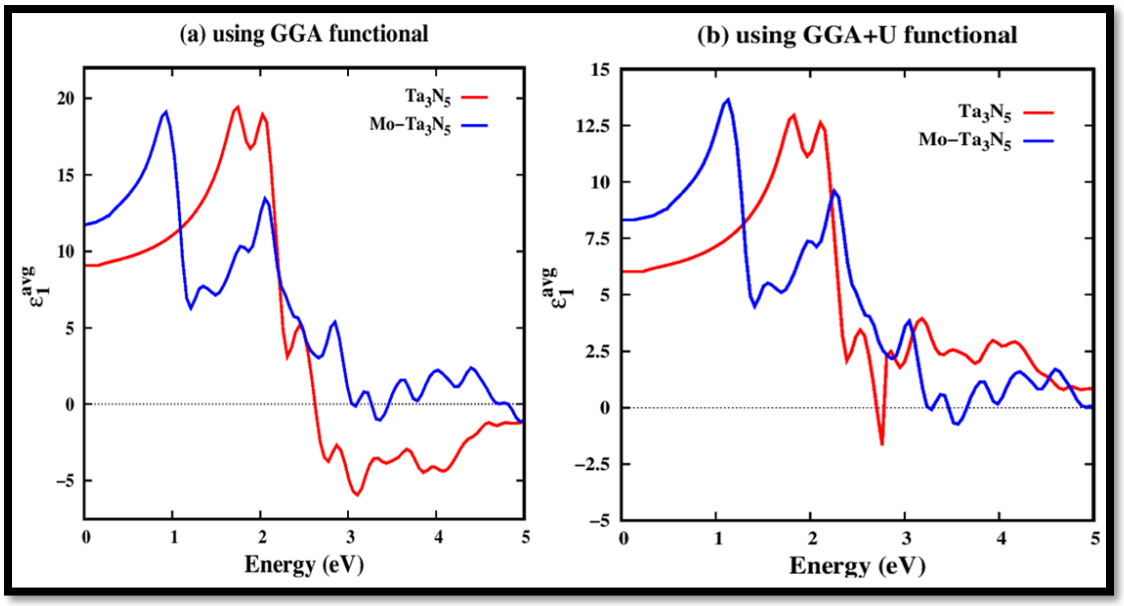

Figure 3-12 real part of dielectric function of pure and Mo doped Ta_3N_5 versus energy (u = 0.2).

For GGA and GGA+U, we clearly observed the inverse relation between ε (0) and E_g. Hence a larger ε (0) yields a smaller E_g as shown in **Figure 3.12**. The real part of dielectric constant for pure Ta_3N_5 calculated with GGA+U in the present work matched very well with the previous literature [89]. For Mo doped Ta_3N_5, we cannot find any related work in the previous literature, but our electronic and optical bandgap matched very well. This matching supports the present work that Mo is one of the best candidates for Ta_3N_5 to change its absorption and nature of the bandgap. Different polarization peaks in **Figure 3.12** show high anisotropy of pure and Mo doped Ta_3N_5. In the energy range for GGA based calculation (**Figure 3.12a**) where the real part of the dielectric constant is negative indicates that at that energy the material shows metallic behavior which is contrary to the experimental behavior [102]. Our GGA+U calculations confirmed that the metallic behavior is almost negligible.

Figure 3.13 (a) and **(b)** shows the GGA and GGA+U calculated reflectivity of pure and Mo doped Ta_3N_5 versus the energy of photon. The zero-frequency reflectivity of pure and Mo doped Ta_3N_5 calculated with GGA approximation are 27% and 21%, respectively. Similarly, the maximum reflectivity calculated with GGA for pure Ta_3N_5 is 60% at 4 eV while in case of Mo doped Ta_3N_5 it is 37% at 1.02 eV. These values are very high as compared to previous literature because of the GGA approximation which

overestimates the optical properties. The GGA+U calculated zero frequency reflectivity values for pure and Mo doped Ta_3N_5 are 21% and 16%, respectively.

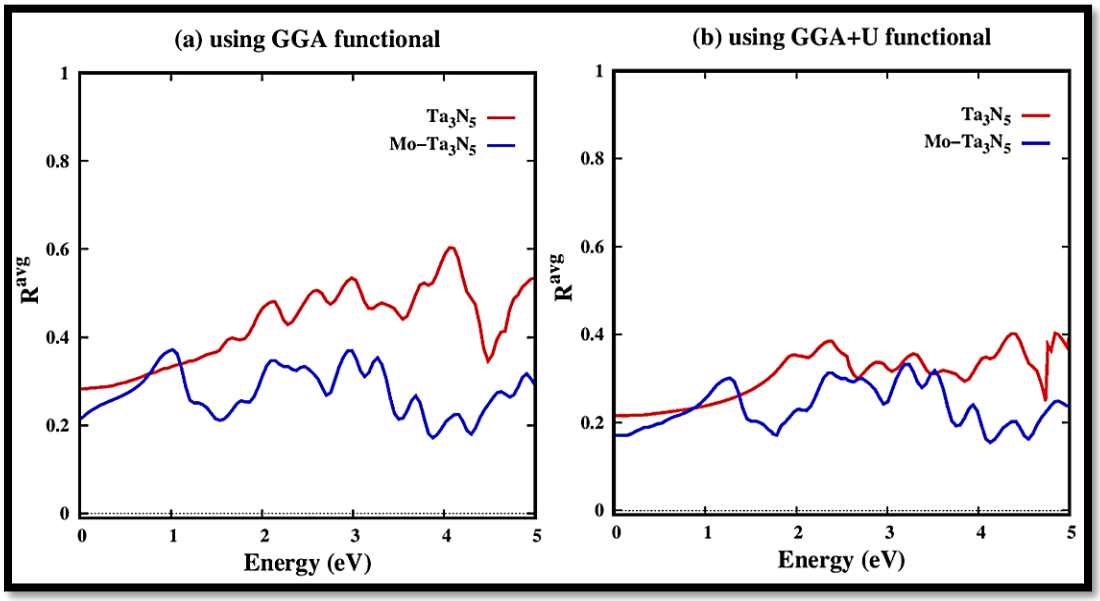

Figure 3-13 . Reflectivity of pure and Mo doped Ta_3N_5 calculated with GGA and GGA+U functional (u = 0.2).

Furthermore, we calculated the reflectivity at optical bandgap for pure and Mo doped system which is 35% for pure Ta_3N_5. This value matches very well with previously reported work [89]. However, for Mo doped Ta_3N_5 the reflectivity at optical band gap is 29%. The decrease in reflectivity observed when Mo is doped into Ta_3N_5 provides evidence of increased absorption in the visible region.

The refractive indices of pure and Mo doped Ta_3N_5 calculated through GGA and GGA+U calculations as a function of photon energy are shown in **Figure 3.14**. The refractive index of a material is proportional to the density of electron in the material. Therefore, higher the density of electron in the material, the higher will be the probability of photon to interact with electron. The GGA calculated value of the average refractive index at static limit η (0) for pure Ta_3N_5 is 3.41, while its value reported in previous work is 3.23. Similarly, the GGA static refractive index for Mo doped Ta_3N_5 is 3.75 and there is no literature available related to Mo doped Ta_3N_5 [89]. The increasing value of the static refractive index with Mo doping is due to the donor behavior of Mo. Furthermore, the GGA+U calculated static refractive index of pure and Mo doped Ta_3N_5 are 2.51 and 2.89, respectively. The static refractive index for Ta_3N_5 in previously reported work is 2.65 with GGA+U calculations [89], [99]. The refractive

index increases with increasing energy; reaches its maximum value followed by a decrease. This trend is in line to the calculated optical properties mentioned above.

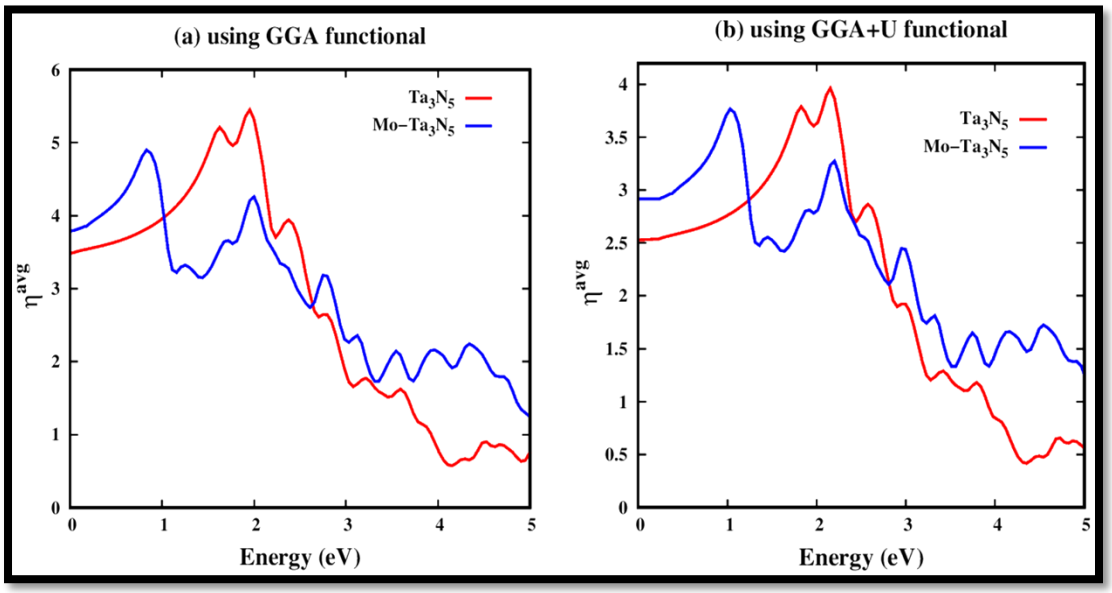

Figure 3-14 GGA and GGA+U calculated refractive index of pure and Mo doped Ta_3N_5 (u = 0.2).

The EEL spectrum of pure and Mo doped Ta_3N_5 is shown in **Figure. 3.15**. At the bandgap energy the EEL is larger for Mo doped Ta_3N_5 compared to pure Ta_3N_5 and it increases with the photon energy. As a result, the probability of interaction of electrons within the Mo doped Ta_3N_5 increases for GGA and GGA+U . The calculated EEL spectrum in the present work coincides very well with the previous work where A.H. Reshak calculated the EEL spectrum for pure Ta_3N_5 which also presented an increase in EEL for increasing photon energy above the bandgap [92], [89].

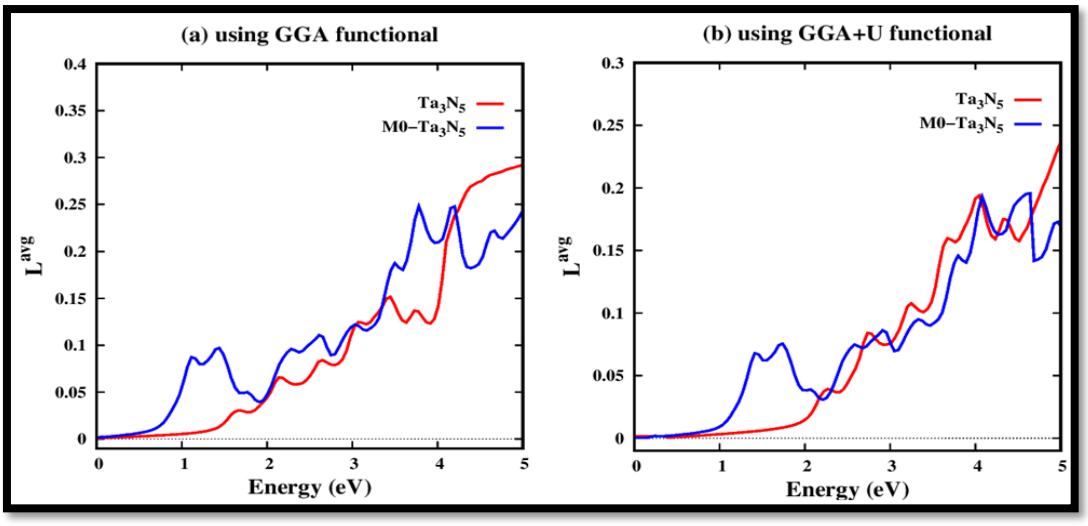

Figure 3-15 The GGA and GGA+U calculated electron energy loss spectrum of pure and Mo doped Ta_3N_5 (u = 0.2).

The GGA and GGA+U calculated extinction coefficient of pure and Mo doped Ta_3N_5 versus the energy of photon are shown **in Figure 3.16 (a)** and **(b)**. The extinction coefficient is related to the imaginary part of the dielectric function [103], [92]. The extinction coefficient follows the same pattern as that of the imaginary part of the dielectric function (**Figure 3.10**). The electronic and optical properties of pure and Mo doped Ta_3N_5 matched very well in both calculations as GGA and GGA+U.

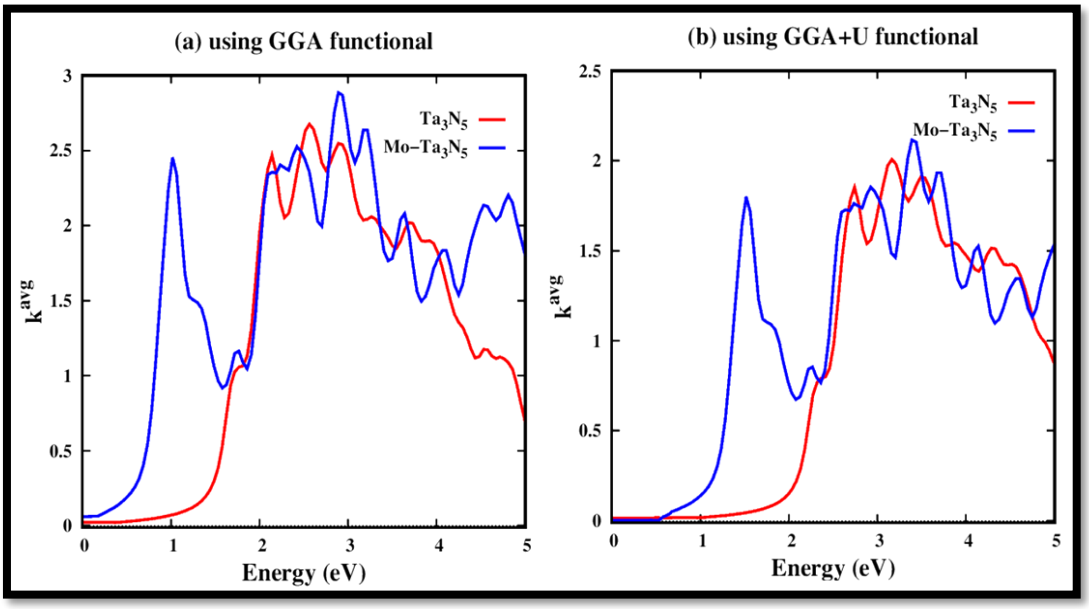

Figure 3-16 Extinction coefficient of pure and Mo doped Ta_3N_5 calculated with GGA and GGA+U functional (u = 0.2).

In summary, the optical properties of pure and Mo-doped Ta_3N_5 were investigated using GGA and GGA+U approximations. Various optical parameters were evaluated, including the real and imaginary parts of the dielectric constant, absorption, refractive index, reflectivity, EEL spectrum, and extinction coefficient. The calculated optical bandgap for pure Ta_3N_5 was found to be 1.40 eV using the GGA approximation. However, this value was underestimated, and the introduction of the GGA+U functional corrected the estimation, resulting in a calculated bandgap of 2.0 eV. For Mo-doped Ta_3N_5, the calculated optical bandgap was 0.98 eV with GGA and 1.20 eV with GGA+U. Regarding the static dielectric constant, the GGA approximation yielded values of 8.9 for pure and 11.58 for Mo-doped Ta_3N_5. With the GGA+U approximation, the static dielectric constant values were 6 for pure and 8.31 for Mo-doped Ta_3N_5. These values obeyed the Penn model. The absorption spectrum, as calculated using both GGA and GGA+U approximations, reveals a noticeable shift towards lower energy with the introduction of Mo doping. This shift indicates a change in the optical properties of the material due to the presence of Mo. In terms of reflectivity, the zero-frequency reflectivity calculated using GGA was found to be 27% for pure and 21% for Mo-doped Ta_3N_5, respectively. However, with GGA+U functional, the reflectivity values were 21% for pure Ta_3N_5 and 16% for Mo-doped Ta_3N_5. The calculated refractive indices, determined using the GGA approximation, were found to be 3.41 for pure and 3.75 for Mo-doped Ta_3N_5. However, these values were corrected using the GGA+U functional. As a result, the refractive index values for pure Ta_3N_5 was 2.51, while for Mo-doped Ta_3N_5, the corresponding value was 2.89. The EEL spectrum show that the matter energy interaction increases above the bandgap energy. The extinction coefficient calculated with GGA and GGA+U functional followed the same trend as that of imaginary part of dielectric constant.

3.3 Experimental results and discussions

3.3.1 Surface and structural characterization of Mo-doped Ta_3N_5

Figure. 3.17 (a) and **Figure. 3.17 (b)** show the surfaces and cross-sectional scanning electron microscopy (SEM) images of as-anodized Ta_2O_5 nanotubes. Anodization resulted in the formation of Ta_2O_5 nanotubes. The growth of the nanotubes can be controlled by controlling the temperature and the electrolyte composition [80]. Due to lower temperature of the electrolyte that we used here, the Ta_2O_5 nanotubes were

strongly adhered to the substrate. In addition, the HF concentration was kept lower i.e., 1 Vol % to form mechanically stable nanotubes. The average length of the nanotubes was 2.1 μm and the external diameter was 160 nm. These results are in good agreement with the previous literature [80]. **Figure. 3.18 (a)** illustrates the cross-section SEM image of as prepared Ta_3N_5 nanotubes by nitration of Ta_2O_5 at 900℃ for 3h. After nitration, a shrinkage in the nanotubes was experienced as the measured average length of the nanotubes was decreased to ~1.5 μm. This shrinkage in the nanotube's is because of the replacement of N in place of O to maintain the charge conservation [104]. It can also be understood from the valence electrons differences between O^{-2} and N^{-3}, that changed the coordination number. The decrease in the coordination number led to change the crystal structure and shrinkage of nanotubes [104]. **Figure 3.18 (b)** displays the cross-sectional image of Mo doped Ta_3N_5. The measured average length of the nanotubes remained ~1.5 μm for Mo doped Ta_3N_5 same as of pure Ta_3N_5.

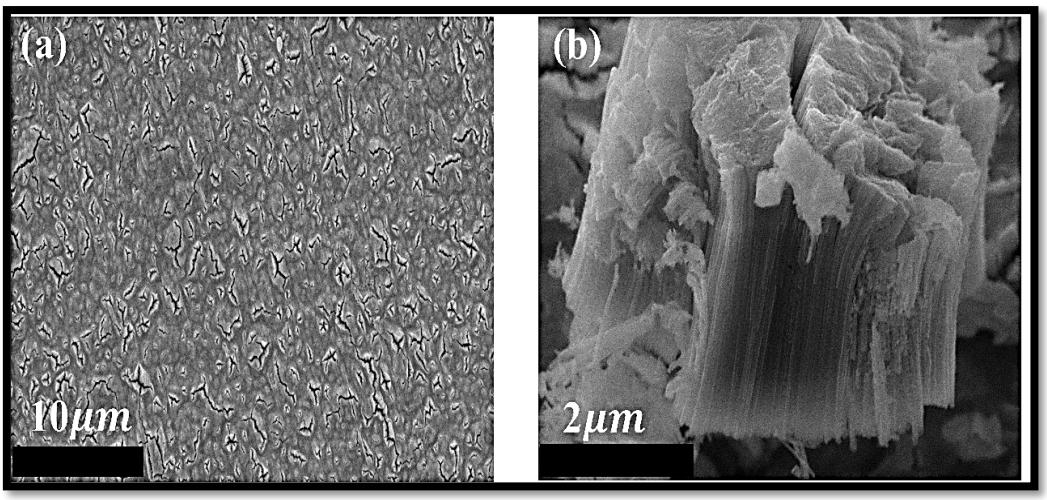

Figure 3-17 (a) Top view SEM image of Ta_2O_5 nanotubes, while (b) is the cross sections views of Ta_2O_5 nanotubes obtained in the electrolyte containing H_2SO_4 +1Vol% HF + 4 Vol% H_2O.

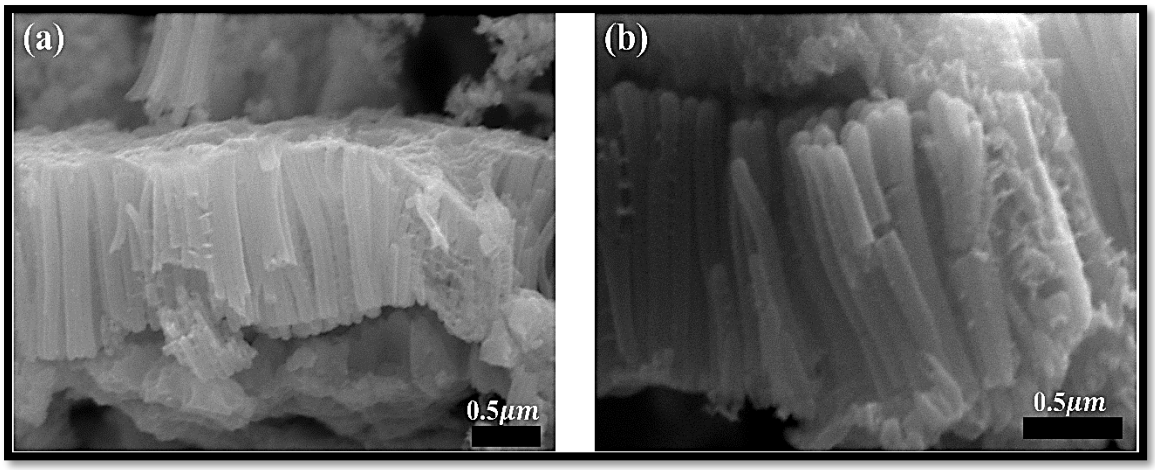

Figure 3-18 Cross-section SEM images of pure and Mo doped Ta_3N_5. (a) Pure Ta_3N_5 (b) Mo doped Ta_3N_5.

To reveal the Mo doping effect on the morphology of Ta_3N_5 nanotubes, the top views SEM images of pure Ta_3N_5, MTN-O.1, MTN-O.3 and MTN-0.5 were obtained and compared as shown in **Figure. 3.19 (a-d)**. Pure and doped samples have irregular surfaces revealing that there is no notable change in the morphology of pure and doped samples.

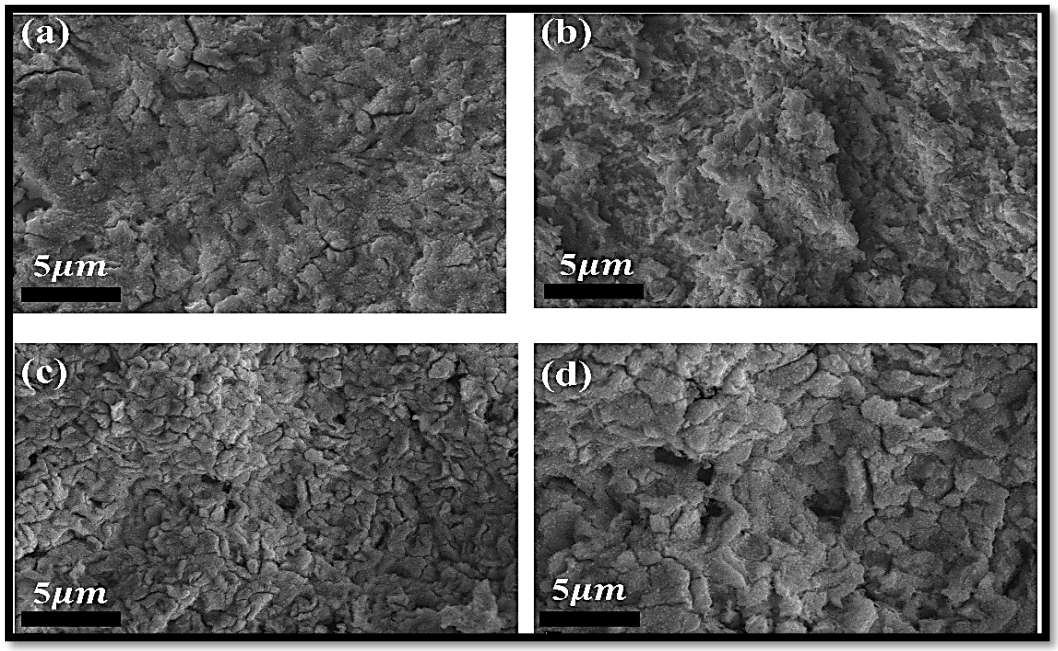

Figure 3-19 (a) SEM top view image of Ta_3N_5 nanotubes, (b) MTN-O.1, (c) MTN-0.3 and (d) MTN-0.5. The scale bar in the inserted images is 5μm.

Figure. 3.20 (a and **b**) shows the transmission electron microscopy (TEM) images of anodized Ta_2O_5 and Ta_3N_5 synthesized by nitridation at 900 ºC for 3h, respectively. Clearly a remarkable shrinkage was observed after 900°C nitridation. The measured outer diameter of anodized Ta_2O_5 from TEM image is 116 ± 5 nm while that of Ta_3N_5 is 65 nm ± 5 nm. These results matched very well with the SEM results discussed earlier where the same shrinkage was observed in the length of the nanotubes (**Figure 3.18**).

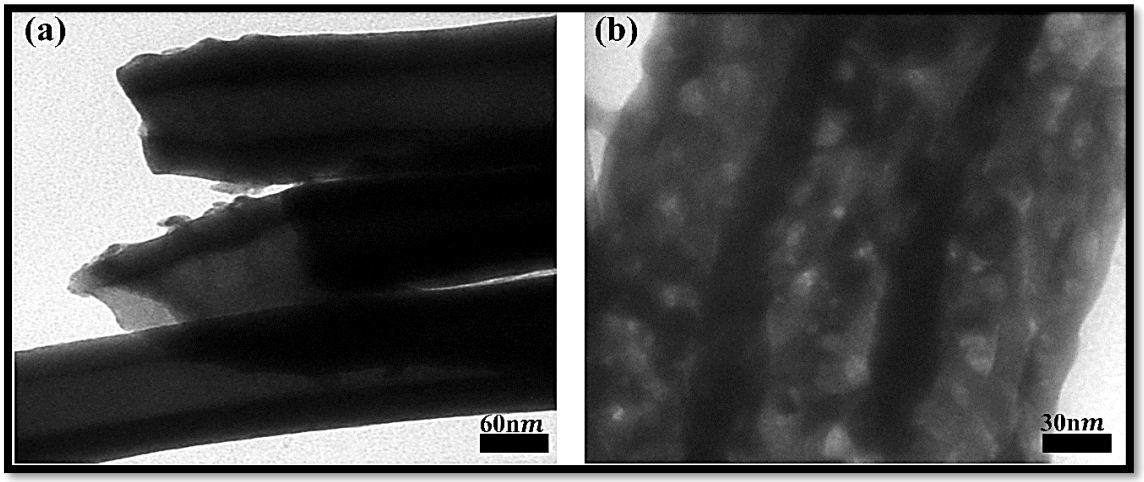

Figure 3-20 TEM images of (a) as-anodized Ta_2O_5 and (b) Ta_3N_5 prepared at 900 °C for 3h.

To confirm the uniform distribution and the presence of O and Ta, the energy dispersive X-Ray (EDX) mapping images of anodized Ta_2O_5 films were obtained **Figure. 3.21 (a-d)**. These maps show the uniform distribution of Ta and O elements on the surface of the film.

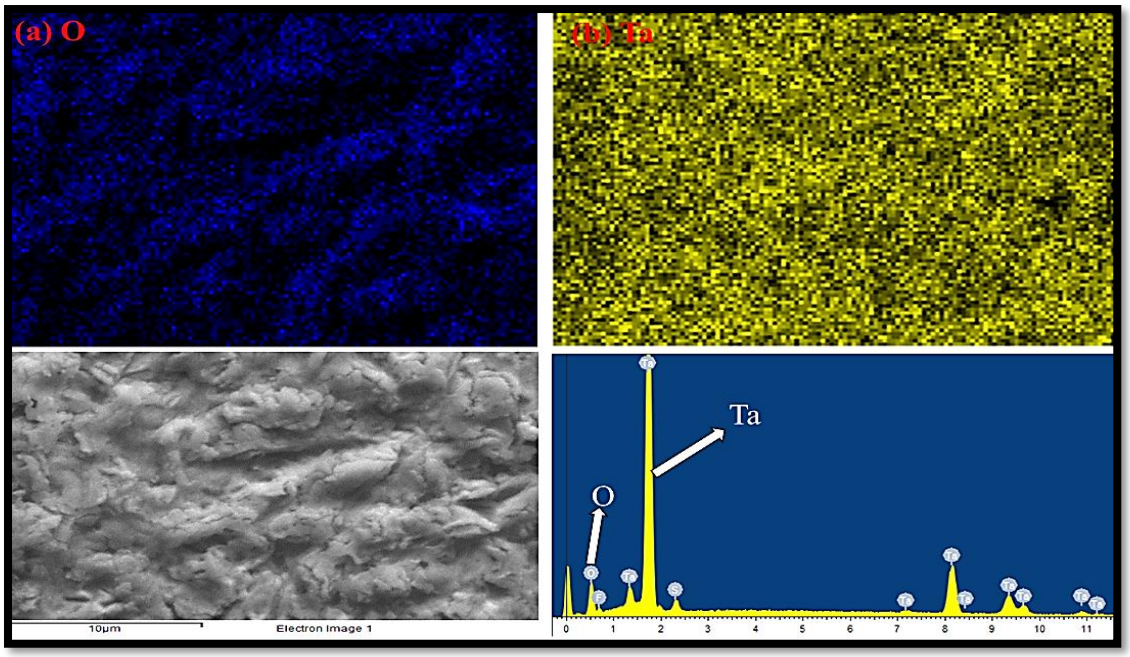

Figure 3-21 (a, b) EDS elemental mapping images of Ta_2O_5 and (C) SEM image and (d) EDS line profile of Ta_2O_5.

Figure 3.22 (a-d) indicate a uniform distribution of Ta, O, N, and Mo elements throughout the film. Upon increasing the dopant (Mo) concentration, the weight% of Mo in the EDX also increases as shown (**Table. 3.7).**

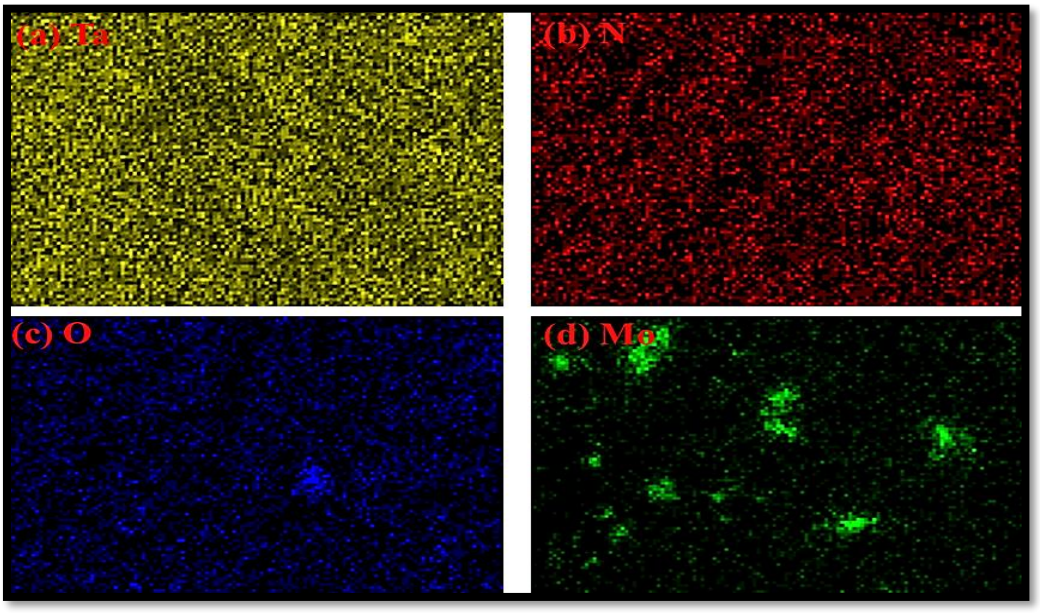

Figure 3-22 (a, d) EDS elemental mapping images of Mo doped Ta_3N_5.

Table 3-7 EDX table of all samples with wt.% of each element.

Elemental analysis (Wt%)

Sample	O	N	Ta	S	Mo
Ta_2O_5	60.02	0	36.66	3.32	0
Ta_3N_5	5.35	57.44	37.21	0	0
MTN-0.1	6.37	54.99	38.22	0	0.42
MTN-0.3	8	55.60	35.35	0	1.05
MTN-0.5	9	51.68	36.53	0	2.75

To investigate the crystal structure of as-synthesized nanotubes, grazing angle XRD was performed that helped decrease the signal contribution from the underlying substrate. XRD patterns of Ta_2O_5 (heated at 500°C in air), Ta_3N_5 and Mo doped Ta_3N_5 are shown in **Figure. 3.23**. From XRD, it is confirmed that the nitridation of Ta_2O_5 at 900°C completely changes the crystal structure from orthorhombic Ta_2O_5 to orthorhombic Ta_3N_5 [104]. For nitride samples, $2\theta \sim 24.5^{o}$, 35^{o} and 36^{o}, correspond to miller indices [110], [130] and [113] for Ta_3N_5, respectively Though we used grazing angle XRD, we observed substrate contribution in the XRD diffractograms, particularly the signals from Ta_2N at $2\theta \sim$ that form at the interface of Ta substrate and the bottom of Ta_2O_5 nanotubes during nitridation [55], [104]. This metallic phase was designated as a good electron transfer facilitator in the literature. After adding Mo in Ta_3N_5, no extra peaks appeared in the diffractogram, showing no extra phase was formed due to the addition of Mo. The experimental lattice constants measured form the XRD analyses match well with their theoretical values **(Table 3.8).**

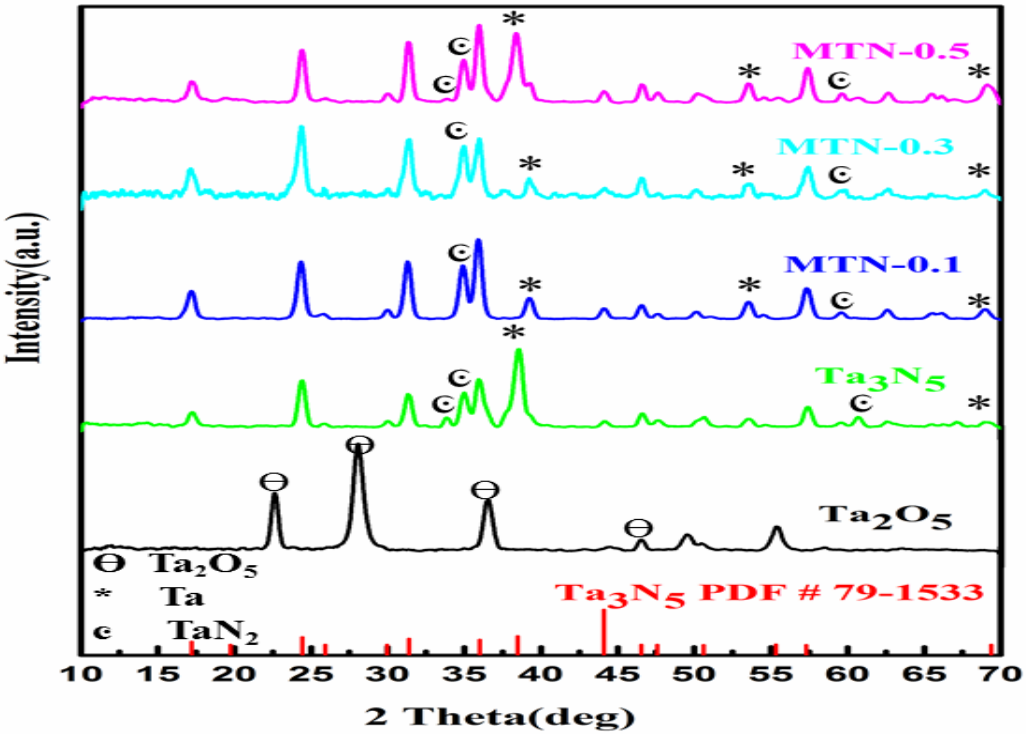

Figure 3-23 XRD patterns of pure and Mo-doped Ta_3N_5.

Table 3-8 Experimental and theoretical lattice parameters of Mo-doped Ta_3N_5.

Lattice Parameters	A (Å)	B (Å)	C (Å)	α (°)	β (°)	γ (°)	Ref
Experimental	3.88	10.21	10.26	90	90	90	Present Work
Theoretical	3.88	10.24	10.28	90	90	90	Present Work
Theoretical	3.87	10.23	10.29	90	90	90	[96]

Figure. 3.24 (a) represents the absorption spectra of pure and Mo doped Ta_3N_5. The absorption edges (bandgap) of all samples are given in **Table. 3.9**. These absorption edges correspond to the excitation of electron from N 2p orbitals to Ta 5d empty orbitals. Although the observed bandgap change was not that significant compared to

theoretically calculated bandgap (**Figure 3.8**), it is worth noting that the absorption tail for Mo-doped samples at higher wavelengths above the bandgap demonstrated a decrease. This decrease suggests the inhibition of reduced Ta species, a phenomenon often reported in the literature [105], [45]. Furthermore, experimentally transforming Ta_2O_5 into Ta_3N_5 by nitridation does not completely remove the 3-coordenated lattice O which has a profound effect on the crystal structure and the optical properties of experimentally synthesized Ta_3N_5 [53], [55]. However. the DFT calculations did not account for this particular effect.

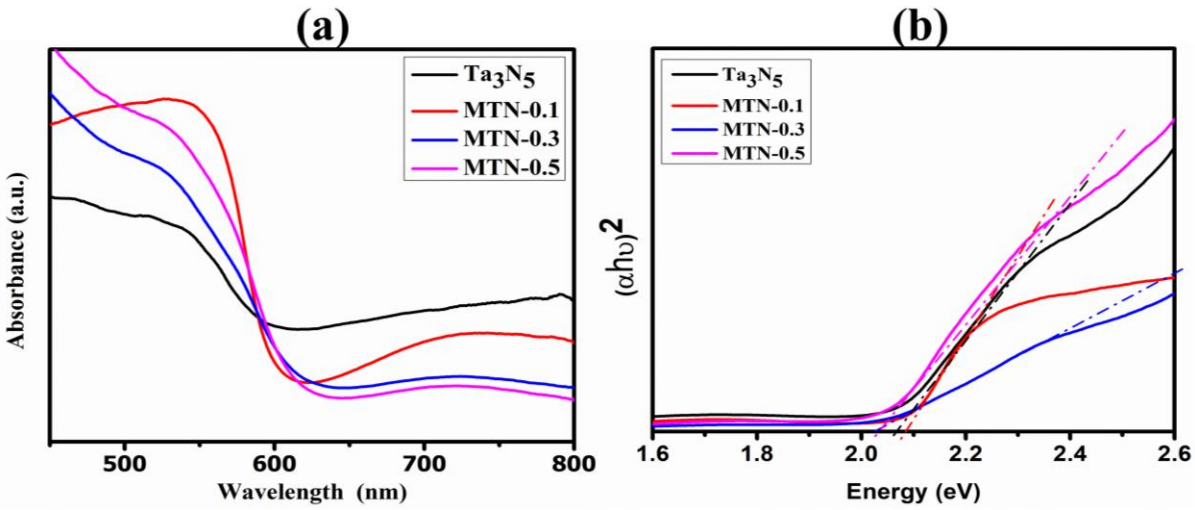

Figure 3-24 a) UV-visible absorption spectra and (b) Tauc plots of pure and Mo doped Ta_3N_5 samples.

Table 3-9 Experimental bandgap and absorption edge of pure and Mo doped Ta_3N_5.

Sample	Bang gap (eV)	Absorption edge (nm)
Pure Ta_3N_5	2.10	613
MTN-0.1	2.05	617
MTN-0.3	2.04	640
MTN-0.5	2.05	634

Furthermore, X. Zou et al reported Zr doping in Ta_3N_5 which exhibited similar trend for the bandgap [45]. The phase composition and microstructure of the pure and doped Ta_3N_5 was investigated by Raman spectroscopy shown in **Figure. 3.25 (a)**. The

characteristics of Raman spectra of all samples are almost similar, as no extra peaks were observed. The frequencies in characteristics Raman spectra at 270 cm^{-1} ± 3 cm^{-1} , 404 cm^{-1} ± 3 cm^{-1} , 527 cm^{-1} ± 3 cm^{-1} and 598 cm^{-1} ± 3 cm^{-1} can be assigned to A_g vibration modes, while around 495 ± 3 cm^{-1} , 749 cm^{-1} ± 3 cm^{-1} , 823 cm^{-1} ± 3 cm^{-1} correspond to B_g vibration modes [128]. These results matched with previously reported work for Ta_3N_5 [61] . The Raman bands observed at 270 cm^{-1} ± 3 cm^{-1} 404 cm^{-1} ± 3 cm^{-1} correspond to the bending vibration of the Ta–N–Ta. This is the clear identification of orthorhombic crystal structure of Ta_3N_5 [61]. Interestingly, a shift in the A_g mode peak was observed attributed to Mo doping of Ta_3N_5 (Figure 3.25b). For the sample MTN-O.1 the full width half maximum of the A_g mode located at 271cm-1 is reduced and the peak position shows a distinct red shift, the similar behavior is also observed for MTN-0.3 sample. But upon further increasing the Mo concentration the order of the change in the prominent A_g mode was reversed. These changes may be due to the additional disorder created by a very high amount of Mo in the crystal lattice of Ta_3N_5.

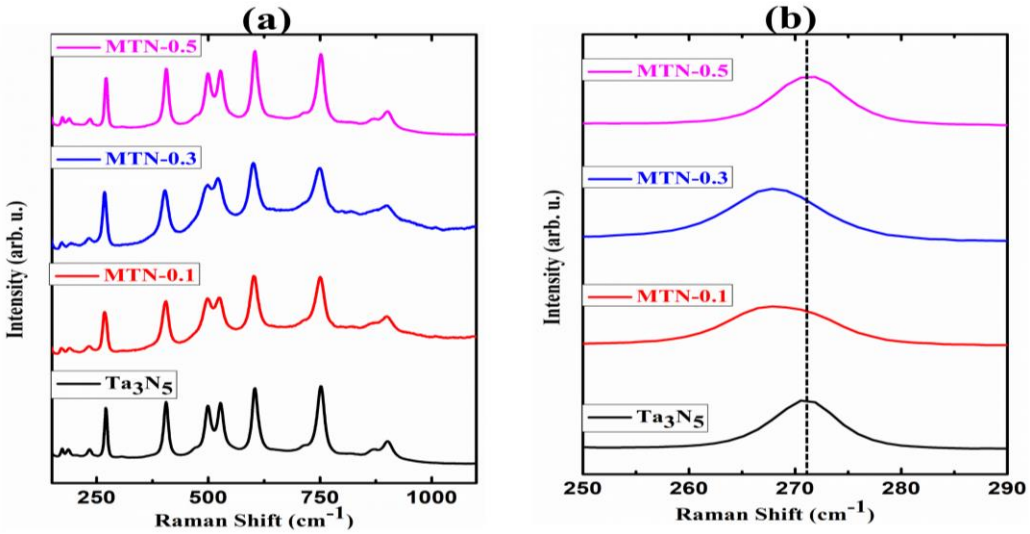

Figure 3-25 Raman Scattering spectrum of pure and Mo doped samples. (b) Representing the main A_g mode peak of pure and Mo doped Ta_3N_5.

To elucidate the surface elemental composition and chemical states of the prepared pure and doped Ta_3N_5, the X-rays photoelectron spectroscopy (XPS) was conducted. The survey scan XPS spectra of pure and doped Ta_3N_5 are displayed in **Figure. 3.26**. In which the characteristics binding energy peaks of Ta 4f, O 1s, and N 1s are clearly observed. The Mo 3d peak is observed in the doped Ta_3N_5 and this is the clear indication of Mo presence. The appearance of O peaks was not completely inhibited in XPS

spectra after the nitridation. Henderson et al. demonstrated that oxygen residuals in Ta_3N_5 cannot be fully removed after nitridation.

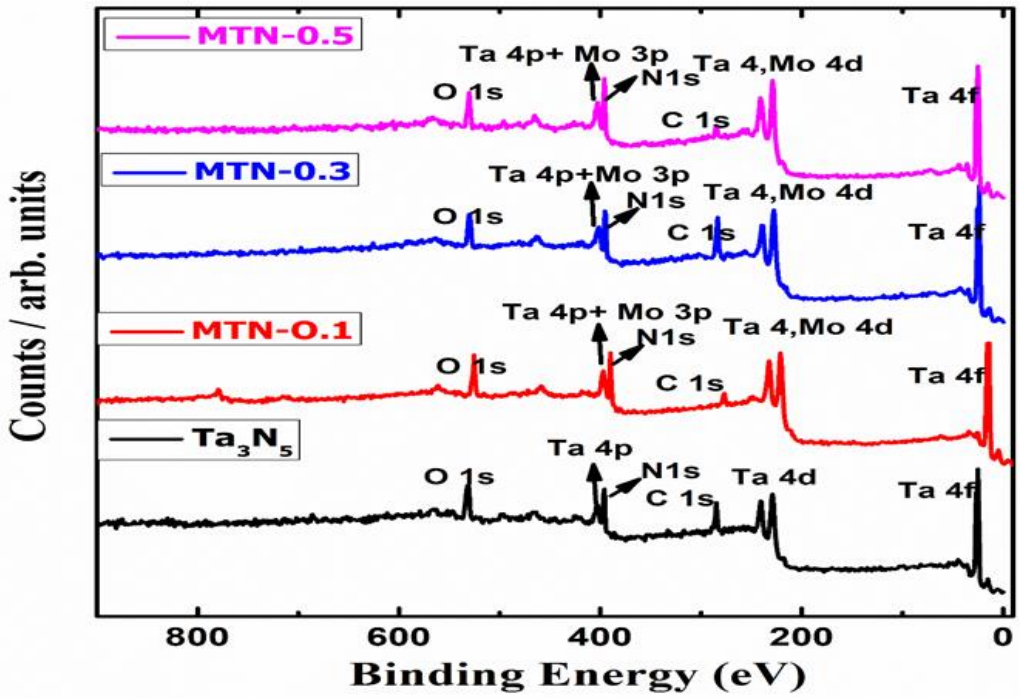

Figure 3-26 Survey scan XPS spectra from 0 to 900 eV of pure and doped Ta_3N_5.

Two doublets of Ta 4f7/2 (24.72 eV, 26.61 eV) and Ta 4f5/2 (25.61 eV, 27.50 eV) were clearly appeared in all samples whether it's pure or doped one where the lower energy doublet corresponds to Ta_3N_5 and the higher one corresponds TaO_xN_x [53], [106]. Mo 3d overlaps with Ta 4d (**Figure 3.27**), therefore, Ta4d/Mo3d region was carefully de-convoluted. An increase in the Mo content was observed due to increasing amount of Mo in the hydrothermal reaction (**Table 3.10**).

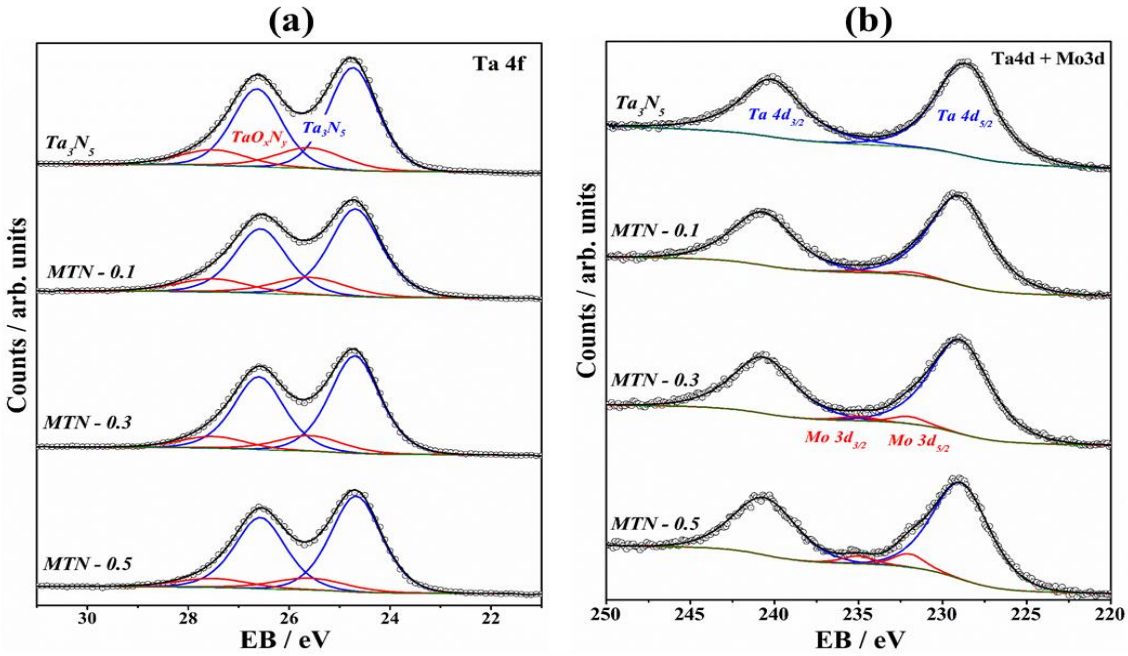

Figure 3-27 XPS core level spectra of Ta and Mo, (a) representing the Ta 4f while (b) is Ta 4d and Mo 3d.

Figure 3.28 (a) represents high resolution N 1s, Ta $4p_{3/2}$ and Mo $3p_{3/2}$ peaks for pure and doped samples located at the binding energy of 396.34 eV, 407.67 eV and 394.19 eV, respectively. Because of the similar binding energy range of Mo 3p and N 1s due to overlapping peaks, the Mo 3p peak was not clearly distinguished from N 1s. The N 1s peak of all samples was observed at a binding energy of 396.4 eV (Figure. 3.28). There is no clear change in the binding energy of N 1s peak**.** Figure 3.28 b represents the de-convoluted O 1s peak. The O 1s state can be de-convoluted into three overlapping peaks (**Figure. 3.28 b**). The peak located at 530 eV corresponds to O-Ta and the O1s peaks at higher bonding energies (~531.83 and ~533.28 eV) are attributed to the hydroxyl groups [53], [104]. After Mo doping O/Ta increases attributed to the charge accommodation when Ta^{5+} is replaced by Mo^{4+}.

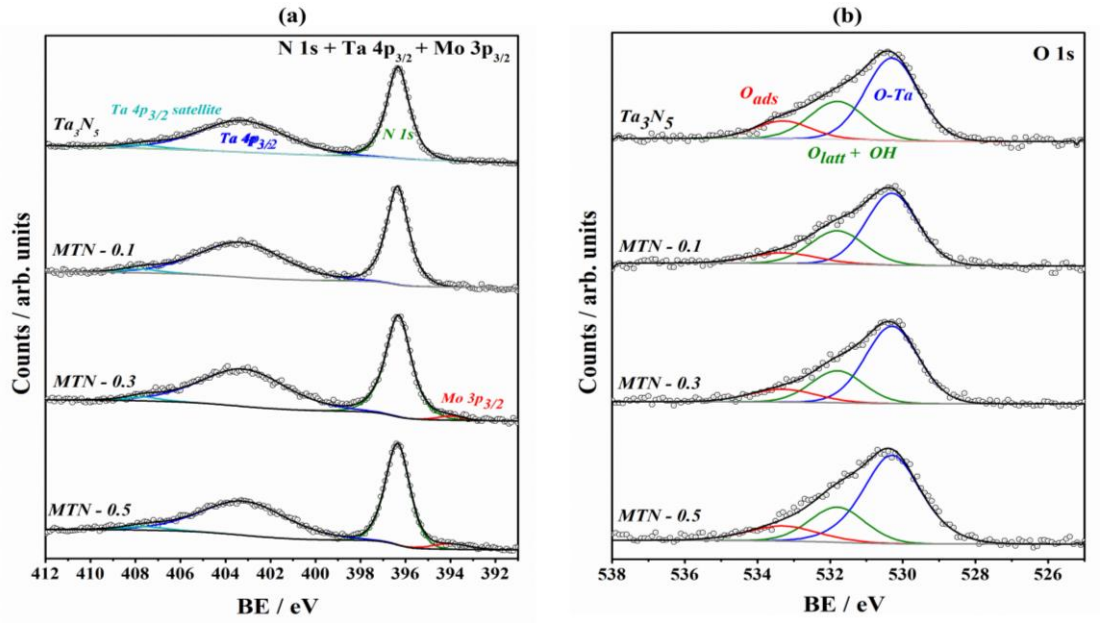

Figure 3-28 XPS spectra of N 1s and O 1s orbitals of pure and Mo doped Ta_3N_5, (a) representing N 1s, Ta $4p_{3/2}$ and Mo $3p_{3/2}$ while (b) representing the O 1s state of all samples.

Table 3-10 Summarize results of XPS of pure and doped Ta_3N_5.

Samples	N/Ta	O/Ta	Mo/Ta	Ref
Ta_2O_5	---	1.70	----	Present Work
Ta_3N_5	1.50	0.20	---	Present Work
Ta_3N_5	1.59	0.22	-----	[79]
MTN-0.1	1.45	0.30	0.10	Present Work
MTN-0.3	1.49	0.50	0.15	Present Work
MTN-0.5	1.58	1.13	0.17	Present Work

3.4 Water Oxidation performance of pure Ta_3N_5 and MTN-x (x = 0.1, 0.3 and 0.5 M) photoanode with and without co-catalyst

Figure 3.29 illustrates the results of linear sweep voltammetry (LSV) of pure and Mo doped Ta_3N_5 with and without the Co(OH)x co-catalyst. All LSV measurements were conducted in an alkaline electrolyte 1M KOH with a pH of 13.6 using a three-electrode photoelectrochemical (PEC) cell under chopped on/off light

illumination at a constant time interval (AM 1.5G simulated sun light). During chopped illumination, transient photocurrent spikes were observed, primarily attributed to the accumulation of holes at the electrode-electrolyte interface. Both pure and Mo-doped Ta_3N_5 exhibit significantly low current densities without co-catalyst decoration due to their high electron-hole recombination rates and limited stability under illumination. The reported current densities for Ta_3N_5, MTN-0.1, MTN-0.3, and MTN-0.5 were 0.78 mA/cm², 2 mA/cm², 1 mA/cm², and 0.8 mA/cm², respectively, at 1.23 $V_{RHE,}$ as illustrated in **Figure 3.29 (a)**. When the voltage exceeds 1.2 V_{RHE} and the light is switched on, we observed anodic spikes that rapidly decay, which can be attributed to the recombination of electron-hole pairs. When the surfaces of both the pure and Mo-doped samples were modified with the application of a co-catalyst ($Co(OH)_x$), an apparent increase in the current density was observed for all samples, as illustrated in **Figure 3.29 (b)**. The current density for pure Ta_3N_5, with co-catalyst modification, reached 0.86 mA/cm² at 1.23 V_{RHE}, whereas MTN-0.1-Co exhibited the highest current density, reaching 3.7 mA/cm² at 1.23 V_{RHE}. These results clearly indicate a substantial increase in current when Mo is introduced into Ta_3N_5. This increase can be attributed to several factors associated with Mo doping in Ta_3N_5, including an expanded light absorption range, enhanced charge separation, improved charge transfer, and faster reaction kinetics. When the Mo doping exceeded 0.1M, a decrease in current density was observed as compared to MTN-0.1-Co, likely attributed to scattering caused by impurities or the formation of defects resulting from excessively high Mo concentrations. The summary of all the photoelectrochemical (PEC) results is presented in the following **Tables (3.11 and 3.12)**.

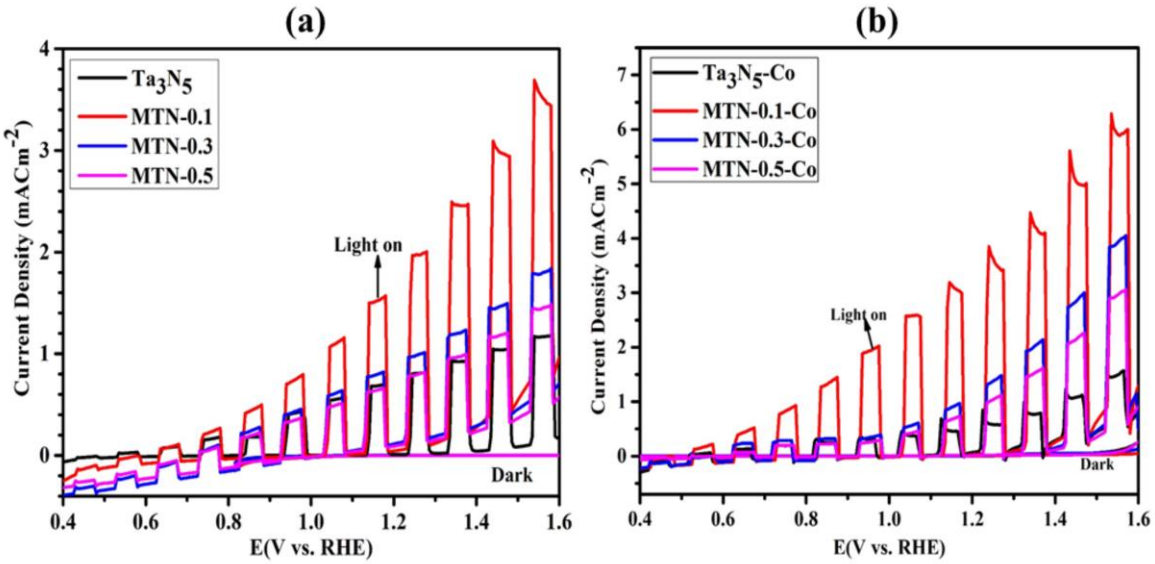

Figure 3-29 Current-potential curves under dark and chopped conditions. (a) Representing the pure and Mo doped Ta_3N_5 without co-catalyst while (b) is the current density with co-catalyst.

Table 3-11. Water oxidation activity of pure Ta_3N_5 and MTN-x (x = 0.1, 0.3 and 0.5) without co-catalyst.

	Ta_3N_5	MTN-0.1	MTN-0.3	MTN-0.5
J at 1.23 V_{RHE} ($mAcm^{-2}$)	0.78	2	1	0.8
J at 1.54 V_{RHE} ($mAcm^{2}$)	1.16	3	1.78	1.43
Onset potential (V_{RHE})	0.94	0.73	0.83	0.86

Table 3-12 Water oxidation activity of pure Ta_3N_5 and MTN-x (x = 0.1, 0.3 and 0.5) with co-catalyst.

	Ta_3N_5-Co	MTN-0.1-Co	MTN-0.3-Co	MTN-0.5-Co
J at 1.23 V_{RHE} ($mAcm^{-2}$)	0.86	3.7	1.30	1
J at 1.54 V_{RHE} ($mAcm^{-2}$)	1.56	6.1	3.8	2.9
Onset potential (V_{RHE})	0.72	0.57	0.62	0.66

The onset potential for all samples, whether pure Ta_3N_5 or MTN-X, was determined with and without co-catalyst modification. In this context, onset potentials were defined

as the potentials at which the photocurrent reached 0.2 mA/cm², as illustrated in **Figure 3.30**. Details regarding the onset potential can be found in **Tables (3.11 and 3.12)**. The calculated onset potential for pure Ta_3N_5 was 0.94 V_{RHE} (**Figure 3.30 (a)**), whereas for MTN-0.1, MTN-0.3, and MTN-0.5, it measured values were 0.73 V_{RHE}, 0.83 V_{RHE}, and 0.86 V_{RHE}, respectively. These results clearly indicate that Mo doping caused a cathodic shift in the onset potentials, reducing them as compared to pure Ta_3N_5. These results are consistent with the current density findings, showing that MTN-0.1 achieved the highest current density. With co-catalyst modification, the lowest onset potential was calculated for MTN-0.1-Co, was 0.57 V_{RHE} **Figure 3.30 (b)**. From this comparison, it was evident that when the concentration of Mo is 0.3M, the most prominent outcomes were observed: the lowest onset potential and the highest photocurrent. These results are consistent with previous literature, which demonstrated a cathodic shift in the onset potential when Zr doping was introduced into Ta_3N_5 [45]. This study provides clear evidence that the introduction of Mo into Ta_3N_5 can effectively tune surface defects and mitigate electron-hole recombination.

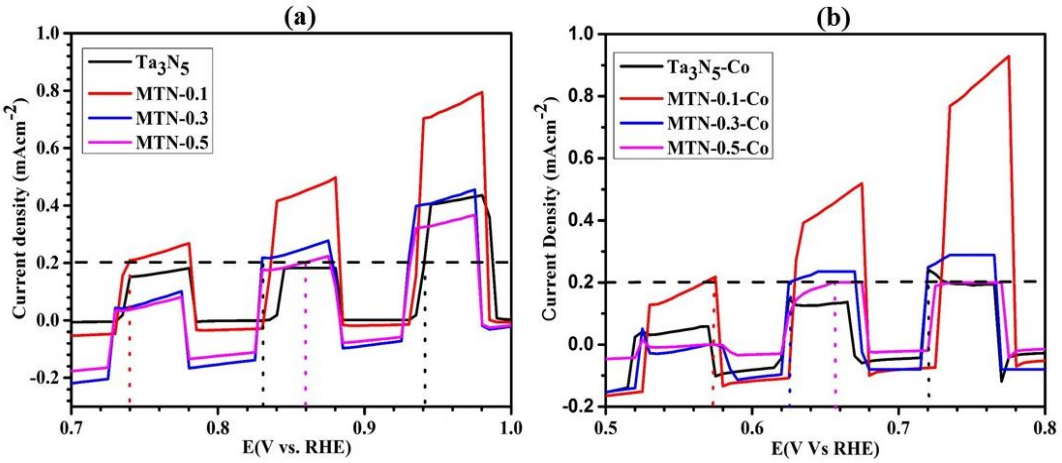

Figure 3-30 Current vs potential curves under AM 1.5G-simulated sun light of pure Ta_3N_5 and MTN-x (a) without co-catalyst (b) with co-catalyst.

3.5 Partial conclusions

In this work, experimental and theoretical (first principle DFT based calculations) studies of pure and Mo doped Ta_3N_5 have been conducted. The electronic and optical properties of pure and Mo doped Ta_3N_5 were calculated by GGA and GGA+U functional. GGA underestimated the bandgap energy which was corrected by

adding Hubbard parameter U. The calculated formation energy showed that the Mo doped at high x-coordinates value is thermodynamically stable. The elemental Mo doping changes the nature of the electronic bandgap from indirect semiconductor to direct semiconductor. Meanwhile with Mo doping the bandgap decreased. This decrease in the bandgap value can be attributed to the unoccupied Mo4d states. The total density of states showed that the conduction band of Mo doped is composed of Mo 4d and Ta5d states. The optical properties of Mo doped Ta_3N_5 matched very well with the electronic properties and show the enhancement of absorption toward lower spectrum of electromagnetic radiation. This study shows that the bandgap can be engineered with Mo doping. The optical functions of pure and Mo doped Ta_3N_5 show that there is high optical anisotropy that exists in both pure and Mo doped Ta_3N_5. The dielectric constant of Ta_3N_5 increased with Mo from 6 to 8.31. The reflectivity at optical bandgap value decreased from 35% to 29% with Mo doping in Ta_3N_5. Mo doping in Ta_3N_5 led to a noticeable enhancement in the static refractive index, increasing from 2.51 for pure Ta_3N_5 to 2.89 when Mo was incorporated. This increase indicates a significant modification in the optical properties within the material. The EEL spectrum analysis revealed an increase in the light-matter interaction following the determination of the optical bandgap values for both pure and Mo-doped Ta_3N_5. The extinction coefficient followed the same trend that of the imaginary part of dielectric constant. Attempts were made to experimentally synthesize Mo doped Ta_3N_5 which were prepared by the nitridation of Ta_2O_5 nanotubes. The average length of as anodized nanotubes was 2.1 µm which decreased to 1.5 µm after nitridation related to the density difference of Ta_2O_5 to Ta_3N_5. The experimental bandgap was slightly redshifted by Mo doping and band transitions for higher wavelengths above the bandgap decreased in UV Vis spectroscopy which indicate inhibition of the reduced Ta species. The XRD data confirmed the presence of the orthorhombic phase in Ta_3N_5, providing structural information about the material. The characteristic diffraction peaks and their positions in the XRD pattern verified the crystalline nature and specific crystal structure of Ta_3N_5. Furthermore, the Raman and X-ray photoelectron spectroscopy (XPS) spectra provided additional evidence of Mo doping in Ta_3N_5. Additionally, the energy-dispersive X-ray spectroscopy (EDX) spectrum further supported the existence of Mo in Ta_3N_5. The photoelectrochemical water oxidation test demonstrated that Mo doping can enhance the water oxidation performance of Ta_3N_5. The calculated current density for Ta_3N_5 was 0.78 mA/cm² at 1.23 V_{RHE}, and this value increased to 2 mA/cm² with the introduction

of Mo doping, without co-catalyst modification. MTN-0.1 exhibited the highest current density, reaching 3 mA/cm² at 1.54 V_{RHE}. This study reveals that Mo doping not only enhances the water oxidation performance of Ta_3N_5 but also shifts the onset potential towards lower values. When the surface is modified with Co(OH)x as a co-catalyst, the photoanode reaches its peak performance, achieving a remarkable maximum current density of 6.1 mA/cm² at 1.54 V_{RHE}, accompanied by a notable reduction in the onset potential to just 0.57 V_{RHE}.

Chapter 4 General Conclusions and Future Work

In this comprehensive study, we conducted both experimental and theoretical investigations on pure and Mo-doped Ta_3N_5. Utilizing first-principle DFT-based calculations, we delved into the electronic and optical properties of pure and Mo doped Ta_3N_5, employing GGA and GGA+U functional to correct the bandgap energy underestimation. Our results revealed that Mo doping, particularly at higher x-coordinates, is thermodynamically stable and leads to a transition of Ta_3N_5 from an indirect to a direct bandgap semiconductor, along with a reduction in the bandgap energy. This change can be attributed to the presence of unoccupied Mo4d states. Furthermore, Mo-doped Ta_3N_5 exhibited enhanced absorption in the lower electromagnetic radiation spectrum, showcasing the tunability of the bandgap through Mo doping. We also observed significant optical anisotropy, an increase in the dielectric constant from 6 to 8.31 with Mo doping, and decrease in reflectivity at the optical bandgap value from 35% to 29%. Additionally, a noticeable enhancement in the static refractive index from 2.51 to 2.89 with Mo incorporation. EEL spectrum analysis indicated increased light-matter interaction in doped system as compared pure Ta_3N_5.

In our experimental efforts, we synthesized Mo-doped Ta_3N_5 via the nitridation of Mo-Ta_2O_5 nanotubes, observing a slight redshift in the bandgap and reduced band transitions in UV Vis spectroscopy, signifying inhibition of the reduced Ta species. XRD, Raman, XPS and EDX, techniques confirmed the successful Mo doping in Ta_3N_5. Furthermore, our photoelectrochemical water oxidation tests showcased the remarkable enhancement in water oxidation performance with Mo doping. Specifically, the current density increased from 0.78 mA/cm² at 1.23 V_{RHE} to 2 mA/cm² at 1.23 V_{RHE} with Mo doping, and MTN-0.1 exhibited the highest current density 3 mA/cm² at 1.54 V_{RHE}. This study highlights the multifaceted benefits of Mo doping, including improved water oxidation performance and shifted onset potentials. When the surface is modified with Co(OH)x as a co-catalyst, the photoanode reaches its peak performance, achieving a remarkable peak current density of 6.1 mA/cm² at 1.54 V_{RHE}, accompanied by a notable reduction in the onset potential to just 0.57 VRH V_{RHE}.

In the future, I aspire to synthesize photanodes doped with Ti, V, and Cr in Ta_3N_5 and apply them to the field of water oxidation. The theoretical calculations for these materials have laid the foundation for this endeavor. The synthesis, characterization and application of these advanced materials in photoelectrochemical water splitting is in process.

The CrSSe is new 2D material predicated by the author research group. The predicted electronic properties make Janus CrSSe as a promising candidate for applications in photocatalysis, solar cells, supercapacitors, and spintronic devices, showcasing its potential for a wide range of technological advancements

References

[1] L.T. Poaty, Hematite as a photocatalyst material View project 2D Materials for spintronics applications View project.

https://www.researchgate.net/publication/355679589.

[2] A.G. Khan, S.A. Ganie, I. Showqi, A Brief Review on Global Warming and Climate Change: Consequences and Mitigation Strategies Paper Making Potential of Selected Herbaceous Species of Kashmir Valley as an Alternative to Woody Species Using Biotechnological Approach-A Way Forward Towards Sustainable Development View project Call for Book Chapters View project, 2018. https://www.researchgate.net/publication/324818247.

[3] G.P. Peters, O. Geden, Catalysing a political shift from low to negative carbon, Nat. Clim. Chang. **7** (2017) 619–621. https://doi.org/10.1038/nclimate3369.

[4] M. Granovskii, I. Dincer, M.A. Rosen, Environmental and economic aspects of hydrogen production and utilization in fuel cell vehicles, J. Power Sources. **157** (2006) 411–421. https://doi.org/10.1016/j.jpowsour.2005.07.044.

[5] Z.X. Guo, C. Shang, K.F. Aguey-Zinsou, Materials challenges for hydrogen storage, J. Eur. Ceram. Soc. **28** (2008) 1467–1473. https://doi.org/10.1016/j.jeurceramsoc.2007.12.019.

[6] K.T. Møller, T.R. Jensen, E. Akiba, H. wen Li, Hydrogen - A sustainable energy carrier, Prog. Nat. Sci. Mater. Int. **27** (2017) 34–40. https://doi.org/10.1016/j.pnsc.2016.12.014.

[7] A. Fujishima and K. Honda, Nature, 1972, **238**, 37–38.

[8] S. Li, J. Zhang, S. Hu, K. Xu, W. Jiang, J. Liu, Synthesis of flower-like Ta_3N_5-Au heterojunction with enhanced visible light photocatalytic activity, J. Alloys Compd. **695** (2017) 1137–1144. https://doi.org/10.1016/j.jallcom.2016.10.240.

[9] J. Xiao, J.J.M. Vequizo, T. Hisatomi, J. Rabeah, M. Nakabayashi, Z. Wang, Q. Xiao, H. Li, Z. Pan, M. Krause, N. Yin, G. Smith, N. Shibata, A. Brückner, A. Yamakata, T. Takata, K. Domen, Simultaneously Tuning the Defects and Surface Properties of Ta_3N_5 Nanoparticles by Mg-Zr Codoping for Significantly

Accelerated Photocatalytic H_2 Evolution, J. Am. Chem. Soc. **143** (2021) 10059–10064. https://doi.org/10.1021/jacs.1c04861.

[10] K. Maeda, N. Nishimura, K. Domen, A precursor route to prepare tantalum (V) nitride nanoparticles with enhanced photocatalytic activity for hydrogen evolution under visible light, Appl. Catal. A Gen. **370** (2009) 88–92. https://doi.org/10.1016/j.apcata.2009.09.024.

[11] Y. Li, L. Zhang, A. Torres-Pardo, J.M. González-Calbet, Y. Ma, P. Oleynikov, O. Terasaki, S. Asahina, M. Shima, D. Cha, L. Zhao, K. Takanabe, J. Kubota, K. Domen, Cobalt phosphate-modified barium-doped tantalum nitride nanorod photoanode with 1.5% solar energy conversion efficiency, Nat. Commun. **4** (2013). https://doi.org/10.1038/ncomms3566.

[12] M. Gurulakshmi, M. Selvaraj, A. Selvamani, P. Vijayan, N.R. Sasi Rekha, K. Shanthi, Enhanced visible-light photocatalytic activity of V_2O_5/S-TiO_2 nanocomposites, Appl. Catal. A Gen. **449** (2012) 31–46. https://doi.org/10.1016/j.apcata.2012.09.039.

[13] P. Roy, S. Berger, P. Schmuki, TiO_2 nanotubes: Synthesis and applications, Angew. Chemie - Int. Ed. **50** (2011) 2904–2939. https://doi.org/10.1002/anie.201001374.

[14] E.C.R. Lopez, J.D. Ocon, J.V.D. Perez, Synthesis of silver-doped titanium dioxide nanotubes by single-step anodization for enhanced photodegradation of acid orange **52**, in: Mater. Sci. Forum, Trans Tech Publications Ltd, 2019: pp. 149–153. https://doi.org/10.4028/www.scientific.net/MSF.950.149.

[15] H. Ullah, A. Ur Rahman, E. Leonetti Aragão, F. Fróis Alves Barbosa, K. Gabriel Ramisch Pergher, R. Giulian, H. Coelho Júnior, R. Luis Sommer, S. Khan, Homogeneous V incorporation via single-step anodization: Structural doping or heterostructure formation?, Appl. Surf. Sci. **556** (2021). https://doi.org/10.1016/j.apsusc.2021.149694.

[16] S.E. Jun, J.K. Lee, H.W. Jang, Two-dimensional materials for photoelectrochemical water splitting, Energy Adv. **2** (2023) 34–53. https://doi.org/10.1039/d2ya00231k.

[17] C. Li, Q. Cao, F. Wang, Y. Xiao, Y. Li, J.J. Delaunay, H. Zhu, Engineering graphene and TMDs based van der Waals heterostructures for photovoltaic and photoelectrochemical solar energy conversion, Chem. Soc. Rev. **47** (2018) 4981–5037. https://doi.org/10.1039/c8cs00067k.

[18] C.J. Chen, V. Veeramani, Y.H. Wu, A. Jena, L.C. Yin, H. Chang, S.F. Hu, R.S. Liu, Phosphorous-doped molybdenum disulfide anchored on silicon as an efficient catalyst for photoelectrochemical hydrogen generation, Appl. Catal. B Environ. **263** (2020). https://doi.org/10.1016/j.apcatb.2019.118259.

[19] H. Chen, S. Wang, J. Wu, X. Zhang, J. Zhang, M. Lyu, B. Luo, G. Qian, L. Wang, Identifying dual functions of rGO in a $BiVO_4$/rGO/NiFe-layered double hydroxide photoanode for efficient photoelectrochemical water splitting, J. Mater. Chem. A. **8** (2020) 13231–13240. https://doi.org/10.1039/d0ta04572a.

[20] B. Zhou, X. Kong, S. Vanka, S. Chu, P. Ghamari, Y. Wang, N. Pant, I. Shih, H. Guo, Z. Mi, Gallium nitride nanowire as a linker of molybdenum sulfides and silicon for photoelectrocatalytic water splitting, Nat. Commun. **9** (2018). https://doi.org/10.1038/s41467-018-06140-1.

[21] C.C. Chung, H. Yeh, P.H. Wu, C.C. Lin, C.S. Li, T.T. Yeh, Y. Chou, C.Y. Wei, C.Y. Wen, Y.C. Chou, C.W. Luo, C.I. Wu, M.Y. Li, L.J. Li, W.H. Chang, C.W. Chen, Atomic-Layer Controlled Interfacial Band Engineering at Two-Dimensional Layered $PtSe_2$/Si Heterojunctions for Efficient Photoelectrochemical Hydrogen Production, ACS Nano. **15** (2021) 4627–4635. https://doi.org/10.1021/acsnano.0c08970.

[22] K.C. Kwon, S. Choi, K. Hong, D.M. Andoshe, J.M. Suh, C. Kim, K.S. Choi, J.H. Oh, S.Y. Kim, H.W. Jang, Tungsten disulfide thin film/p-type Si heterojunction photocathode for efficient photochemical hydrogen production, MRS Commun. **7** (2017) 272–279. https://doi.org/10.1557/mrc.2017.37.

[23] P. Gnanasekar, D. Periyanagounder, P. Varadhan, J.H. He, J. Kulandaivel, Highly Efficient and Stable Photoelectrochemical Hydrogen Evolution with 2D-NbS2/Si Nanowire Heterojunction, ACS Appl. Mater. Interfaces. **11** (2019) 44179–44185. https://doi.org/10.1021/acsami.9b14713.

[24] L. Ju, J. Qin, L. Shi, G. Yang, J. Zhang, L. Sun, Rolling the wsse bilayer into

double-walled nanotube for the enhanced photocatalytic water-splitting performance, Nanomaterials. **11** (2021) 1–11.

[25] H. Ullah, I. Shehzadi, A.U. Rahman, M.W. Iqbal, S. Khan, Room Temperature Ferromagnetism in Hydrogenated Janus CrSSe Monolayer Using Quantum Monte Carlo Simulation, Cryst. Growth Des. **23** (2023) 511–523. https://doi.org/10.1021/acs.cgd.2c01157.

[26] R.M. Navarro, M.C. Alvarez-Galván, J.A. Villoria De La Mano, S.M. Al-Zahrani, J.L.G. Fierro, A framework for visible-light water splitting, Energy Environ. Sci. **3** (2010) 1865–1882. https://doi.org/10.1039/c001123a.

[27] Photoelectro-chemical Hydrogen Production Roel van de Krol Michael Grätzel, n.d. http://www.springer.com/series/5915.

[28] K. Sivula, F. Le Formal, M. Grätzel, WO_3-Fe_2O_3 photoanodes for water splitting: A host scaffold, guest absorber approach, Chem. Mater. **21** (2009) 2862–2867. https://doi.org/10.1021/cm900565a.

[29] C.M. Fang, E. Orhan, G.A. De Wijs, H.T. Hintzen, R.A. De Groot, R. Marchand, J.Y. Saillard, G. De With, The electronic structure of tantalum (oxy)nitrides TaON and Ta_3N_5, J. Mater. Chem. **11** (2001) 1248–1252. https://doi.org/10.1039/b005751g.

[30] P.Y. Yu, M. Cardona, Fundamentals of Semiconductors: Physics and Materials Properties, 4th Edition, n.d.

[31] E. Nurlaela, Development of Ta_3N_5 as an Efficient Visible Light-responsive Photocatalyst for Water Oxidation, 2015.

[32] Introduction to Solid State Physics Charles Kittel, 2005.

[33] S. Ono, M. Saito, H. Asoh, Self-ordering of anodic porous alumina induced by local current concentration: Burning, Electrochem. Solid-State Lett. **7** (2004). https://doi.org/10.1149/1.1738553.

[34] O. Madelung, U. Rössler, M. Schulz, eds., Germanium (Ge), intrinsic carrier concentration: Datasheet from Landolt-Börnstein - Group III Condensed Matter · Volume 41A1β: "Group IV Elements, IV-IV and III-V Compounds. Part b - Electronic, Transport, Optical and Other Properties" in SpringerMaterials

(https://doi.org/10.1007/10832182_503).

[35] D.A. Neamen, Semiconductor physics and devices : basic principles, McGraw-Hill, 2012.

[36] C. Ampelli, C. Genovese, G. Centi, R. Passalacqua, S. Perathoner, Nanoscale Engineering in the Development of Photoelectrocatalytic Cells for Producing Solar Fuels, Top. Catal. **59** (2016) 757–771. https://doi.org/10.1007/s11244-016-0547-5.

[37] J. Gandia, M. Pujadas, P. Salvador, Elsevier Sequoia S.A., Lausanne-Printed in The Netherlands ELECTROLYTE ELECI'ROREFLECTANC EASY AND RELIABLE FLAT-BAND POTENTIAL MEASUREMFNTS, 1988.

[38] L.J. Minggu, W.R. Wan Daud, M.B. Kassim, An overview of photocells and photoreactors for photoelectrochemical water splitting, Int. J. Hydrogen Energy. **35** (2010) 5233–5244. https://doi.org/10.1016/j.ijhydene.2010.02.133.

[39] X. Shi, L. Cai, M. Ma, X. Zheng, J.H. Park, General Characterization Methods for Photoelectrochemical Cells for Solar Water Splitting, ChemSusChem. **8** (2015) 3192–3203. https://doi.org/10.1002/cssc.201500075.

[40] J. Brillet, J.H. Yum, M. Cornuz, T. Hisatomi, R. Solarska, J. Augustynski, M. Graetzel, K. Sivula, Highly efficient water splitting by a dual-absorber tandem cell, Nat. Photonics. **6** (2012) 824–828.

[41] W.J. Chun, A. Ishikawa, H. Fujisawa, T. Takata, J.N. Kondo, M. Hara, M. Kawai, Y. Matsumoto, K. Domen, Conduction and valence band positions of Ta_2O_5, TaOn, and Ta_3N_5 by UPS and electrochemical methods, J. Phys. Chem. B. 107 (2003) 1798–1803. https://doi.org/10.1021/jp027593f.

[42] Z. Su, S. Grigorescu, L. Wang, K. Lee, P. Schmuki, Fast fabrication of Ta_2O_5 nanotube arrays and their conversion to Ta_3N_5 for efficient solar driven water splitting, Electrochem. Commun. **50** (2015) 15–19. https://doi.org/10.1016/j.elecom.2014.10.017.

[43] Y. Xia, P. Yang, Y. Sun, Y. Wu, B. Mayers, B. Gates, Y. Yin, F. Kim, H. Yan, One-dimensional nanostructures: Synthesis, characterization, and applications, Adv. Mater. 15 (2003) 353–389. https://doi.org/10.1002/adma.200390087.

[44] M.C. Nevárez-Martínez, P. Mazierski, M.P. Kobylański, G. Szczepańska, G. Trykowski, A. Malankowska, M. Kozak, P.J. Espinoza-Montero, A. Zaleska-Medynska, Growth, structure, and photocatalytic properties of hierarchical V_2O_5-TiO_2 nanotube arrays obtained from the one-step anodic oxidation of Ti-V alloys, Molecules. 22 (2017). https://doi.org/10.3390/molecules22040580.

[45] X. Zou, X. Han, C. Wang, Y. Zhao, C. Du, B. Shan, Carrier engineering of Zr-doped Ta_3N_5 film as an efficient photoanode for solar water splitting, Sustain. Energy Fuels. **5** (2021) 2877–2883. https://doi.org/10.1039/d1se00640a.

[46] S. Grigorescu, B. Bärhausen, L. Wang, A. Mazare, J.E. Yoo, R. Hahn, P. Schmuki, Tungsten doping of Ta_3N_5-nanotubes for band gap narrowing and enhanced photoelectrochemical water splitting efficiency, Electrochem. Commun. **51** (2015) 85–88. https://doi.org/10.1016/j.elecom.2014.12.019.

[47] J. Venturini, F. Bonatto, W.C. Guaglianoni, T. Lemes, S. Arcaro, A.K. Alves, C.P. Bergmann, Cobalt-doped titanium oxide nanotubes grown via one-step anodization for water splitting applications, Appl. Surf. Sci. **464** (2019) 351–359. https://doi.org/10.1016/j.apsusc.2018.09.093.

[48] J. Wang, Y. Jiang, A. Ma, J. Jiang, J. Chen, M. Li, J. Feng, Z. Li, Z. Zou, Charge compensation doping to improve the photocatalytic and photoelectrochemical activities of Ta_3N_5: A theoretical study, Appl. Catal. B Environ. **244** (2019) 502–510. https://doi.org/10.1016/j.apcatb.2018.11.076.

[49] L. Yuliati, J.H. Yang, X. Wang, K. Maeda, T. Takata, M. Antonietti, K. Domen, Highly active tantalum(v) nitride nanoparticles prepared from a mesoporous carbon nitride template for photocatalytic hydrogen evolution under visible light irradiation, J. Mater. Chem. **20** (2010) 4295–4298.

[50] Y. Fukasawa, K. Takanabe, A. Shimojima, M. Antonietti, K. Domen, T. Okubo, Synthesis of ordered porous graphitic-C3N4 and regularly arranged Ta3N5 nanoparticles by using self-assembled silica nanospheres as a primary template, Chem. - An Asian J. **6** (2011) 103–109. https://doi.org/10.1002/asia.201000523.

[51] T. Hisatomi, M. Otani, K. Nakajima, K. Teramura, Y. Kako, D. Lu, T. Takata, J.N. Kondo, K. Domen, Preparation of crystallized mesoporous Ta_3N_5 assisted by chemical vapor deposition of tetramethyl orthosilicate, Chem. Mater. **22**

(2010) 3854–3861. https://doi.org/10.1021/cm903583f.

[52] Z. Wang, J. Wang, J. Hou, K. Huang, S. Jiao, H. Zhu, Facile synthesis of efficient photocatalytic tantalum nitride nanoparticles, Mater. Res. Bull. **47** (2012) 3605–3611. https://doi.org/10.1016/j.materresbull.2012.06.054.

[53] J. Eichhorn, S.P. Lechner, C.M. Jiang, G. Folchi Heunecke, F. Munnik, I.D. Sharp, Indirect bandgap, optoelectronic properties, and photoelectrochemical characteristics of high-purity Ta_3N_5 photoelectrodes, J. Mater. Chem. A. **9** (2021) 20653–20663. https://doi.org/10.1039/d1ta05282a.

[54] S.S.K. Ma, T. Hisatomi, K. Maeda, Y. Moriya, K. Domen, Enhanced water oxidation on Ta_3N_5 photocatalysts by modification with alkaline metal salts, J. Am. Chem. Soc. **134** (2012) 19993–19996. https://doi.org/10.1021/ja3095747.

[55] S. Khan, M.J.M. Zapata, D.L. Baptista, R. V. Gonçalves, J.A. Fernandes, J. Dupont, M.J.L. Santos, S.R. Teixeira, Effect of Oxygen Content on the Photoelectrochemical Activity of Crystallographically Preferred Oriented Porous Ta3N5 Nanotubes, J. Phys. Chem. C. **119** (2015) 19906–19914. https://doi.org/10.1021/acs.jpcc.5b05475.

[56] B.A. Pinaud, P.C.K. Vesborg, T.F. Jaramillo, Effect of film morphology and thickness on charge transport in Ta_3N_5/Ta photoanodes for solar water splitting, J. Phys. Chem. C. **116** (2012) 15918–15924. https://doi.org/10.1021/jp3041742.

[57] L. Wang, F. Dionigi, N.T. Nguyen, R. Kirchgeorg, M. Gliech, S. Grigorescu, P. Strasser, P. Schmuki, Tantalum nitride nanorod arrays: Introducing Ni-Fe layered double hydroxides as a cocatalyst strongly stabilizing photoanodes in water splitting, Chem. Mater. **27** (2015) 2360–2366. https://doi.org/10.1021/cm503887t.

[58] Q.H. Funk, H. Bohland, Zur Darstellung von Metallnitriden aus Ammoniumfluorometallaten und Ammoniak, 1924.

[59] K. Hieber, STRUCTURAL AND ELECTRICAL PROPERTIES OF Ta AND Ta NITRIDES DEPOSITED BY CHEMICAL VAPOUR DEPOSITION, 1974.

[60] E. Nurlaela, M. Harb, S. Del Gobbo, M. Vashishta, K. Takanabe, Combined experimental and theoretical assessments of the lattice dynamics and

optoelectronics of TaON and Ta_3N_5, J. Solid State Chem. **229** (2015) 219–227. https://doi.org/10.1016/j.jssc.2015.06.029.

[61] H. Hajibabaei, O. Zandi, T.W. Hamann, Tantalum nitride films integrated with transparent conductive oxide substrates: Via atomic layer deposition for photoelectrochemical water splitting, Chem. Sci. **7** (2016) 6760–6767. https://doi.org/10.1039/c6sc02116f.

[62] J. Seo, T. Takata, M. Nakabayashi, T. Hisatomi, N. Shibata, T. Minegishi, K. Domen, Mg-Zr cosubstituted Ta_3N_5 photoanode for lower-onset-potential solar-driven photoelectrochemical water splitting, J. Am. Chem. Soc. **137** (2015) 12780–12783. https://doi.org/10.1021/jacs.5b08329.

[63] Y. Cong, H.S. Park, S. Wang, H.X. Dang, F.R.F. Fan, C.B. Mullins, A.J. Bard, Synthesis of Ta_3N_5 nanotube arrays modified with electrocatalysts for photoelectrochemical water oxidation, J. Phys. Chem. C. **116** (2012) 14541–14550. https://doi.org/10.1021/jp304340a.

[64] J. Zhang, M. Deng, F. Ren, Y. Wu, Y. Wang, Effects of Mo/W codoping on the visible-light photocatalytic activity of monoclinic $BiVO_4$ within the GGA + U framework, RSC Adv. **6** (2016) 12290–12297. https://doi.org/10.1039/c5ra22659g.

[65] J.P. Perdew, K. Burke, M. Ernzerhof, Generalized Gradient Approximation Made Simple, 1996.

[66] D.S. Sholl, J.A. Steckel, DENSITY FUNCTIONAL THEORY A Practical Introduction, n.d.

[67] J.P. Perdew, W. Yue, Accurate and simple density functional for the electronic exchange energy: Generalized gradient approximation, 1986.

[68] W. Kohn, L.J. Sham, PHYSICAL REVIEW Self-Consistent Equations Including Exchange and Correlation Effects*, n.d.

[69] D. Vanderbilt, Rapid Communications Soft self-consistent pseudopotentials in a generalized eigenvalue formalism, n.d.

[70] B.J. Ausrrn, ~ V Hernz, A.L.J. Shamt, General Theory of Pseutlopotentials, 1962.

[71] T. Starklofp, J.D. Joannopoulos~, Local psentiopotential theory for transition metals, 1977.

[72] D. Vanderbilt, Optimally smooth norm-conserving pseudopotentials, 1985.

[73] N. Troullier, J.L. Martins, EfFicient pseudopotentials for plane-wave calculations-II, 1991.

[74] S. Goedecker, M. Teter, J. Hutter, Separable dual-space Gaussian pseudopotentials, 1996.

[75] P. Giannozzi, S. Baroni, N. Bonini, M. Calandra, R. Car, C. Cavazzoni, D. Ceresoli, G.L. Chiarotti, M. Cococcioni, I. Dabo, A. Dal Corso, S. De Gironcoli, S. Fabris, G. Fratesi, R. Gebauer, U. Gerstmann, C. Gougoussis, A. Kokalj, M. Lazzeri, L. Martin-Samos, N. Marzari, F. Mauri, R. Mazzarello, S. Paolini, A. Pasquarello, L. Paulatto, C. Sbraccia, S. Scandolo, G. Sclauzero, A.P. Seitsonen, A. Smogunov, P. Umari, R.M. Wentzcovitch, QUANTUM ESPRESSO: A modular and open-source software project for quantum simulations of materials, J. Phys. Condens. Matter. **21** (2009). https://doi.org/10.1088/0953-8984/21/39/395502.

[76] S.A. Tolba, K.M. Gameel, B.A. Ali, H.A. Almossalami, N.K. Allam, The DFT+U: Approaches, Accuracy, and Applications, in: Density Funct. Calc. - Recent Progresses Theory Appl., InTech, 2018. https://doi.org/10.5772/intechopen.72020.

[77] H. Jouypazadeh, H. Farrokhpour, M.M. Momeni, A DFT study of the water-splitting photocatalytic properties of pristine, Nb-doped, and V-doped Ta3N5 monolayer nanosheets, Surfaces and Interfaces. **26** (2021). https://doi.org/10.1016/j.surfin.2021.101379.

[78] P. Migowski, H. Wender, D. Eberhardt, D.E. Weibel, C. Sonaglio, M.J.M. Zapata, J. Dupont, A.F. Feil, S.R. Teixeira, Ta_2O_5 Nanotubes Obtained by Anodization: E ff ect of Thermal Treatment on the Photocatalytic Activity for Hydrogen Production, (2012).

[79] N.K. Allam, X.J. Feng, C.A. Grimes, Self-assembled fabrication of vertically oriented Ta_2O_5 nanotube arrays, and membranes thereof, by one-step tantalum

anodization, Chem. Mater. 20 (2008) 6477–6481. https://doi.org/10.1021/cm801472y.

[80] T. Wen, H. Tan, S. Chen, P. He, S. Yang, C. Deng, S. Liu, Growth behavior of tantalum oxide nanotubes during constant current anodization, Electrochem. Commun. **128** (2021). https://doi.org/10.1016/j.elecom.2021.107073.

[81] Y. Wu, G. Ceder, First principles study on Ta_3N_5:$Ti_3O_3N_2$ solid solution as a water-splitting photocatalyst, J. Phys. Chem. C. **117** (2013) 24710–24715. https://doi.org/10.1021/jp407911g.

[82] Y. Hou, J. Zhang, Q. Yang, C. Wang, H. Tang, S. Yan, Z. Zou, ALD-grown oxide protective layers on Ta_3N_5-Cu_2O n-p nanoarray heterojunction for improved photoelectrochemical water splitting, Appl. Phys. Lett. **117** (2020). https://doi.org/10.1063/5.0027906.

[83] H. Jouypazadeh, H. Farrokhpour, M.M. Momeni, Theoretical investigation of the water splitting photocatalytic properties of pristine, Nb and V doped, and Nb-V co-doped (1 1 1) TaON nanosheets, Appl. Surf. Sci. **541** (2021). https://doi.org/10.1016/j.apsusc.2020.148572.

[84] M. Harb, P. Sautet, E. Nurlaela, P. Raybaud, L. Cavallo, K. Domen, J.M. Basset, K. Takanabe, Tuning the properties of visible-light-responsive tantalum (oxy)nitride photocatalysts by non-stoichiometric compositions: A first-principles viewpoint, Phys. Chem. Chem. Phys. **16** (2014) 20548–20560. https://doi.org/10.1039/c4cp03594a.

[85] J. Wang, T. Fang, L. Zhang, J. Feng, Z. Li, Z. Zou, Effects of oxygen doping on optical band gap and band edge positions of Ta_3N_5 photocatalyst: A GGA + U calculation, J. Catal. **309** (2014) 291–299.

[86] M. Cococcioni, S. De Gironcoli, Linear response approach to the calculation of the effective interaction parameters in the LDA+U method, Phys. Rev. B - Condens. Matter Mater. Phys. **71** (2005).

[87] V.N. Jafarova, G.S. Orudzhev, Structural and electronic properties of ZnO: A first-principles density-functional theory study within LDA(GGA) and LDA(GGA)+U methods, Solid State Commun. **325** (2021).

https://doi.org/10.1016/j.ssc.2020.114166.

[88] R. Tesch, P.M. Kowalski, Hubbard U parameters for transition metals from first principles, Phys. Rev. B. **105** (2022).

[89] A.H. Reshak, Electronic structure and dispersion of optical function of tantalum nitride as a visible light photo-catalyst, Comput. Mater. Sci. **89** (2014) 45–51. https://doi.org/10.1016/j.commatsci.2014.03.035.

[90] H.A. El-Sayed, V.I. Birss, Controlled interconversion of nanoarray of Ta dimples and high aspect ratio Ta oxide nanotubes, Nano Lett. **9** (2009) 1350–1355. https://doi.org/10.1021/nl803010v.

[91] M.A. Khan, A. Kashyap, A.K. Solanki, T. Nautiyal, S. Auluck, Interband optical properties of Ni_3A1, 1993.

[92] R. Khan, K. Ur Rahman, Q. Zhang, A.U. Rahman, S. Azam, A. Dahshan, The effect of substitutional doping of Yb^{2+}on structural, electronic, and optical properties of $CsCaX_3$(X: Cl, Br, I) phosphors: A first-principles study, J. Phys. Condens. Matter. **34** (2022). https://doi.org/10.1088/1361-648X/ac3583.

[93] M. Fox, G.F. Bertsch, *Optical Properties of Solids*, Am. J. Phys. **70** (2002) 1269–1270. https://doi.org/10.1119/1.1691372.

[94] M. Fox, G.F. Bertsch, D.J. Griffiths, Optical Properties of Solids, **1269** (2011). https://doi.org/10.1119/1.1691372.

[95] F. Kong, G. Jiang, Nonlinear optical response of wurtzite ZnO from first principles, Phys. B Condens. Matter. **404** (2009) 2340–2344. https://doi.org/10.1016/j.physb.2009.04.041.

[96] P. Rani, G.S. Dubey, V.K. Jindal, DFT study of optical properties of pure and doped graphene, Phys. E Low-Dimensional Syst. Nanostructures. **62** (2014) 28–35. https://doi.org/10.1016/j.physe.2014.04.010.

[97] Electronic and Photonic Materials Kasap Capper Editors 2nd Edition, n.d.

[98] P.D. Bhuyan, D. Singh, S. Kansara, P. Yadav, S.K. Gupta, Y. Sonvane, S.K. Rout, E. Sinha, Experimental and theoretical analysis of electronic and optical properties of MgWO4, J. Mater. Sci. **52** (2017) 4934–4943.

https://doi.org/10.1007/s10853-016-0730-x.

[99] J.M. Morbec, I. Narkeviciute, T.F. Jaramillo, G. Galli, Optoelectronic properties of Ta3 N5: A joint theoretical and experimental study, Phys. Rev. B - Condens. Matter Mater. Phys. **90** (2014). https://doi.org/10.1103/PhysRevB.90.155204.

[100] I. V. Kityk, New approach for calculation of the GaxAl1-xN solid-state alloys, Comput. Mater. Sci. **27** (2003) 342–350. https://doi.org/10.1016/S0927-0256(03)00039-9.

[101] O. Fursenko, J. Bauer, G. Lupina, P. Dudek, M. Lukosius, C. Wenger, P. Zaumseil, Optical properties and band gap characterization of high dielectric constant oxides, Thin Solid Films. **520** (2012) 4532–4535. https://doi.org/10.1016/j.tsf.2011.10.195.

[102] A.B. Murphy, Band-gap determination from diffuse reflectance measurements of semiconductor films, and application to photoelectrochemical water-splitting, Sol. Energy Mater. Sol. Cells. **91** (2007) 1326–1337. https://doi.org/10.1016/j.solmat.2007.05.005.

[103] K. Noh, K.S. Brammer, H. Kim, S.Y. Jung, T.Y. Seong, S. Jin, Highly self-assembled nanotubular aluminum oxide by hard anodization, J. Mater. Res. **26** (2011) 186–193. https://doi.org/10.1557/jmr.2010.6.

[104] V.A. Online, S. Khan, M. Jose, L. Santos, improved structural and photoelectrochemical, (2015) 103284–103291.

[105] P. Krisna Das, M. Arunachalam, K.R. Subhash, Y.J. Seo, K.S. Ahn, J.S. Ha, S.H. Kang, Nanoporous Ta_3N_5: Via electrochemical anodization followed by nitridation for solar water oxidation, Dalt. Trans. **49** (2020) 15023–15033. https://doi.org/10.1039/d0dt03056b.

[106] Y.W. Kim, S. Cha, I. Kwak, I.S. Kwon, K. Park, C.S. Jung, E.H. Cha, J. Park, Surface-Modified Ta3N5 Nanocrystals with Boron for Enhanced Visible-Light-Driven Photoelectrochemical Water Splitting, ACS Appl. Mater. Interfaces. **9** (2017) 36715–36722. https://doi.org/10.1021/acsami.7b09040.

Appendix

Published Articles

Article No: 1

Applied Surface Science 556 (2021) 149694

Contents lists available at ScienceDirect

Applied Surface Science

journal homepage: www.elsevier.com/locate/apsusc

Full Length Article

Homogeneous V incorporation via single-step anodization: Structural doping or heterostructure formation?

Hameed Ullah [a], Altaf Ur Rahman [b], Erhon Leonetti Aragão [a], Fernanda Fróis Alves Barbosa [a], Kevin Gabriel Ramisch Pergher [a], Raquel Giulian [c], Horácio Coelho Júnior [d], Rubem Luis Sommer [d], Sherdil Khan [a,*]

[a] Laboratório de Filmes Finos e Fabricação de Nanoestruturas (L3FNano), Institute of Physics, PPGFIS and PPGCIMAT, Federal University of Rio Grande do Sul (UFRGS), Campus do Vale: Av. Bento Gonçalves, 9500 - Agronomia, Porto Alegre-RS, Brazil
[b] Department of Physics, Riphah Institute of Computing & Applied Sciences, Riphah International University, 13 km Raiwind Rd, Chamru Pur, Lahore, Pakistan
[c] Laboratório de Implantação Iônica, Institute of Physics, PPGFIS and PPGCIMAT Federal University of Rio Grande do Sul (UFRGS), Campus do Vale: Av. Bento Gonçalves, 9500 - Agronomia, Porto Alegre-RS, Brazil
[d] Centro Brasileiro de Pesquisas Físicas (CBPF), Rua Dr. Xavier Sigaud 150, Urca, Rio de Janeiro-RJ, Brazil

ARTICLE INFO

Keywords:
Single-step anodization
Foreign element insertion
Heterostructure
Photoelectrochemical
Photolysis
Density functional theory
Energy-band alignment

ABSTRACT

Two distinct-phenomena were reported for anodic elemental-incorporation; structural-doping/heterostructure formation. Herein, by adding V for the first time in TiO_2-nanotubes via anodization; the foreign elemental incorporation is peered. The bandgap (3.2 eV), flat band (0.07 V_{RHE}) and valence band (VB) positions of V-incorporated anatase-TiO_2 nanotubes remained invariant which ruled out structural doping of TiO_2. The first-step in anodization is Ti-oxidation that occurs momentarily; thereby, the oxidation/dissolution dominancy of anodization in later stages impeded V-structural doping even for varying times (1–24 h) and voltages (6–60 V) and thus a small fraction of V_2O_5 was observed in surface and microscopic studies. Density functional theory realistic simulations revealed TiO_2/V_2O_5 forms commensurate-heterostructure at common lattice constants with charge transfer from TiO_2 to V_2O_5 at the heterostructure interface; exhibiting type-II band-alignment having CB from V_2O_5 and VB from TiO_2 with decreasing bandgap. In photoelectrochemical-setup, the photogenerated electron transfer from V_2O_5 to the heterostructure interface was suppressed due to barrier-height which decreased photocurrent for TiO_2/V_2O_5 (52 $\mu A/cm^2$) as compared to pure-TiO_2 (140 $\mu A/cm^2$) at ~1.0 V_{RHE}. Contrarily, in photolysis, improved light absorption and facile carrier migration from TiO_2/V_2O_5 resulted in better photodegradation activity of methylene-blue. We unlocked anodization is ineffective for structural-doping, indeed it results in uniform low-content elemental incorporation forming oxides heterostructure.

Article No: 2

CRYSTAL GROWTH & DESIGN

pubs.acs.org/crystal Article

Room Temperature Ferromagnetism in Hydrogenated Janus CrSSe Monolayer Using Quantum Monte Carlo Simulation

Published as part of a Crystal Growth and Design virtual special issue on Molecular Magnets and Switchable Magnetic Materials

Hameed Ullah, Iram Shehzadi, Altaf Ur Rahman,* Muhammad Waqas Iqbal, and Sherdil Khan*

Cite This: *Cryst. Growth Des.* 2023, 23, 511−523 Read Online

ACCESS | Metrics & More | Article Recommendations | Supporting Information

ABSTRACT: Here, using first-principles calculations based on density-functional theory, we propose a novel member of the two-dimensional (2D) transitional metal dichalcogenide family known as a Janus CrSSe monolayer (denoted as CrSSe-ML). The 2D CrSSe-ML has a hexagonal crystal structure. The calculated phonon band structure suggests Janus CrSSe-ML is dynamically stable, and formation energy indicates thermodynamic stability. At the equilibrium lattice constant, it is reported that 2D Janus CrSSe-ML is a non-magnetic semiconductor with a direct bandgap of 0.93 eV (K−K). We found that compressive biaxial strain induces no local magnetic moment, while in contrast the tensile biaxial strain of 12% induces a magnetic moment of 2 μ_B and half-metallicity which is robust up to 20%. Furthermore, we studied the ferromagnetic (FM) and antiferromagnetic (AFM) coupling between Cr atoms in CrSSe-ML and found that the FM state is favorable over AFM by the amount of energy of 0.007 meV, which is less than 0.03 eV, so no room-temperature ferromagnetism is possible. At the end, we added the H atom at the most preferable Se top-site in a Janus CrSSe-ML and found that hydrogenated Janus CrSSe-ML is magnetic and half-metallic at the equilibrium lattice constant. We further studied FM and AFM calculation by considering fully hydrogenated 4 × 4 × 1 supercell of a Janus CrSSe-ML. We used quantum Monte Carlo simulations (MC) to estimate the Curie temperature (T_c) of hydrogenated CrSSe-ML under normal conditions. The calculated value of T_c is 553.96 K using the quantum MC simulations. Our calculations predicted that the 2D Janus CrSSe-ML material is a promising candidate for spintronic device applications above room temperature.

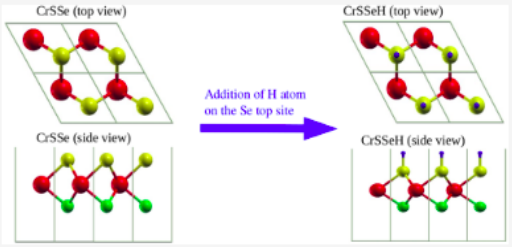

Article No: 3

Journal of Magnetism and Magnetic Materials 515 (2020) 167212

Contents lists available at ScienceDirect

Journal of Magnetism and Magnetic Materials

journal homepage: www.elsevier.com/locate/jmmm

Research articles

Functionalization of monolayer-CdS by metal and non-metal elemental substitution: First-principle understanding

Altaf Ur Rahman[a,b,*], Hameed Ullah[c], Manish Verma[d], Sherdil Khan[c,*]

[a] Department of Physics, Riphah Institute of Computing & Applied Sciences, Riphah International University, 13 km Raiwind Rd, Chamru Pur Lahore, Pakistan
[b] Department of Physics, International Islamic University, Islamabad 44000, Pakistan
[c] Institute of Physics, UFRGS, Av Bento Goncalves 9500, Porto Alegre, RS, Brazil
[d] Department of Physics, University of Duisburg-Essen, Germany

ARTICLE INFO

Keywords:
Metal Mono-chalcogenides
Electronic and magnetic properties
Substitutional doping
Density functional theory
Generalized gradient approximation

ABSTRACT

Herein, monolayer-CdS substitutional elemental doping with metal (X; Fe) and non-metal (X; H, N, F) atoms has been investigated by the first-principle calculations. In non-magnetic monolayer-CdS, magnetism can be induced by metal and non-metal atom substitution at possible dopant sites except for F_S (F doped at the chalcogen site). In particular, Fe doping at Cd-Site (Fe_{Cd}) results in a maximum magnetic moment of 4.0 μ_B, and half-metallic character with a small dispersion at Γ point. Among all the substitutional dopants at the hole-site, F_h is ferromagnetic, being most energetically favorable under both atomic and molecular phases. The H_h in monolayer-CdS retained the semiconducting nature with reduced band gaps for spin-up and spin-down channels. N_h exhibits half-metallic character with a small dispersion of 0.13 eV at K-Γ point. The F_h and Fe_h show metallic behavior. To determine the exchange-field strength ferromagnetic (FM) and anti-ferromagnetic (AFM) coupling between the two dopants at far positions (1, 3) and near positions (1, 2) have been considered. The effect of dopants concentration on FM and AFM coupling were also investigated. It was found N_S ($\Theta = 4$ %) at near positions (1, 2) shows FM state with Curie temperature (T_c) of 106 K. As the biaxial strain of −5 % is applied the maximum FM state was achieved withT_c of 164 K. The functionalization of monolayer-CdS with the proposed elements provided in this work can help tailoring two-dimensional (2D) materials applied in spintronics and electronics devices.

Article No: 4

International Journal of Biological Macromolecules 242 (2023) 124815

Contents lists available at ScienceDirect

International Journal of Biological Macromolecules

journal homepage: www.elsevier.com/locate/ijbiomac

In-vitro synergistic microbicidal and catalytic evaluation of polyvinylpyrrolidone/chitosan doped tungsten trioxide nanoplates with evidential in-silico analysis

Ehtisham Umar [a], Ali Haider [b,*], Iram Shahzadi [c], Anwar Ul-Hamid [d], Hameed Ullah [e], Sherdil Khan [e], Muhammad Ikram [a,*]

[a] Solar Cell Applications Research Lab, Department of Physics, Government College University Lahore, Lahore 54000, Punjab, Pakistan
[b] Department of Clinical Sciences, Faculty of Veterinary and Animal Sciences, Muhammad Nawaz Shareef University of Agriculture (MNSUA), Multan 66000, Punjab, Pakistan
[c] Punjab University College of Pharmacy, University of the Punjab, Allama Iqbal Campus, Lahore 54000, Pakistan
[d] Core Research Facilities, Research Institute, King Fahd University of Petroleum & Minerals, Dhahran 31261, Saudi Arabia
[e] Laboratory of Nanomaterials for Renewable Energy and Artificial Photosynthesis (NanoREAP), Institute of Physics, UFRGS, 91509-900 Porto Alegre, Rio Grande do Sul, Brazil

ARTICLE INFO

Keywords:
WO_3 nanoplates
Molecular docking analysis
Raman and XPS

ABSTRACT

In this research, hydrothermally synthesized tungsten trioxide (WO_3) nanocomposites doped polyvinylpyrrolidone (PVP) and chitosan (CS) were studied. Various concentrations (3, 6, and 9 wt%) of PVP were doped into a fixed amount of binary system (CS-WO_3) nanocomposites. PVP/CS polymers showed attractive attention because of their different structure, functionality, and architecture control as dopant to WO_3. The PVP/CS encapsulates the WO_3 (ternary composite), which controls crystallite size (band gap reduction), rapidly overcomes the recombination electron-hole pairs issues, and generates the active sites, resulting in improved catalytic and antimicrobial activity. The synthesized nanocomposites revealed significant catalytic efficiency and methylene blue (MB) dye depletion of 99.9 % in the presence of reducing agent ($NaBH_4$) in neutral and acidic media. Antimicrobial effectiveness of produced nanostructures towards *Escherichia coli* (*E. coli*) pathogen at low and high concentrations were investigated by Vernier caliper in mm. Furthermore, to their microbicidal action, docking experiments of CS-doped WO_3 and PVP/CS-doped WO_3 nanostructures for DHFR and FabI of *Escherichia coli* suggested blockage of aforesaid enzymes as the plausible pathway.

Article No: 5

Surfaces and Interfaces 38 (2023) 102804

Contents lists available at ScienceDirect

Surfaces and Interfaces

journal homepage: www.sciencedirect.com/journal/surfaces-and-interfaces

Efficient dye degradation in the presence of reducing agent and bactericidal behavior with in silico molecular docking of z-scheme P3HT/g-C_3N_4 doped CuO heterojunction

Hafsa Saeed [a], Muhammad Ikram [a,*], Ali Haider [b], Sadia Naz [c], Anwar Ul-Hamid [d], Walid Nabgan [e,*], Junaid Haider [c], SM Ibrahim [f], Hameed Ullah [g], Sherdil Khan [g]

[a] Solar Cell Applications Research Lab, Department of Physics, Government College, University Lahore, Lahore, 54000, Punjab, Pakistan
[b] Department of Clinical Sciences, Faculty of Veterinary and Animal Sciences, Muhammad Nawaz Shareef, University of Agriculture, 66000, Multan, Punjab, Pakistan
[c] Tianjin Institute of Industrial Biotechnology, Chinese Academy of Sciences, Tianjin, 300308, China
[d] Core Research Facilities, King Fahd University of Petroleum & Minerals, Dhahran, 31261, Saudi Arabia
[e] Departamentd'Enginyeria Química, Universitat Rovira i Virgili, Av Països Catalans 26, 43007, Tarragona, Spain
[f] Department of Chemistry, Government College University Faisalabad, Sahiwal campus, Pakpattan Chowk, 57000, Pakistan
[g] Laboratory of Nanomaterials for Renewable Energy and Artificial Photosynthesis (NanoREAP), Institute of Physics, UFRGS, 91509-900 Porto Alegre, Rio Grande do Sul, Brazil

ARTICLE INFO

Keywords:
Nanorods
Anti-microbial activity
z-scheme
Catalytic activity
Molecular docking analysis

ABSTRACT

The present study aims to synthesize z-scheme heterojunction of graphitic carbon nitride (g-C_3N_4; poly 3-hexylthiophene (P3HT) doped CuO nanorods (NRs) by co-precipitation technique. Characterizations succeeded in evaluating their catalytic and antimicrobial activities. XRD investigation revealed monoclinic crystal phase of CuO. Electronic spectra identified blue shift by incorporating P3HT and g-C_3N_4 led to an increment in band gap energy. FTIR spectra proclaimed the existence of rotational and vibrational modes associated with the functional groups during synthesis activity. Catalytic degradation of toxic methylene blue (MB) was revealed by synthesized NRs in neutral, basic and acidic media. CuO NRs doped with (2 & 4%) g-C_3N_4/P3HT demonstrated promising anti-bacterial tendency against multiple drug resistant (MDR) *Escherichia coli* (*E.coli*). Furthermore, *in silico* molecular docking predictions of P3HT/CuO and g-C_3N_4 were performed against $DHFR_{E.coli}$ and $FabI_{E.coli}$ to rationale their role as possible inhibitors against these enzyme targets.

Article No: 6

Surfaces and Interfaces 42 (2023) 103372

Contents lists available at ScienceDirect

Surfaces and Interfaces

journal homepage: www.sciencedirect.com/journal/surfaces-and-interfaces

Carbon spheres/polyvinylpyrrolidone doped MnO_2 nanorods served as dye degrader and antibacterial activity with evidential molecular docking

L. Khan [a], Muhammad Ikram [a,*], Ali Haider [b], Anum Shahzadi [c], Anwar Ul-Hamid [d], Hameed Ullah [e], Sherdil Khan [e], Mohammed M. Algaradah [f], Hisham S.M. Abd-Rabboh [g], Walid Nabgan [h,*], Iram Shahzadi [c]

[a] Solar Cell Applications Research Lab, Department of Physics, Government College University Lahore, Lahore, 54000, Punjab, Pakistan
[b] Department of Clinical Sciences, Faculty of Veterinary and Animal Sciences, Muhammad Nawaz Shareef, University of Agriculture, 66000, Multan, Punjab, Pakistan
[c] Department of Pharmacy, COMSATS University Islamabad, Lahore campus, 54000, Pakistan
[d] Core Research Facilities, King Fahd University of Petroleum & Minerals, Dhahran 31261, Saudi Arabia
[e] Laboratory of Nanomaterials for Renewable Energy and Artificial Photosynthesis (NanoREAP), Instituteof Physics, UFRGS, 91509-900 Porto Alegre, Rio Grande do Sul, Brazil
[f] Chemistry Department, King Khalid Military Academy, Riyadh 11495, Saudi Arabia
[g] Chemistry Department, Faculty of Science, King Khalid University, P.O. Box 9004, Abha 61413, Saudi Arabia
[h] Departament d'Enginyeria Química, Universitat Rovira i Virgili, Av Països Catalans 26, 43007, Tarragona, Spain

ARTICLE INFO

Keywords:
Carbon sphere
PAA
MnO_2

ABSTRACT

The present study synthesized carbon sphere (CS) and polyvinylpyrrolidone (PVP) doped MnO_2 nanorods via co-precipitation technique. Using a systematic approach, this research investigates the deliberate doping of carbon spheres at 2 and 4 wt.% concentrations into a predetermined quantity of PVP-doped MnO_2 nanorods (NRs). The motive of this work was to reduce the recombination rate and inhibit the dimension of NRs that caused to increase in the catalytic reduction of methylene blue and microbicidal action of MnO_2 NRs confirmed by molecular docking analysis. Several characterization techniques were utilized to check the effect of doping agents (CS and PVP) on the structural, morphological and optical characteristics of MnO_2. The XRD pattern evidenced that MnO_2 had an orthorhombic framework, and incorporating PVP and CS reduced the crystallinity of NRs. The electronic spectra revealed the blue shift, assigned to increase band gap energy by the addition PVP and CS. TEM analysis confirmed the formation of a network of MnO_2 nanorods and decreased size with the integration of dopants. CS and PVP-doped MnO_2 NRs significantly improved their microbicidal effectiveness towards *Escherichia coli* (*E. coli*) measured in an inhibitory zone mm and catalytic performance. The enigma behind these bactericidal effects was recently unraveled by in silico assertions regarding these doped NRs for targeted enzymes (i.e., DNA gyrase and β-lactamase).

Article No: 7

frontiers | Frontiers in Environmental Science

TYPE Original Research
PUBLISHED 22 May 2023
DOI 10.3389/fenvs.2023.1158399

OPEN ACCESS

EDITED BY
Vassilis Inglezakis,
University of Strathclyde, United Kingdom

REVIEWED BY
Alzhan Baimenov,
Nazarbayev University, Kazakhstan
Gang Tang,
Anhui University of Technology, China

*CORRESPONDENCE
Muhammad Ikram,
dr.muhammadikram@gcu.edu.pk
Walid Nabgan,
walid.nabgan@urv.cat

RECEIVED 06 February 2023
ACCEPTED 13 April 2023
PUBLISHED 22 May 2023

CITATION
Khan M, Ikram M, Haider A, Ul-Hamid A, Ullah H, Shahzadi I, Khan S, Kanoun MB, Goumri-Said S, Medina F and Nabgan W (2023), Experimental and DFT study of GO-decorated CaO quantum dots for catalytic dye degradation and bactericidal potential.
Front. Environ. Sci. 11:1158399.
doi: 10.3389/fenvs.2023.1158399

Experimental and DFT study of GO-decorated CaO quantum dots for catalytic dye degradation and bactericidal potential

Mahreen Khan[1], Muhammad Ikram[1]*, Ali Haider[2], Anwar Ul-Hamid[3], Hameed Ullah[4], Iram Shahzadi[5], Sherdil Khan[4], Mohammed Benali Kanoun[6], Souraya Goumri-Said[7], Francisco Medina[8] and Walid Nabgan[8]*

[1]Solar Cell Applications Research Laboratory, Department of Physics, Government College University Lahore, Lahore, Punjab, Pakistan, [2]Department of Clinical Sciences, Faculty of Veterinary and Animal Sciences, Muhammad Nawaz Shareef University of Agriculture (MNSUA) Multan, Multan, Pakistan, [3]Center for Engineering Research, Research Institute, King Fahd University of Petroleum and Minerals, Dhahran, Saudi Arabia, [4]Laboratory of Nanomaterials for Renewable Energy and Artificial Photosynthesis (NanoREAP), Institute of Physics, UFRGS, Porto Alegre, Rio Grande do Sul, Brazil, [5]Punjab University College of Pharmacy, University of the Punjab, Lahore, Pakistan, [6]Department of Mathematics and Sciences, College of Humanities and Sciences, Prince Sultan University, Riyadh, Saudi Arabia, [7]Physics Department, College of Science and General Studies, Alfaisal University, Riyadh, Saudi Arabia, [8]Departament d'Enginyeria Química, Universitat Rovira i Virgili, Tarragona, Spain

This research lays the groundwork for preparing graphene oxide (GO)-doped CaO nanocomposites for efficient antibacterial potential and dye degradation. The study aimed to reduce the recombination rate of the electron hole (e^-/h^+) of CaO and improve charge transfer. This issue can be minimized by doping high-surface area GO into CaO quantum dots (QDs). Herein, the one-pot co-precipitation technique has prepared various concentrations (1, 3, and 5 wt%) of GO-doped CaO. Characterization techniques were used to investigate optical, elemental analysis, microstructural, functional, and morphological properties. The addition of GO into QDs showed excellent catalytic activity (CA) to control sample CaO against methylene blue (MB) in basic and acidic media compared to the neutral media. The synergistic effect of morphological alternation attributed to an increase in the mechanism of CA upon doping. Various concentrations of GO to QDs promised remarkable bactericidal potency against *Escherichia coli*.

KEYWORDS

graphene oxide, CaO, antibacterial activity, catalysis, DFT

Articles under Review

1. Ali Haider; Anum Shahzadi; Muhammad Ahsaan Bari; Anwar Ul-Hamid; **Hameed Ullah**; Sherdil Khan, "Superior catalytic reduction of RhB dye and inactivation of E. Coli by carbon sphere/graphitic carbon nitride doped zinc oxide nanorods: In Silico Molecular Docking Studies", Manuscript Number: SEPPUR-D-23-06811 (Separation and Purification Technology).
2. Lubaba Khan; Muhammad Ikram; Ali Haider; anum Shahzadi; Anwar Ul-Hamid; **Hameed Ullah**; Sherdil Khan; Mohammed M Algaradah; Hisham S.M. Abd-Rabboh; Iram Shahzadi, "Carbon spheres/polyvinylpyrrolidone doped MnO2 nanorods served as dye degrader and antibacterial activity with evidential molecular docking". Manuscript Number: SURFIN-D-23-02988. (Journal: Surfaces and Interfaces).
3. Ahmad, Wakeel; Ikram, Muhammad; Shahzadi, Iram; Haider, Ali; Ul-Hamid, Anwar; **Ullah, Hameed** ; Khan, Sherdil, "Efficient dye degradation and antimicrobial behavior with molecular docking performance of silver and polyvinylpyrrolidone doped Zn/Fe layered double hydroxide". Manuscript ID: ao-2023-05754b. (Journal: ACS Omega).
4. Fiaz Ahmad; Ali Haider; Iram Shahzadi; Wakeel Ahmad; Anwar Ul-Hamid; **Hameed Ullah**; Sherdil Khan and Muhammad Ikram, "Graphitic-carbon nitride and polyvinylpyrrolidone doped barium oxide nanorods served as dye degrader and bactericidal potential: A molecular docking study" Manuscript Number: JPHOTOCHEM-D-23-02234 (Journal: Journal of Photochemistry & Photobiology, A: Chemistry).
5. Muhammad Imran; Ali Haider; Anum Shahzadi; Muhammad Mustajab; Anwar Ul-Hamid; **Hameed Ullah**; Sherdil Khan, Muhammad Ikram, "Elucidation of nickel selenide doped silver and carbon nitride for effective dual performance in catalytic degradation and bactericidal efficiency: in silico docking study". Manuscript Number: SURFIN-D-23-05084 (Journal: Surfaces and Interfaces).
6. Anum Shahzadi; Ali Haider; Nelofer Aslam; Hafsa Saeed; Anwar Ul-Hamid; Muhammad Ali Khan; **Hameed Ullah**; Sherdil Khan, Muhammad Ikram, "Enhanced dye degradation and bactericidal behavior with in silico molecular

docking of barium and polyacrylic acid doped NiSe nanostructure". Manuscript Number: MSB-D-23-02178, (Journal: Materials Science & Engineering B).